
















Visible-light Phase Curves from the Second Year of the TESS Primary Mission

Ian Wong^{1,10} , Daniel Kitzmann² , Avi Shporer³ , Kevin Heng^{2,4} , Tara Fetherolf⁵ , Björn Benneke⁶ , Tansu Daylan^{3,11} , Stephen R. Kane⁵ , Roland Vanderspek³ , Sara Seager^{1,3,7} , Joshua N. Winn⁸ , Jon M. Jenkins⁹ , and Eric B. Ting⁹ 

¹ Department of Earth, Atmospheric and Planetary Sciences, Massachusetts Institute of Technology, Cambridge, MA 02139, USA; iwong@mit.edu

² University of Bern, Center for Space and Habitability, Bern, Switzerland

³ Department of Physics and Kavli Institute for Astrophysics and Space Research, Massachusetts Institute of Technology, Cambridge, MA 02139, USA

⁴ University of Warwick, Department of Physics, Astronomy and Astrophysics Group, Coventry CV4 7AL, UK

⁵ Department of Earth and Planetary Sciences, University of California, Riverside, CA 92521, USA

⁶ Department of Physics and Institute for Research on Exoplanets, Université de Montréal, Montréal, QC, Canada

⁷ Department of Aeronautics and Astronautics, MIT, 77 Massachusetts Avenue, Cambridge, MA 02139, USA

⁸ Department of Astrophysical Sciences, Princeton University, Princeton, NJ 08544, USA

⁹ NASA Ames Research Center, Moffett Field, CA 94035, USA

Received 2021 April 14; revised 2021 June 4; accepted 2021 June 16; published 2021 August 31

Abstract

We carried out a systematic study of full-orbit phase curves for known transiting systems in the northern ecliptic sky that were observed during Year 2 of the TESS primary mission. We applied the same methodology for target selection, data processing, and light-curve fitting as we did in our Year 1 study. Out of the 15 transiting systems selected for analysis, seven—HAT-P-7, KELT-1, KELT-9, KELT-16, KELT-20, Kepler-13A, and WASP-12—show statistically significant secondary eclipses and day–night atmospheric brightness modulations. Small eastward dayside hot-spot offsets were measured for KELT-9b and WASP-12b. KELT-1, Kepler-13A, and WASP-12 show additional phase-curve variability attributed to the tidal distortion of the host star; the amplitudes of these signals are consistent with theoretical predictions. We combined occultation measurements from TESS and Spitzer to compute dayside brightness temperatures, TESS-band geometric albedos, Bond albedos, and phase integrals for several systems. The new albedo values solidify the previously reported trend between dayside temperature and geometric albedo for planets with $1500\text{ K} < T_{\text{day}} < 3000\text{ K}$. For Kepler-13Ab, we carried out an atmospheric retrieval of the full secondary eclipse spectrum, which revealed a noninverted temperature–pressure profile, significant H₂O and K absorption in the near-infrared, evidence for strong optical atmospheric opacity due to sodium, and a confirmation of the high geometric albedo inferred from our simpler analysis. We explore the implications of the phase integrals (ratios of Bond to geometric albedos) for understanding exoplanet clouds. We also report updated transit ephemerides for all of the systems studied in this work.

Unified Astronomy Thesaurus concepts: [Exoplanet astronomy \(486\)](#)

Supporting material: machine-readable tables

1. Introduction

In 2020 July, the Transiting Exoplanet Survey Satellite (TESS) completed its 2 yr primary mission to discover new exoplanets around bright stars in the solar neighborhood. With the goal of achieving almost full sky coverage, the survey has provided high-cadence visible-wavelength photometry for hundreds of thousands of stars. Among these observed targets are hundreds of previously discovered transiting exoplanet systems. For these systems, TESS light curves enable a wide range of scientific investigations (Kane et al. 2021), from refining orbital ephemerides (e.g., Cortés-Zuleta et al. 2020; Ikwut-Ukwa et al. 2020; Szabó et al. 2020) and detecting additional transiting planets (e.g., Huang et al. 2018; Teske et al. 2020) to probing for orbital decay and transit-timing variations (e.g., Bouma et al. 2019).

The study of exoplanet phase curves in particular has benefited immensely from the nearly continuous long-baseline observations by TESS. The full-orbit light curve of a transiting system at optical wavelengths can reveal the secondary eclipse, when the light from the planet’s star-facing hemisphere is

occulted by the host star, as well as synchronous flux modulations attributed to longitudinal brightness variations across the planet’s surface (e.g., Heng & Showman 2015; Parmentier & Crossfield 2017), the tidal distortion of the surfaces of both bodies (e.g., Morris 1985; Morris & Naftilan 1993), and periodic Doppler shifting of the stellar spectrum through the mutual star–planet gravitational interaction (e.g., Shakura & Postnov 1987; Loeb & Gaudi 2003; Zucker et al. 2007; Shporer et al. 2010). Detecting and measuring these phase-curve signals can provide crucial insights into the system, including the global temperature distribution, efficiency of day–night heat transport, and reflectivity of the planet, as well as the stellar tidal response (see the review by Shporer 2017).

To date, dedicated TESS phase-curve analyses have been published for a wide range of individual exoplanet systems, including KELT-1 (Beatty et al. 2020; von Essen et al. 2020), KELT-9 (Wong et al. 2020d), KELT-16 (Mancini et al. 2021), WASP-18 (Shporer et al. 2019), WASP-19 (Wong et al. 2020b), WASP-33 (von Essen et al. 2020), WASP-100 (Jansen & Kipping 2020), and WASP-121 (Bourrier et al. 2020; Daylan et al. 2021). These are some of the brightest and most amenable targets for detailed study, yielding high signal-to-noise ratio secondary eclipse measurements and exquisite constraints on

¹⁰ 51 Pegasi b Fellow.

¹¹ Kavli Fellow.

the day–night brightness contrast. Looking beyond these benchmark targets, we have set out to compile a comprehensive body of phase-curve analyses based on TESS photometry. This effort is guided by previous systematic investigations of Kepler light curves (e.g., Esteves et al. 2013, 2015; Angerhausen et al. 2015) and facilitates ensemble studies of visible-light secondary eclipses and atmospheric properties.

In Wong et al. (2020c, hereafter Paper I), we presented a summary of phase-curve measurements from the first year of the TESS primary mission, when TESS’s four cameras surveyed the southern ecliptic sky. Ten systems displayed statistically significant secondary eclipse and/or phase-curve signals. One of the most notable results from this study emerged when combining the newly obtained TESS-band secondary eclipses with previously published Spitzer measurements, which allowed us to break the degeneracy between atmospheric reflectivity and dayside brightness temperature and calculate self-consistent TESS-band geometric albedos. We uncovered a tentative positive correlation between geometric albedo and dayside temperature among hot Jupiters, suggesting a steady increase in reflective cloud cover and/or systematic deviations from blackbody-like emission spectra with increasing temperature. This surprising and consequential finding necessitates further study, and the inclusion of additional data points into the body of geometric albedo measurements promises to shed more light on this emergent trend.

In this paper, we extend our previous systematic phase-curve study of southern targets into the northern ecliptic sky, which was observed by TESS during the second year of the primary mission. A comparable number of targets are considered, among which seven show robust phase-curve signals. We employ a consistent light-curve processing and fitting methodology, thereby ensuring that the analyses carried out in this paper and Paper I constitute a uniform set of results.

The target-selection criteria, TESS light curves, and data-analysis techniques are described in Sections 2.1–2.3, respectively. Section 3 presents the results of our phase-curve fits. In Section 4, we use published Spitzer secondary eclipse measurements to expand the list of self-consistently derived geometric albedo and dayside brightness temperatures (Section 4.1) and revisit the emergent albedo versus temperature trend for highly irradiated planets (Section 4.2). This discussion is supplemented by detailed emission spectrum modeling of the high-albedo hot Jupiter Kepler-13Ab (Section 4.3), as well as an exploration of the predictive power of albedo measurements in characterizing exoplanet cloud properties (Section 4.4). Lastly, we present updated transit ephemerides in Section 4.5. A broad summary of the results of this work is given in Section 5.

2. Light-curve Analysis

To ensure maximum consistency with our systematic phase-curve study from the first year of the TESS mission (Paper I), we implemented an identical methodology for target selection, data processing, phase-curve modeling, and error analysis. All steps in the light-curve analysis were carried out using the ExoTEP pipeline (e.g., Benneke et al. 2019; Wong et al. 2020a). We briefly discuss these techniques in the following; see Paper I for a more detailed description of the methods.

2.1. Target Selection

Targets for phase-curve study were selected from the population of all transiting planet and brown dwarf systems published in the literature as of 2021 January 1. In order to adequately resolve the transit and secondary eclipse shapes, we limited our scope to systems that were preselected by the TESS mission to have photometry extracted at 2 minute cadence, as opposed to the 30 minute cadence of the stacked full-frame images.

The signal-to-noise ratio and predicted signal-strength thresholds that we considered are unchanged from those defined in Paper I. We first excluded systems with TESS-band magnitudes greater than $T=12.5$ mag. For the remaining systems, we used the predicted secondary eclipse depth as the determining factor in the selection. To compute this depth D'_d , we assumed maximally inefficient day–night heat recirculation and a dayside geometric albedo of $A_g=0.1$ (Esteves et al. 2013, 2015; Heng & Demory 2013; Shporer 2017):

$$D'_d = \left(\frac{R_p}{R_*}\right)^2 \frac{\int B_\lambda(T_p)\tau(\lambda)d\lambda}{\int B_\lambda(T_*)\tau(\lambda)d\lambda} + A_g \left(\frac{R_p}{a}\right)^2, \quad (1)$$

$$T_p = T_* \sqrt{\frac{R_*}{a}} \left[\frac{2}{3} \left(1 - \frac{3}{2} A_g \right) \right]^{1/4}, \quad (2)$$

where we assumed a conversion factor of 3/2 between the Bond and geometric albedos, as is appropriate for Lambertian scattering. Here the photon-weighted planetary and stellar emission spectra, which are approximated by blackbodies with temperatures T_p and T_* , respectively, are integrated over the TESS transmission function $\tau(\lambda)$. We note that the TESS transmission function provided online¹² is given in energy units, so an additional factor of λ/hc is not needed. The remaining variables are system parameters related to the shape of the transit light curve: the planet–star radius ratio R_p/R_* and the scaled orbital semimajor axis a/R_* . As a preliminary cut, we calculated the predicted secondary eclipse depths using parameter values from the respective discovery papers and selected all systems with $D'_d > 100$ ppm/ \sqrt{s} , where s is the number of sectors that a system was observed by TESS, and the scaling reflects the approximate increase in combined signal-to-noise ratio with additional sectors of observation.

Next, we inspected the raw light curves of the systems that passed this threshold (see Section 2.2). In order to limit our analysis to cases where the astrophysical signal can be reliably detected, we removed systems that show severe systematics and/or significant short-period stellar variability. Both of these features present difficulties for systematics detrending methodologies, particularly when the timescale of the variations is shorter than the orbital period (i.e., the characteristic timescale of the phase-curve modulation). Several targets that are otherwise promising for phase-curve study were excluded due to excessive variability, including KELT-7, WASP-33,¹³ and XO-3. An exception to this exclusion condition is KELT-9, which displays a stellar pulsation signal with a period of roughly 7.6 hr (Wong et al. 2020d). Having previously

¹² <https://heasarc.gsfc.nasa.gov/docs/tess/data/tess-response-function-v1.0.csv>

¹³ A dedicated analysis of the WASP-33 TESS phase curve was published in von Essen et al. (2020), where a detailed treatment of the complex stellar pulsation frequency spectrum was applied.

analyzed the TESS light curve for this system, we included it in the present work to derive updated phase-curve results using a consistent methodology with the other targets on the list.

The final set of 15 targets selected for our systematic phase-curve analysis is as follows: HAT-P-7 (Pál et al. 2008), HAT-P-36 (Bakos et al. 2012), KELT-1 (Siverd et al. 2012), KELT-9 (Gaudi et al. 2017), KELT-16 (Oberst et al. 2017), KELT-20 (Lund et al. 2017), KELT-23A (Johns et al. 2019), Kepler-13A (Shporer et al. 2011; Szabó et al. 2011), Qatar-1 (Alsubai et al. 2011), TrES-3 (O’Donovan et al. 2007), WASP-3 (Pollacco et al. 2008), WASP-12 (Hebb et al. 2009), WASP-92 (Hay et al. 2016), WASP-93 (Hay et al. 2016), and WASP-135 (Spake et al. 2016).

As in Paper I, we established an additional selection criterion based on the predicted amplitudes of the ellipsoidal distortion and Doppler-boosting phase-curve signals. Ellipsoidal distortion of the host star yields a photometric modulation with a leading-order term at the first harmonic of the cosine of the orbital period, while Doppler boosting produces a contribution at the fundamental of the sine. The corresponding semi-amplitudes are related to the planet–star mass ratio $q \equiv M_p/M_*$ via the following expressions (e.g., Shporer 2017):

$$A'_{\text{ellip}} = \alpha_{\text{ellip}} q \left(\frac{R_*}{a} \right)^3 \sin^2 i, \quad (3)$$

$$A'_{\text{Dopp}} = \left[\frac{2\pi G}{Pc^3} \frac{q^2 M_p \sin^3 i}{(1+q)^2} \right]^{\frac{1}{3}} \left\langle \frac{xe^x}{e^x - 1} \right\rangle_{\text{TESS}}. \quad (4)$$

Here i is the orbital inclination, P represents the orbital period, and $x \equiv hc/k\lambda T_*$. The expression for the ellipsoidal distortion semi-amplitude includes a prefactor α_{ellip} , which depends on the linear limb- and gravity-darkening coefficients for the host star (see, for example, Morris 1985 and Shporer 2017). Tabulated values of the TESS-band limb- and gravity-darkening coefficients from Claret (2017) were interpolated to provide appropriate coefficients for a given set of stellar parameters. In the case of Doppler boosting, the term inside the angled brackets is the logarithmic derivative of the host star’s spectrum (approximated as a blackbody) and is integrated over the TESS bandpass. Using a theoretical stellar spectrum instead (e.g., a PHOENIX model; Husser et al. 2013) results in a negligible change to the resultant Doppler-boosting amplitude at a level of a few percent.

We calculated the predicted A'_{ellip} and A'_{Dopp} values for all known systems brighter than $T = 12.5$ mag and set a minimum threshold of 25 ppm. We found that all systems for which A'_{ellip} and/or A'_{Dopp} exceed 25 ppm were already added to our target list by satisfying the aforementioned secondary eclipse depth benchmark; hence, no additional targets were included based on this threshold.

2.2. TESS Light Curves

During the second year of the primary mission, TESS observed the northern ecliptic hemisphere, which was divided into 13 sectors. Each sector has a combined field of view of $24^\circ \times 96^\circ$ and was observed for 27.4 days, during which the spacecraft completed two eccentric orbits around the Earth, with a gap in science observations near perigee for data downlink.

We obtained the light-curve files from the Mikulski Archive for Space Telescopes (MAST). The photometry and associated data products were produced using the official Science Processing Operations Center (SPOC) pipeline, based at the NASA Ames Research Center (Jenkins et al. 2016). The files contain both the raw simple aperture photometry (SAP) and the presearch data conditioning (PDC) light curves, which were corrected for instrumental systematics using cotrending basis vectors empirically derived on a sector-by-sector basis for each camera and detector on the instrument (Smith et al. 2012; Stumpe et al. 2012, 2014). Just as in Paper I, we carried out analogous analyses of the SAP and PDC light curves and found that the systematics corrections by the SPOC pipeline typically result in significantly reduced long-term flux variations and reduced red noise while crucially preserving the astrophysical phase-curve signal of interest. For most targets, we utilized the PDC light curves in the final fits presented in this paper.

However, for systems exhibiting significant stellar variability, the PDC detrending process is often unable to properly discriminate between instrumental systematics trends and flux variations from the star, resulting in poorer light-curve quality. This was previously seen in the light curves of several active targets, including WASP-19 (Wong et al. 2020b) and WASP-121 (Daylan et al. 2021). Among the Year 2 targets selected for phase-curve analysis, only TrES-3 displays notable photometric variability from stellar activity. For that system, we used the SAP light curve instead and detrended the instrumental systematics by using the publicly available cotrending basis vectors.

We note that TESS data from sectors 14–19 were reprocessed by the official SPOC pipeline after their initial release to rectify issues with the time stamps and alter the treatment of scattered light, among other improvements.¹⁴ The previously published phase-curve analyses of KELT-1 (Beatty et al. 2020; von Essen et al. 2020) and KELT-9 (Wong et al. 2020d) were based off of the original versions of the light curves. In this analysis, we used the newer versions of the photometry for all targets observed in sectors 14–19. As discussed in Sections 3.2 and 3.7, the updated astrophysical parameter values for KELT-1 and KELT-9 in this paper do not differ significantly from the previously published results.

Following our previous work (Wong et al. 2020b, 2020c, 2020d), we split each sector’s worth of photometry into smaller segments that are separated by the scheduled momentum dumps. During the second year of the primary mission, these occurred once or twice during each spacecraft orbit and were typically associated with discernible discontinuities in the photometry, with some instances showing additional flux ramps before and/or after. In cases with severe flux ramps on short timescales (i.e., shorter than the orbital period of the system), we trimmed the ramps prior to fitting, with the trimming interval selected among multiples of 0.25 day. After removing all points assigned a nonzero data-quality flag by the SPOC pipeline, we applied a 16 point wide moving median filter to trim 3σ outliers. Lastly, we inspected each light curve and disregarded all segments shorter than 1 day, as well as those that show systematically larger time-correlated noise or contain large gaps due to periods of significant scattered light on the detector.

¹⁴ See the notes for Data Release 30 for full details: archive.stsci.edu/tess/tess_drn.html (dated 2020 August 5).

In Appendix A, we provide a full description of the data segments used in our analysis. The raw and trimmed light curves for each target are plotted in Appendix B, with the locations of momentum dumps indicated by vertical blue lines.

2.3. Phase-curve Model Fitting

The combined phase-curve and systematics model used in our fits was defined exactly as in Paper I:

$$f(t) = \psi(t) \times S_N^{(k)}(t). \quad (5)$$

The first term is the astrophysical model that describes the photometric modulation of the host star and orbiting companion separately with respect to orbital phase $\phi \equiv 2\pi(t - T_0)/P$, as well as the geometrical loss-of-light functions due to transits $\lambda_t(t)$ and secondary eclipses $\lambda_e(t)$ ¹⁵:

$$\psi(t) = \frac{\psi_*(t)\lambda_t(t) + \psi_p(t)\lambda_e(t)}{1 + \bar{f}_p}, \quad (6)$$

$$\psi_p(t) = \bar{f}_p - A_{\text{atm}} \cos(\phi + \delta), \quad (7)$$

$$\psi_*(t) = 1 - A_{\text{ellip}} \cos(2\phi) + A_{\text{Dopp}} \sin(\phi). \quad (8)$$

Both transits and secondary eclipses were modeled using *batman* (Kreidberg 2015). The variables \bar{f}_p , A_{atm} , and δ signify the average relative brightness of the companion, the semiamplitude of the atmospheric brightness modulation, and the corresponding phase shift, respectively. From these parameters, the dayside flux (i.e., secondary eclipse depth) and nightside flux are given by $D_d = \bar{f}_p - A_{\text{atm}} \cos(\pi + \delta)$ and $D_n = \bar{f}_p - A_{\text{atm}} \cos(\delta)$.

The host star’s variability includes contributions from ellipsoidal distortion and Doppler boosting. In cases where significant ellipsoidal distortion amplitudes were measured, we experimented with fitting for additional higher-order harmonics but did not retrieve any statistically significant signals. For targets where no significant A_{ellip} or A_{Dopp} values were retrieved in unconstrained fits, we followed the methodology of Paper I and applied Gaussian priors on the amplitudes instead. These priors were derived using Equations (3) and (4), the stellar parameters from the corresponding discovery papers, and the tabulated limb- and gravity-darkening coefficients from Claret (2017).

The second term in Equation (5) is the systematics detrending model, which consists of generalized polynomial functions in time that were applied separately to each data segment k in the light curve:

$$S_N^{(k)}(t) = \sum_{j=0}^N c_j^{(k)} (t - t_0)^j. \quad (9)$$

Here t_0 is the time of the first data point of the segment, and N is the order of the detrending polynomial. To choose the optimal polynomial order for a given segment, we fit the segment’s light curve individually, selecting the order that minimized the Bayesian information criterion (BIC). Table A1 in Appendix A lists the optimal polynomial orders for every

segment; typical values range from zero to 2. The systematics-detrended light curves are plotted in Appendix B.

In the first step of our light-curve analysis, the astrophysical and systematics models were fit simultaneously using the affine-invariant Markov Chain Monte Carlo (MCMC) routine *emcee* (Foreman-Mackey et al. 2013). All transit shape and orbital ephemeris parameters were allowed to vary freely, except in the case of KELT-9, where the transits were trimmed from the light curve and Gaussian priors were used instead (Section 3.7). For all of the targets in our analysis, the orbit of the companion is consistent with circular, and we set the orbital eccentricity to zero. The time of secondary eclipse was adjusted for the light-travel time between inferior and superior conjunction, which is less than a minute for all targets in our study. The fitted parameters are the mid-transit time T_0 , orbital period P , impact parameter b , scaled orbital semimajor axis a/R_* , planet–star radius ratio R_p/R_* , and modified quadratic limb-darkening coefficients, which are defined by Holman et al. (2006): $\gamma_1 \equiv 2u_1 + u_2$ and $\gamma_2 \equiv u_1 - 2u_2$, where u_1 and u_2 are the standard quadratic coefficients. We also introduced a uniform per-point scatter parameter σ , which was allowed to float freely to ensure that the chains converged to models with a reduced χ^2 value near unity.

In the next step, we employed two methods to account for the additional contribution of red noise at timescales longer than the 2 minute cadence of the time series. First, following the technique first described by Pont et al. (2006), we computed the scatter in the residual series, binned at various intervals n , and calculated the average fractional deviation ξ from the $1/\sqrt{n}$ scaling expected for pure white noise across bin sizes corresponding to time intervals between 20 minutes and 8 hr. These timescales are relevant to the primary features of the astrophysical model, i.e., transit ingress/egress and phase-curve inflection timescales. To incorporate this long-timescale red noise contribution into the final MCMC fits, we inflated the previously calculated per-point uncertainty values σ by ξ and reran the fitting procedure, now with the flux uncertainties fixed to the new values. The second technique was “prayer-bead” (PB) residual permutation (e.g., Gillon et al. 2009); after dividing out the best-fit systematics detrending model from the initial MCMC fit, we cyclically shifted and readded the residual array 5000 times, each time computing the best-fit astrophysical parameters using a standard Levenberg–Marquardt optimization routine. The uncertainties on the fit parameters were derived from the resulting 5000-point posteriors of the best-fit values.

For all parameters except the mid-transit time, the uncertainty-inflated MCMC analysis yielded larger uncertainties, and we present those values in the results tables below. For T_0 , the PB analysis produced uncertainties that are consistently larger than those from the MCMC fits (by up to 150%). We list both the MCMC- and PB-derived transit timings in the tables and utilize the larger PB uncertainties when calculating updated transit ephemerides (Section 4.5).

3. Results

For each of the 15 targets, we determined which phase-curve signals were robustly detected in the TESS light curves by running an ensemble of joint MCMC fits that included different combinations of phase-curve parameters. In cases where no significant ellipsoidal distortion and/or Doppler-boosting signals were measured from an unconstrained fit, we instead

¹⁵ The formulation presented here contains a few simplifying assumptions regarding the shape of the atmospheric brightness modulation and higher-order terms in the ellipsoidal distortion modulation. See Paper I for a full description of the caveats and validations for our approach.

applied Gaussian priors on the semiamplitudes based on the predicted values derived using Equations (3) and (4). For the final fit results, we selected the combination of free parameters that minimized the Akaike information criterion (AIC). The AIC penalizes the addition of free parameters less severely than the BIC, so considering the AIC allowed us to explore some comparatively marginal phase-curve signals. These weak detections will benefit the most from additional light curves obtained during the extended mission and help orient strategies for follow-up study.

In the following subsections, we present the results for the seven systems that yielded significant phase-curve signals. Due to the presence of stellar pulsations and additional light-curve variability, the KELT-9 light curve was treated differently than the other six targets; that system is discussed after the other nominal cases. Finally, for the remaining eight systems without statistically significant phase-curve signals or secondary eclipses, we present the results from transit-only light-curve fits; these targets are discussed together in the last subsection.

3.1. HAT-P-7

The HAT-P-7 system consists of a highly irradiated $1.8 M_{\text{Jup}}$, $1.4 R_{\text{Jup}}$ gas giant that lies on a nearly pole-on 2.205 day orbit around an evolved F6 star with an effective temperature of 6350 K (Pál et al. 2008; Narita et al. 2009; Winn et al. 2009). The brightness of the host star ($T = 10.0$ mag, $V = 10.5$ mag) has made HAT-P-7 an attractive candidate for both ground- and space-based atmospheric characterization. This system is also located within the Kepler field of view, and the full-orbit Kepler phase curve has been analyzed by several authors (Borucki et al. 2009; Esteves et al. 2015; Armstrong et al. 2016). TESS observed HAT-P-7 in sectors 14 and 15.

From our phase-curve analysis, we obtained a strong detection of the secondary eclipse ($D_d = 127_{-32}^{+33}$ ppm) and the atmospheric brightness modulation ($A_{\text{atm}} = 56_{-13}^{+14}$ ppm). The corresponding nightside flux is consistent with zero. No significant offset in the atmospheric phase-curve variation was measured ($\delta = 5^\circ \pm 12^\circ$). This is consistent with the results from the Kepler phase-curve analysis, which found a small but statistically robust offset of 7.0 ± 0.3 (Esteves et al. 2015). Meanwhile, phase curves of HAT-P-7b obtained in the Spitzer 3.6 and $4.5 \mu\text{m}$ bands show insignificant but formally consistent eastward shifts in the dayside hot spot of 7.0 ± 7.5 and 4.1 ± 7.5 , respectively (Wong et al. 2016).

The ellipsoidal distortion and Doppler-boosting signals were not detected in an unconstrained fit. For this and all other analogous cases, we plugged the measured values for T_{eff} , M_p , q , P , a/R_* , and i from the discovery papers into Equations (3) and (4) to derive the predicted values A_{ellip} and A_{Dopp} , which we used as priors in the final fit. For HAT-P-7, we obtained $A_{\text{ellip}} = 16 \pm 4$ and $A_{\text{Dopp}} = 2.2 \pm 0.1$ ppm. The measured orbital ephemeris, transit shape, and transit-depth parameter values are consistent with the measurements reported in the discovery paper (Pál et al. 2008) to within 1σ . Our results also agree with the more precise planetary parameters from the Kepler phase-curve analysis in Esteves et al. (2015). The full set of results from our light-curve fit is provided in Table 1. Marginal detections (i.e., those that yielded increases in the AIC upon inclusion in the model) are indicated with parentheses, while parameters that were constrained by Gaussian priors are shown with square brackets. We used the posteriors from our MCMC fit to compute various derived parameters: inclination i , standard

quadratic limb-darkening coefficients (u_1, u_2), orbital semimajor axis a , and planetary radius R_p .

Zoomed-in views of the systematics-corrected, phase-folded, and binned transit light curves for HAT-P-7 and all other systems are compiled in Figure 1. Figure 2 displays the full phase-folded TESS phase curve of HAT-P-7 and the corresponding residuals from the best-fit model; the middle panel shows the three components of the phase-curve model in blue. The binning interval is chosen so as to yield roughly 75 bins spanning the orbital period.

In their Kepler phase-curve analysis, Esteves et al. (2015) found a significant phase-curve signal at the second harmonic of the orbital period (i.e., $\cos(3\phi)$ and $\sin(3\phi)$), which has a semiamplitude of around 2 ppm. This additional variability may be attributable to the spin-orbit misalignment, which causes the tidal bulge to traverse regions of the star’s surface that have different surface gravities and temperatures. For the TESS light curve, the amplitude of this signal is dwarfed by the uncertainties on the phase-curve amplitudes.

Another notable result from the Kepler phase-curve study of HAT-P-7 was the detection of temporal variations in the offset between the location of peak brightness and the substellar point (Armstrong et al. 2016; but see also Lally & Vanderburg 2020). Specifically, it was reported that the direction of the phase-curve offset repeatedly shifts between westward and eastward on a timescale of tens to hundreds of days. The TESS observations of this system spanned two sectors (~ 55 days). While the photometric precision of the TESS light curves and the corresponding sensitivity of the phase-curve results are significantly lower than in the case of Kepler, we nevertheless carried out individual fits of each sector’s light curve. We obtained mutually consistent amplitude and phase-shift values for sectors 14 and 15: $A_{\text{atm},14} = 44 \pm 20$ ppm, $A_{\text{atm},15} = 64 \pm 21$ ppm, $\delta_{14} = 8^\circ \pm 21^\circ$, and $\delta_{15} = 2^\circ \pm 16^\circ$. However, we note that even when jointly fitting ~ 10 orbits of the system within each sector, the precision of our measured phase shifts still dwarfs the standard deviation of the individual Kepler-band offsets measured by Armstrong et al. (2016), which was reported to be 12° .

3.2. KELT-1

KELT-1b is a $27 M_{\text{Jup}}$ brown dwarf on a 1.22 day low-obliquity orbit around an evolved mid-F star (Siverv et al. 2012). The system was observed by TESS in sector 17, and the full-orbit phase curve was previously studied in two independent analyses (Beatty et al. 2020; von Essen et al. 2020). In this work, we utilized the updated photometry from the SPOC pipeline to reanalyze the light curve.

We measured a secondary eclipse depth of 388_{-65}^{+67} ppm, an atmospheric phase-curve modulation with a semiamplitude of 176_{-30}^{+29} ppm, and a nightside flux of 39_{-72}^{+70} ppm. Our eclipse depth is consistent with the ground-based z' -band ($\lambda_{\text{eff}} = 892$ nm) measurement of 490 ± 230 reported by Beatty et al. (2014). We did not find a significant phase-curve offset in the TESS phase curve. The strongest phase-curve component in the data is the ellipsoidal distortion signal, which has a semiamplitude of 416_{-36}^{+25} ppm. The Doppler-boosting modulation was not detected in an unconstrained fit, and A_{Dopp} was constrained by a Gaussian prior in the final fit based on the predicted value: 43 ± 2 ppm.

All of our phase-curve parameter values are consistent with those measured by the earlier analyses, demonstrating that the updated photometry and any differences in data-analysis methodology did not have any substantive effect on the conclusions of our phase-

Table 1
Results from Phase-curve Fits without Stellar Pulsations

Parameter	HAT-P-7		KELT-1		KELT-16	
	Value	Error	Value	Error	Value	Error
Fitted Parameters						
R_p/R_*	0.0770	$^{+0.0009}_{-0.0011}$	0.07612	$^{+0.00095}_{-0.00076}$	0.1099	$^{+0.0021}_{-0.0018}$
$T_{0,\text{MCMC}}$ (BJD _{TDB} -2,458,000) ^a	709.02447	$^{+0.00018}_{-0.00019}$	778.92668	$^{+0.00022}_{-0.00024}$	719.14833	0.00025
$T_{0,\text{PB}}$ (BJD _{TDB} -2,458,000) ^a	709.02466	$^{+0.00034}_{-0.00033}$	778.92707	$^{+0.00048}_{-0.00050}$	719.14831	$^{+0.00045}_{-0.00042}$
P (days)	2.204753	$^{+0.000027}_{-0.000025}$	1.217537	$^{+0.000036}_{-0.000034}$	0.968995	$^{+0.000033}_{-0.000029}$
b	0.41	$^{+0.08}_{-0.14}$	0.27	$^{+0.15}_{-0.17}$	0.29	0.16
a/R_*	4.31	$^{+0.19}_{-0.17}$	3.59	$^{+0.10}_{-0.18}$	3.21	$^{+0.10}_{-0.16}$
\bar{f}_p (ppm)	71	30	213	61	240	$^{+120}_{-110}$
A_{atm} (ppm)	56	$^{+14}_{-13}$	176	$^{+29}_{-30}$	175	$^{+64}_{-62}$
δ (deg)	(5) ^b	(12) ^b	(5.2)	(-7.4) ^b	(6)	(-19) ^b
A_{ellip} (ppm)	[16] ^b	[4] ^b	416	$^{+25}_{-26}$	[72]	[10]
A_{Dopp} (ppm)	[2.2]	[0.1]	[43]	[2]	[5.2]	[0.3]
γ_1 ^c	0.795	$^{+0.080}_{-0.086}$	0.74	$^{+0.10}_{-0.11}$	0.82	0.14
γ_2 ^c	-0.68	$^{+0.51}_{-0.47}$	-0.17	$^{+0.39}_{-0.54}$	-0.45	$^{+0.57}_{-0.66}$
Derived Parameters						
D_d (ppm) ^d	127	$^{+33}_{-32}$	388	$^{+67}_{-65}$	410	$^{+130}_{-120}$
D_n (ppm) ^d	14	32	39	$^{+70}_{-72}$	70	130
i (deg)	84.6	$^{+2.0}_{-1.4}$	85.8	$^{+2.7}_{-2.8}$	84.8	$^{+3.0}_{-3.3}$
u_1	0.18	$^{+0.11}_{-0.10}$	0.26	$^{+0.09}_{-0.12}$	0.23	$^{+0.12}_{-0.13}$
u_2	0.43	$^{+0.19}_{-0.20}$	0.22	$^{+0.21}_{-0.16}$	0.34	$^{+0.28}_{-0.22}$
a (au)	0.0365	0.0037	0.0244	0.0011	0.0203	0.0012
R_p (R_{Jup})	1.38	0.13	1.081	0.028	1.454	0.068
M_p (M_{Jup}) ^e	25.1	$^{+3.7}_{-3.3}$
Parameter	KELT-20		Kepler-13A		WASP-12	
	Value	Error	Value	Error	Value	Error
Fitted Parameters						
R_p/R_*	0.11562	$^{+0.00056}_{-0.00064}$	0.08739	$^{+0.00046}_{-0.00039}$	0.1169	$^{+0.0010}_{-0.0012}$
$T_{0,\text{MCMC}}$ (BJD _{TDB} -2,458,000)	698.21073	0.00011	718.82552	0.00015	853.91923	$^{+0.00013}_{-0.00011}$
$T_{0,\text{PB}}$ (BJD _{TDB} -2,458,000)	698.21073	0.00014	718.82551	$^{+0.00030}_{-0.00034}$	853.91918	$^{+0.00020}_{-0.00021}$
P (days)	3.474074	$^{+0.000042}_{-0.000045}$	1.7635869	0.0000016	1.091414	$^{+0.000015}_{-0.000017}$
b	0.499	$^{+0.021}_{-0.024}$	0.12	$^{+0.10}_{-0.09}$	0.338	$^{+0.065}_{-0.084}$
a/R_*	7.546	$^{+0.095}_{-0.090}$	4.508	$^{+0.033}_{-0.070}$	3.062	$^{+0.063}_{-0.066}$
\bar{f}_p (ppm)	64	$^{+34}_{-32}$	151	$^{+45}_{-39}$	184	$^{+82}_{-79}$
A_{atm} (ppm)	43	$^{+13}_{-11}$	151	$^{+15}_{-16}$	264	$^{+33}_{-30}$
δ (deg)	(-9)	(-16) ^b	(8.9)	(-5.0) ^b	13.2	5.7
A_{ellip} (ppm)	49	$^{+17}_{-16}$	80	$^{+33}_{-35}$
A_{Dopp} (ppm)	[6.8]	[1.7]	[2.3]	[0.2]
γ_1	0.583	$^{+0.048}_{-0.050}$	0.667	$^{+0.051}_{-0.053}$	0.733	0.069
γ_2	-0.22	$^{+0.34}_{-0.42}$	0.08	$^{+0.18}_{-0.27}$	-0.41	$^{+0.46}_{-0.49}$
Derived Parameters						
D_d (ppm)	111	$^{+35}_{-36}$	301	$^{+46}_{-42}$	443	$^{+86}_{-85}$
D_n (ppm)	18	$^{+36}_{-33}$	0	$^{+48}_{-43}$	-74	$^{+90}_{-85}$
i (deg)	86.21	$^{+0.23}_{-0.21}$	88.5	$^{+1.1}_{-1.4}$	83.7	$^{+1.7}_{-1.4}$
u_1	0.188	$^{+0.079}_{-0.095}$	0.282	$^{+0.044}_{-0.060}$	0.209	$^{+0.091}_{-0.092}$
u_2	0.21	$^{+0.16}_{-0.13}$	0.10	$^{+0.11}_{-0.07}$	0.31	$^{+0.20}_{-0.18}$
a (au)	0.0549	0.0022	0.03585	0.00093	0.0224	0.0011
R_p (R_{Jup})	1.761	0.069	1.454	0.035	1.786	0.081
M_p (M_{Jup})	3.9-11.2	...	3.0	1.3

Notes.^a Mid-transit times derived from the MCMC and PB analyses.^b Marginally detected phase-curve parameters are provided in parentheses. Square brackets denote applied Gaussian priors.^c Modified limb-darkening parameters $\gamma_1 \equiv 2u_1 + u_2$ and $\gamma_2 \equiv u_1 - 2u_2$.^d Here D_d and D_n are the dayside and nightside fluxes, respectively. The dayside flux is equivalent to the secondary eclipse depth.^e Companion masses derived from the measured ellipsoidal distortion, when applicable.

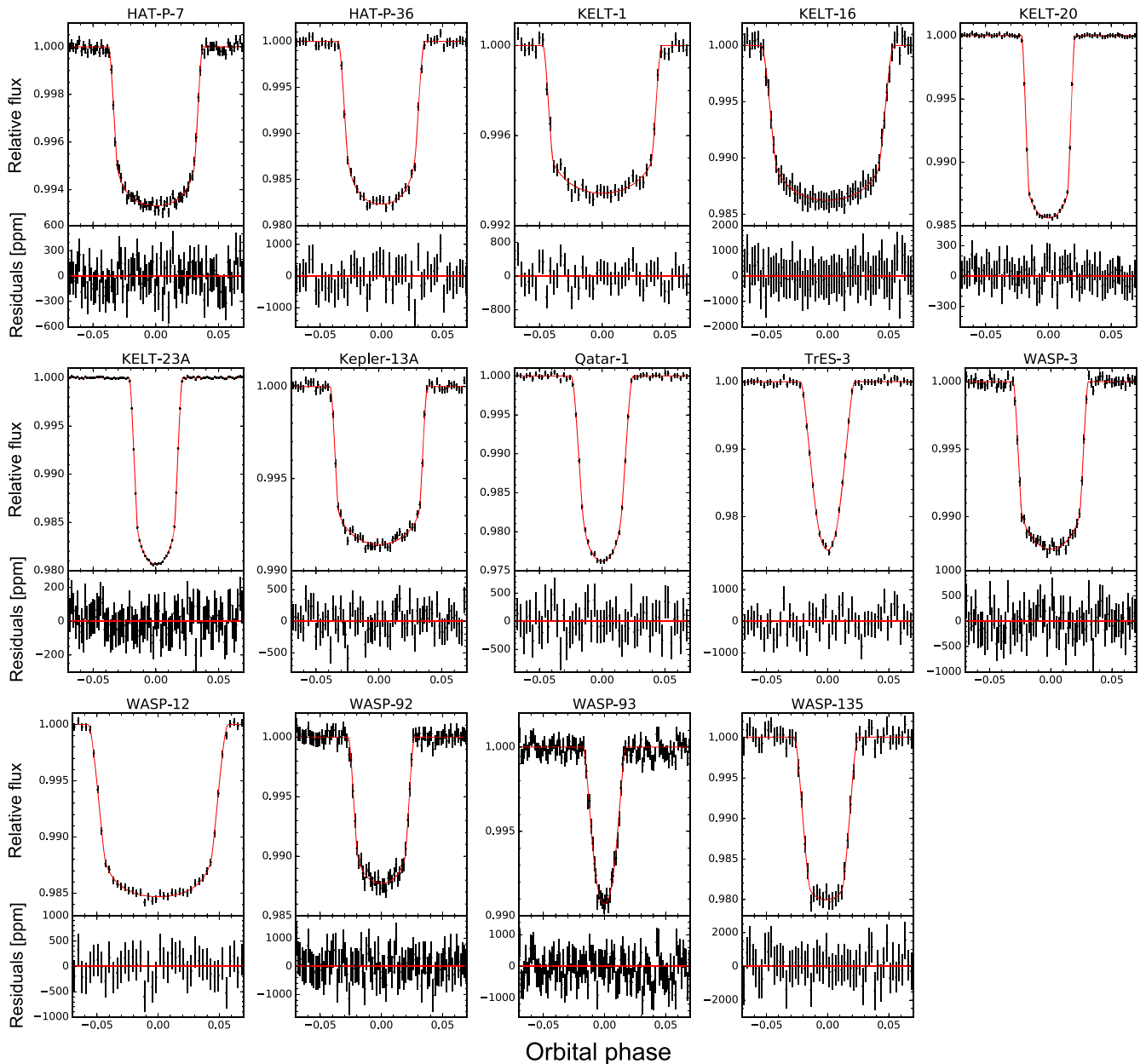


Figure 1. Compilation of the systematics-corrected and phase-folded TESS light curves in the vicinity of the primary transit for 14 of the 15 targets analyzed in this work. KELT-9 is excluded, because the transits were removed from the time series prior to analysis (Section 3.7). The best-fit phase-curve models have been removed from the data for the systems where significant signals were detected. The corresponding residuals from the best-fit model are shown in the bottom panels. The databinning interval was set to 3, 5, and 10 minutes for systems with orbital periods in the ranges $P < 1$ day, $1 \text{ days} \leq P \leq 3$ days, and $P > 3$ days, respectively.

curve fit. In particular, the published secondary eclipse depths from Beatty et al. (2020) and von Essen et al. (2020)— 371^{+47}_{-49} and 320 ± 69 ppm, respectively—agree with our value at much better than the 1σ level. Using Equation (3) and the system parameters presented in Siverd et al. (2012), we computed a predicted ellipsoidal distortion semiamplitude of 460 ± 40 , which agrees with our measured value at the 0.9σ level. We utilized the same equation to arrive at an independent photometric constraint on the brown dwarf’s mass based on the measured ellipsoidal distortion amplitude: $25.1^{+3.7}_{-3.3} M_{\text{Jup}}$.

The full results from our phase-curve analysis of KELT-1 are listed in Table 1. The full-orbit phase-folded light curve is shown in Figure 3.

Full-orbit Spitzer phase-curve observations of the KELT-1 system were presented in Beatty et al. (2019). Significant eastward

phase offsets in the atmospheric brightness modulation signal were measured in both the 3.6 and $4.5 \mu\text{m}$ bandpasses: $28^{\circ}6 \pm 3^{\circ}8$ and $18^{\circ}5 \pm 5^{\circ}1$, respectively. These values are larger than the marginal phase-curve offset that we measured from the TESS phase curve, suggesting that the infrared bandpasses are probing regions of the atmosphere with more efficient longitudinal heat transport and/or longer atmospheric radiative timescales than the optical wavelength observations (e.g., Showman & Guillot 2002; Komacek & Showman 2016).

3.3. KELT-16

The ultrashort-period transiting system KELT-16, which contains a massive, inflated, $2.75 M_{\text{Jup}}$ hot Jupiter and an F7V star with $T_{\text{eff}} = 6236 \pm 54$ K (Oberst et al. 2017), was observed by the TESS spacecraft in sector 15. Similar to the case of

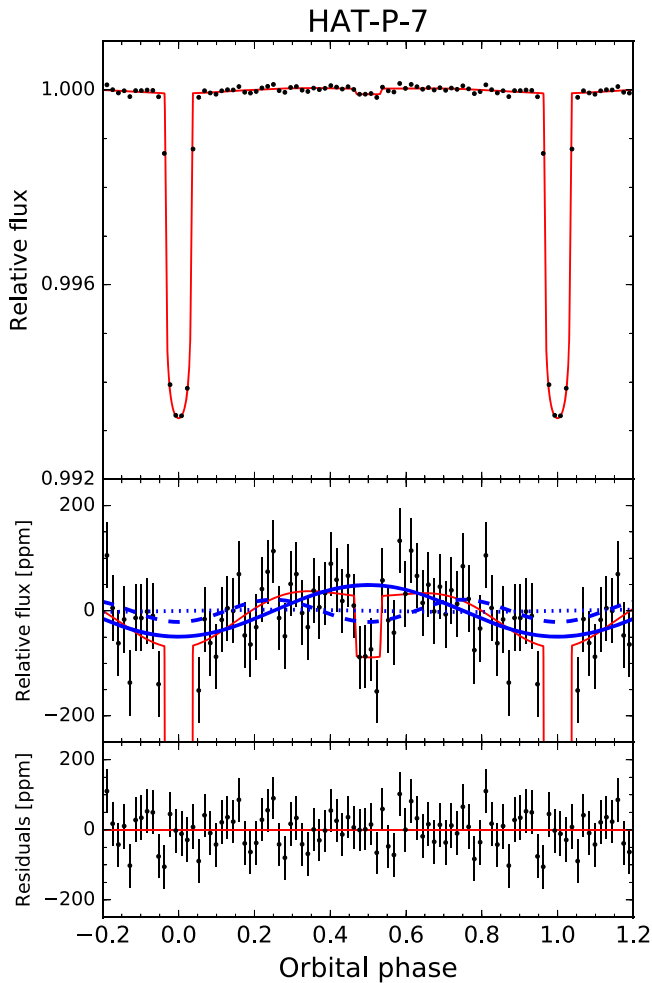


Figure 2. Top: systematics-removed TESS light curve of HAT-P-7, phase-folded and binned in 40 minute intervals (black points). Here and in all subsequent plots, orbital phase is given as a fraction of the orbital period. The best-fit full phase-curve model from the joint fit analysis is plotted in red. Middle: expanded view of the phase-curve variations, with the atmospheric modulation, ellipsoidal distortion, and Doppler-boosting components overplotted in solid, dashed, and dotted blue curves, respectively. Bottom: the corresponding residuals from the best-fit phase-curve model.

HAT-P-7, we did not independently measure any phase-curve variability attributed to ellipsoidal distortion and Doppler boosting, and we applied priors to the corresponding amplitudes, which have predicted semi-amplitudes of 72 ± 10 and 5.2 ± 0.3 ppm, respectively. We detected a secondary eclipse with a depth of 410^{+130}_{-120} ppm and an atmospheric brightness modulation signal with a semi-amplitude of 175^{+64}_{-62} ppm and no offset. From the standpoint of statistical significance, this system displays the weakest signals among the seven targets that had robust secondary eclipse and phase-curve detections.

Table 1 provides the full results from our light-curve analysis. The other system parameters are all consistent with the values from the discovery paper to well within 1σ . Figure 4 shows the phase-folded light curve.

The Spitzer $4.5 \mu\text{m}$ full-orbit phase curve of KELT-16b was published by Bell et al. (2021). Dayside and nightside temperatures of 3030^{+150}_{-140} and 1520^{+410}_{-360} K were measured, while the atmospheric brightness modulation showed an unusual $30^\circ \pm 13^\circ$ westward offset in the location of the dayside hot spot. The statistically insignificant phase-curve

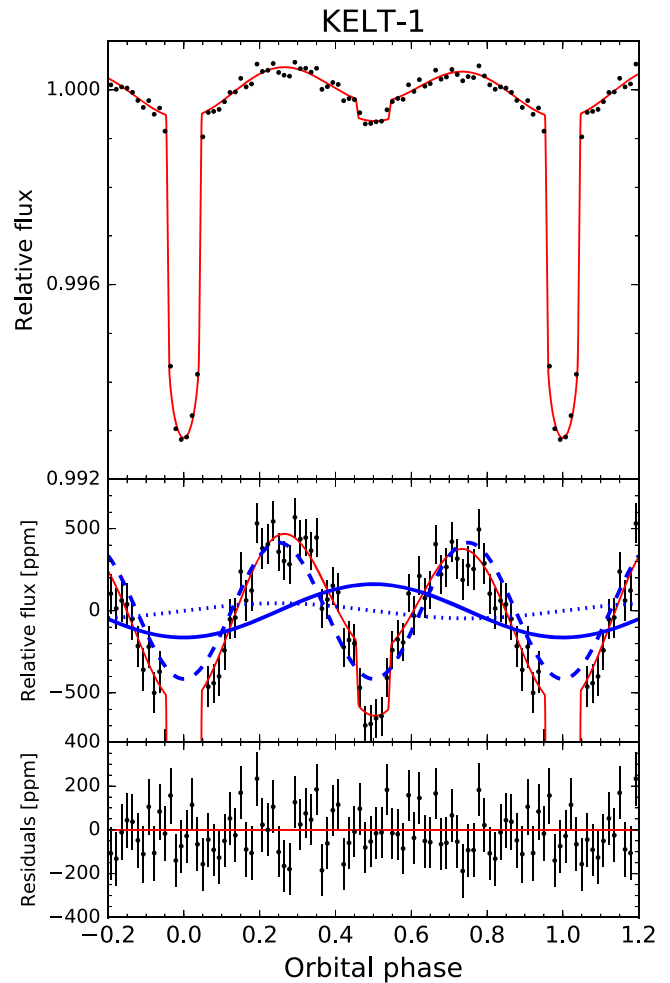


Figure 3. Same as Figure 2 but for KELT-1. The phase-folded light curve is binned in 25 minute intervals.

offset from our TESS light-curve analysis (6^{+18}_{-19} deg) is formally consistent with the Spitzer value at the 1.6σ level.

Mancini et al. (2021) published an independent analysis of the KELT-16 TESS phase curve. Using the PDC light curve, they modeled the brightness distribution across the planet’s atmosphere as a dipole and derived a secondary eclipse depth of 434 ± 42 ppm, which is statistically identical to our value. From their analysis, they also obtained a marginal eastward offset in the dayside hot spot of $25^\circ \pm 14^\circ$ —consistent with our value at better than the 1σ level. We note that their analysis did not account for red noise or systematics modeling, which likely contributed to the significantly smaller uncertainty on the secondary eclipse depth.

3.4. KELT-20

This system was discovered independently by the Kilo-degree Extremely Little Telescope (KELT) survey as KELT-20 (Lund et al. 2017) and the Multi-site All-Sky CAmERA (MASCARA) as MASCARA-2 (Talens et al. 2018). The host star is an A star with an effective temperature of 8730 K and a mass of $1.8 M_\odot$. The highly irradiated transiting planet is a $1.7 R_{\text{Jup}}$ hot Jupiter on a 3.47 day orbit with a 3σ mass upper limit of about $3.5 M_{\text{Jup}}$. TESS observations of this bright $T = 7.6$ mag target occurred during sector 14.

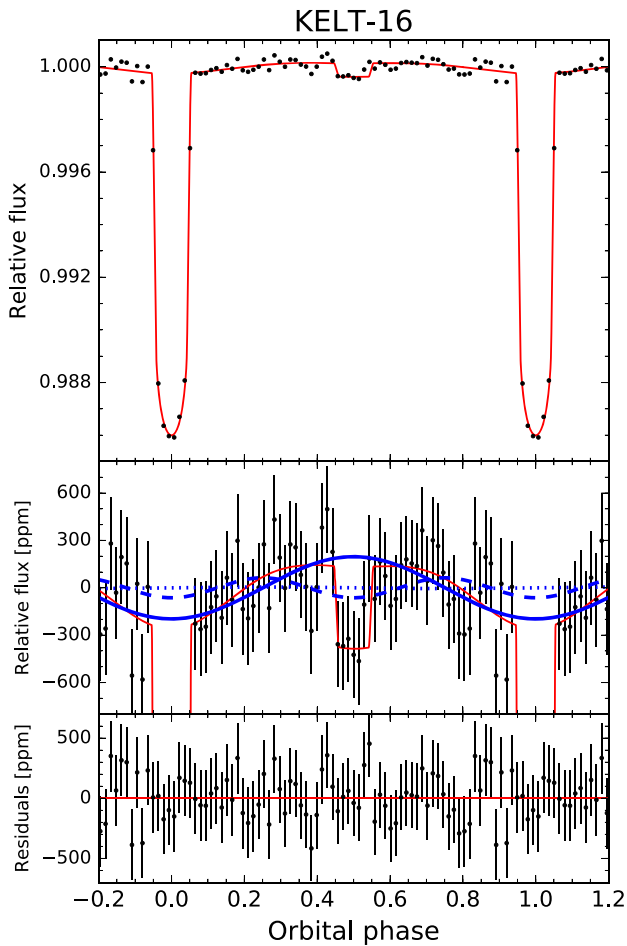


Figure 4. Same as Figure 2 but for KELT-16. The phase-folded light curve is binned in 20 minute intervals.

No discernible ellipsoidal distortion or Doppler-boosting signal was found in the light curve, and given the poorly constrained mass from the discovery papers, we did not apply priors to the respective phase-curve amplitudes in the final fit. The measured secondary eclipse depth and atmospheric brightness modulation semiamplitude are 111^{+35}_{-36} and 43^{+13}_{-11} ppm, respectively. As with the previous targets, no statistically significant phase offset was detected.

The planet radius of $1.761 \pm 0.069 R_{\text{Jup}}$ that we derived from the TESS light-curve fit is consistent with the values listed in both discovery papers. Our measurements of i and a/R_* are slightly more precise than the previously published values, while being consistent at better than 1σ . The full results are given in Table 1; the best-fit phase-curve model and phase-folded light curve are plotted in Figure 5.

3.5. Kepler-13A

Kepler-13A was identified as a candidate planet host early on in the Kepler mission, with subsequent works confirming the existence of a highly irradiated hot Jupiter on a 1.76 day orbit. The availability of long-baseline Kepler data also yielded a well-characterized phase-curve signal and an estimate of the mass ratio from the ellipsoidal distortion amplitude (e.g., Shporer et al. 2011; Szabó et al. 2011; Mazeh et al. 2012). Follow-up imaging with adaptive optics uncovered a bound system of two A-type stars—Kepler-13A and Kepler-13B—with the brighter star, Kepler-13A,

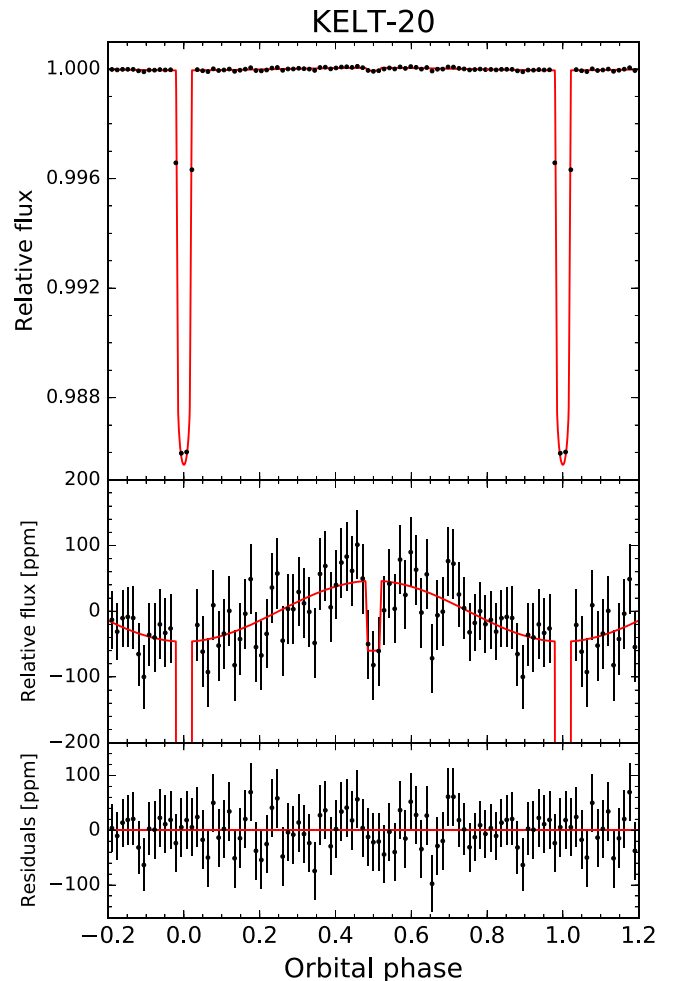


Figure 5. Same as Figure 2 but for KELT-20. The phase-folded light curve is binned in 65 minute intervals. Due to the lack of rigid constraints on the planetary mass, no priors on the ellipsoidal distortion or Doppler-boosting phase-curve amplitudes were applied.

hosting the detected transiting planet and the fainter secondary orbited by a third late-type star, Kepler-13BB (Santerne et al. 2012). High-resolution spectra of the two binary components revealed that Kepler-13A has an effective temperature of 7650 ± 250 K, a roughly solar metallicity of 0.2 ± 0.2 , and a mass of $1.72 \pm 0.10 M_{\odot}$ (Shporer et al. 2014).

An analysis of the full 4 yr Kepler phase curve was carried out by Esteves et al. (2015), who produced high signal-to-noise ratio measurements of phase-curve amplitudes corresponding to all three processes: atmospheric brightness modulation, ellipsoidal distortion, and Doppler boosting. In addition, Shporer et al. (2014) presented secondary eclipse depths in the Spitzer 3.6 and $4.5 \mu\text{m}$ bands, as well as in the K_s band ($2.1 \mu\text{m}$); they showed that the planet’s dayside emission spectrum is consistent with a blackbody brightness temperature of 2750 ± 160 K and an elevated optical geometric albedo $A_g = 0.33^{+0.04}_{-0.06}$.

TESS observed the Kepler-13A system in sectors 14, 15, and 26. The PDC photometry was corrected for the contamination from Kepler-13B by the SPOC pipeline. The transit light curves from the first two sectors were previously analyzed in Szabó et al. (2020), who presented a refined transit ephemeris. That work also confirmed earlier reports of a time-varying impact parameter—a consequence of orbital precession excited by the oblate star and the significant spin–orbit misalignment of

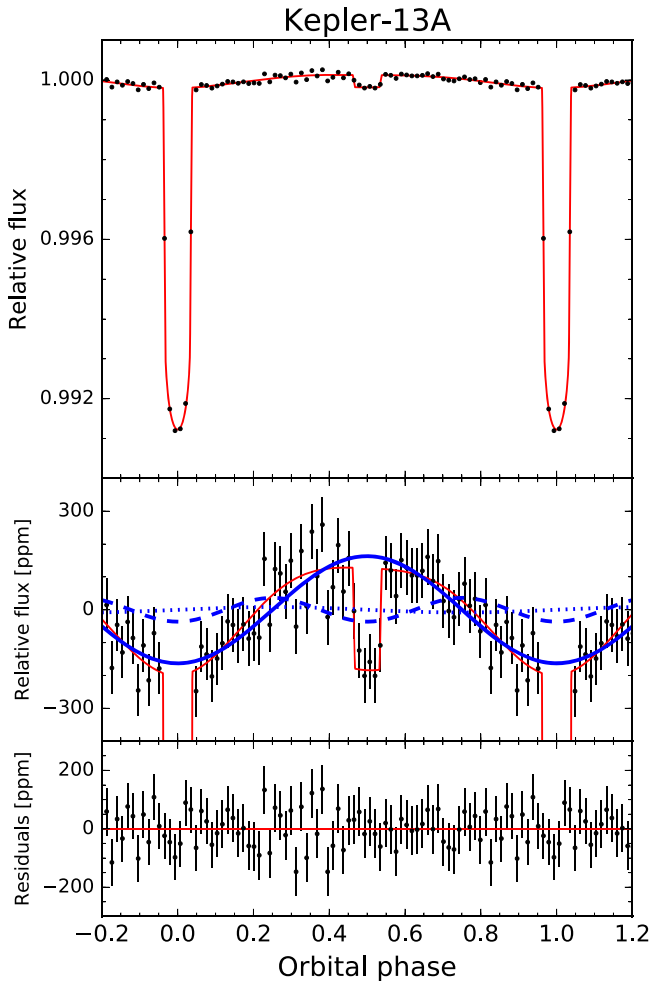


Figure 6. Same as Figure 2 but for Kepler-13A. The phase-folded light curve is binned in 35 minute intervals.

the system (Johnson et al. 2014; Masuda 2015). In our TESS light-curve fit of all three sectors of data, we did not allow for a time-varying impact parameter, since the measured yearly drift of $\Delta b = -0.011$ is significantly smaller than the uncertainty on b from the fit.

We detected significant atmospheric brightness modulation and ellipsoidal distortion semiamplitudes of 151_{-16}^{+15} and 49_{-16}^{+17} ppm, respectively. Meanwhile, the Doppler-boosting amplitude was constrained by a Gaussian prior based on the theoretical value: 6.8 ± 1.7 ppm. We measured a secondary eclipse depth of 301_{-42}^{+46} ppm and a nightside flux that is consistent with zero. Our phase-curve fit that included an offset in the atmospheric brightness modulation yielded a marginal eastward shift in the dayside hot spot of $8^{\circ}9_{-4}^{+5}$. However, just as in the case of the Kepler phase curve, the model with zero offset is statistically favored. The values of R_p/R_* and a/R_* from our TESS light-curve fit (Table 1) agree at much better than 1σ with the extremely precise values measured from the full Kepler light-curve fit in Esteves et al. (2015). The phase-folded TESS light curve is shown in Figure 6.

Similar to the case of HAT-P-7, the Kepler phase curve of Kepler-13A showed an additional modulation of the host star’s brightness at the second harmonic of the orbital period with a semiamplitude of around 7 ppm (Esteves et al. 2013, 2015; Shporer et al. 2014). This is well within the noise of the TESS

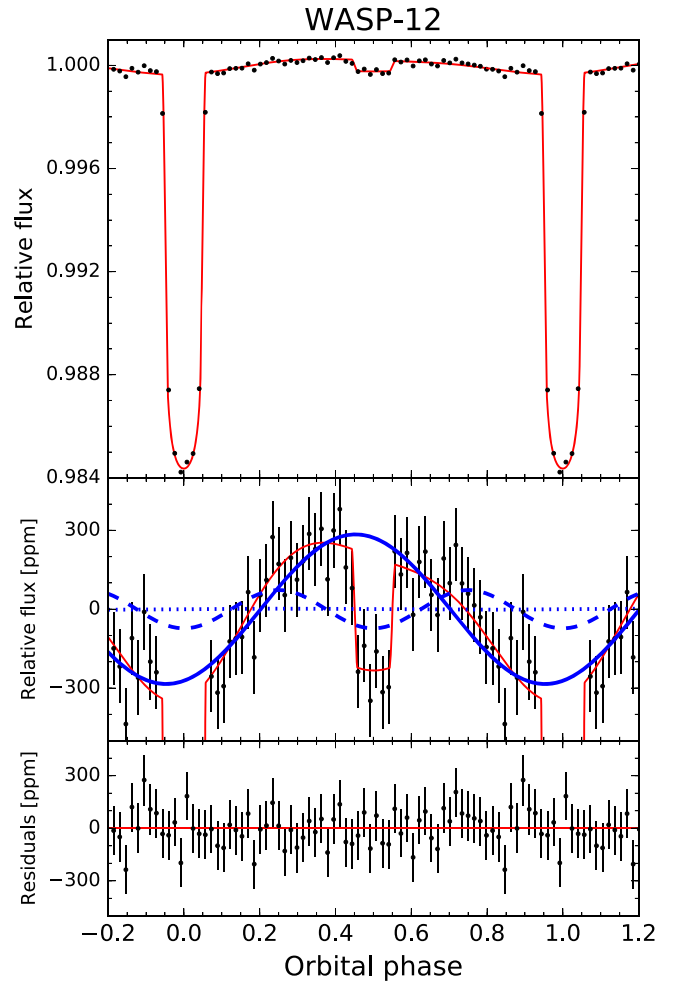


Figure 7. Same as Figure 2 but for WASP-12. The phase-folded light curve is binned in 20 minute intervals.

photometry, and we did not retrieve any significant signal at this harmonic from an unconstrained fit.

Across the temperature range spanned by the published stellar temperature and uncertainties, the gravity-darkening coefficient varies significantly (Claret 2017). As such, we were unable to derive a precise predicted ellipsoidal distortion amplitude. Likewise, the highly uncertain gravity-darkening profile of the star means that our measured ellipsoidal distortion amplitude is consistent with a wide range of planet masses: $4\text{--}11 M_{\text{Jup}}$.

3.6. WASP-12

TESS observations of WASP-12 took place during sector 20. This system consists of a $1.4 M_{\text{Jup}}$ hot Jupiter on a roughly 1 day orbit around a late F star with $T_{\text{eff}} = 6300$ K (Hebb et al. 2009). While WASP-12 is relatively faint ($T = 11.1$ mag), the extreme dayside irradiation has made it an attractive target for atmospheric characterization, particularly in emission. Secondary eclipse observations have been carried out in all four channels of Spitzer/IRAC (Campo et al. 2011; Madhusudhan et al. 2011; Cowan et al. 2012; Stevenson et al. 2014b), as well as with Hubble Space Telescope Wide Field Camera 3 (HST/WFC3; Stevenson et al. 2014b). In addition, full-orbit Spitzer light-curve fits at 3.6 and 4.5 μm were published in Cowan et al. (2012) and Bell et al. (2019). Long-term transit monitoring of WASP-12b has

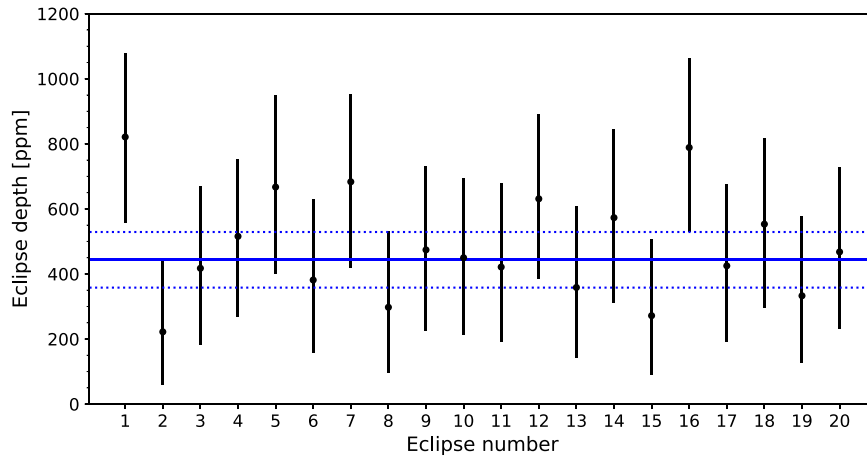


Figure 8. Eclipse depth measurements for each of the 20 full secondary eclipses contained within the TESS light curve of WASP-12. The blue horizontal lines indicate the median global depth and 1σ bounds from the full light-curve fit (Table 1). All individual depths are consistent with the global value to within 1.5σ .

revealed significant orbital decay (Patra et al. 2017; Yee et al. 2020; see Section 4.5). In our TESS phase-curve analysis, we did not consider a time-varying ephemeris, given that the predicted period shortening across one 27 day sector of TESS observations is only ~ 2.5 ms.

We measured an atmospheric brightness modulation with a semiamplitude of 264^{+33}_{-30} ppm that is shifted eastward by $13^{\circ}2 \pm 5^{\circ}7$. The secondary eclipse depth is 443^{+86}_{-85} ppm, and the nightside flux is consistent with zero. We also detected a statistically significant ellipsoidal distortion component with $A_{\text{ellip}} = 80^{+33}_{-35}$ ppm. All of the transit-depth and orbital parameters (R_p/R_* , a/R_* , b ; Table 1) are consistent with the values in the discovery paper (Hebb et al. 2009) at better than the 1σ level. Figure 7 shows the binned and phase-folded TESS light curve, from which the atmospheric brightness and ellipsoidal distortion phase-curve signals are clearly discernible.

In their analysis of the Spitzer phase curves, Bell et al. (2019) measured an eastward offset in the dayside hot spot of $12^{\circ}0 \pm 2^{\circ}0$ at $4.5 \mu\text{m}$ (averaged between the 2010 and 2013 observations), which is consistent with the TESS-band value we derived from our analysis. Meanwhile, the individual phase-curve offset measurements at $3.6 \mu\text{m}$ differed significantly, with the 2010 epoch showing an eastward shift, while the 2013 epoch displayed a westward offset.

Comparing the predicted ellipsoidal distortion semiamplitude (37 ± 8 ppm) with our measured value, we find a slight 1.2σ discrepancy. Similarly, we derived a planetary mass of $3.0 \pm 1.3 M_{\text{Jup}}$ from the measured ellipsoidal distortion amplitude, which differs from the mass listed in the discovery paper ($1.41 \pm 0.10 M_{\text{Jup}}$) at the same significance level.

Bell et al. (2019) reported a first-harmonic phase-curve modulation at $4.5 \mu\text{m}$ that is much larger than expected. Based on the lack of an analogous variation in the $3.6 \mu\text{m}$ phase curves, they concluded that the additional first-harmonic amplitude may be due to gas outflow from the atmosphere of WASP-12b into the host star. In this configuration, the stream of escaping gas is viewed edge-on during quadrature, with the thermal emission from heated CO gas contributing to the extra brightness modulation across the orbit primarily in the $4.5 \mu\text{m}$ bandpass.

Given this mass-loss hypothesis, we propose that the somewhat larger-than-expected first-harmonic phase-curve signal we measured in the TESS light curve might be caused by scattered

starlight off condensates and/or aerosols in the gas stream or thermal emission from superheated gas accreting onto the host star. In order to effectively probe whether the deviation in the TESS-band first-harmonic phase-curve signal from the predicted amplitude is indeed significant, additional photometry from the TESS extended mission is needed.

In addition to the anomalous Spitzer $4.5 \mu\text{m}$ phase curve, several authors have reported possible time variability in the secondary eclipse depth. Hooton et al. (2019) obtained two i' -band observations from two different ground-based telescopes and measured eclipse depths that differed from each other by more than 2σ . Likewise, von Essen et al. (2019) obtained a pair of V-band secondary eclipse depths that are mutually discrepant at the 4.3σ level. While instrumental systematics and observing conditions may be the source of some or all of these eclipse depth mismatches, some level of orbit-to-orbit variability could also be present, especially in the context of the aforementioned mass-loss hypothesis.

To explore the possibility of time-varying eclipse depths in the TESS light curve, we fit each secondary eclipse separately. First, we divided the best-fit systematics model from the light curve and removed the measured atmospheric brightness modulation and ellipsoidal distortion signals. Next, we constructed individual secondary eclipse light curves by selecting data points within 0.1 in orbital phase of each superior conjunction. There are 20 secondary eclipses that lie entirely within the time series and do not contain large gaps due to momentum dumps or trimmed flux ramps. We fit these light curves with the `batman` occultation model while fixing all system parameters except the eclipse depth to the median values from the full MCMC light-curve fit.

Figure 8 shows the measured eclipse depths for each epoch. All of the individual depths lie within 1.5σ of the global value from the full light-curve fit. The standard deviation of the individual eclipse depths is 160 ppm, while the mean uncertainty is 240 ppm. The highest and lowest eclipse depth measurements (from the first two epochs) are consistent at the 1.8σ level. Therefore, we do not find any evidence for significant orbit-to-orbit variability in the dayside brightness of WASP-12b to the level of precision in the TESS data.

Owens et al. (2021) carried out an independent analysis of the TESS phase curve of WASP-12 using both the SAP and PDC light curves. While their methodology differed in several substantive ways, e.g., applying a Gaussian prior to the planet

mass for the ellipsoidal distortion signal modeling and assuming a reflection-dominated atmospheric brightness modulation, their results are broadly consistent with our values. In the case of the PDC light-curve analysis, they obtained a secondary eclipse depth of 577^{+71}_{-72} ppm and a planetary phase-curve semiamplitude of 265 ± 30 ppm, which agree with the corresponding values from our work (443^{+86}_{-85} and 264^{+33}_{-30} ppm) at the 1.2σ and $<0.1\sigma$ levels, respectively. Meanwhile, the secondary eclipse depth they obtained from the SAP light-curve fit is 609^{+74}_{-73} ppm, 1.5σ larger than our value. Notably, Owens et al. (2021) also reported a marginal eastward phase shift in the dayside hot spot that agrees with our measurement at better than the 1σ level ($17^\circ.6 \pm 5^\circ.4$ versus $13^\circ.2 \pm 5^\circ.7$).

3.7. KELT-9

The most extreme of the ultrahot Jupiters discovered to date, KELT-9b is a massive, $\sim 3 M_{\text{Jup}}$ gas giant on a near-polar 1.48 day orbit around an $\sim 10,000$ K $2.3 M_{\odot}$ A0/B9 star (Gaudi et al. 2017). An analysis of the Spitzer $4.5 \mu\text{m}$ full-orbit phase curve indicated a dayside brightness temperature of around 4500 K and a relatively low day–night temperature contrast attributed to the dissociation and recombination of H_2 (Mansfield et al. 2020). Due to the rapid rotation of the host star and the large spin-axis misalignment, the transit light curves of this system show significant aberrations due to gravity darkening. A previous analysis by Ahlers et al. (2020) was dedicated to the detailed modeling of the TESS transit light curves.

Wong et al. (2020d) studied the initially released sector 14 and 15 TESS SPOC light curves of KELT-9 and uncovered several unusual features. First, they detected an unexpected signal at the first harmonic of the orbital period, with the overall modulation significantly offset from the expected phase alignment for ellipsoidal distortion. Using the gravity-darkening model derived by Ahlers et al. (2020), they proposed that this shift is caused by the rotational deformation of the host star and the near-polar orbit of KELT-9b, which results in time-varying insolation of the dayside hemisphere with two maxima and two minima per orbit. This interpretation was supported by numerical modeling of the time-varying stellar irradiation from the gravity-darkening analysis and an analogous signal measured from the planet’s observed thermal phase curve (Mansfield et al. 2020). The second peculiarity was a marginal detection of a phase-curve signal at the second harmonic of the orbital phase, similar to what was reported from the Kepler phase-curve analyses of HAT-P-7 and Kepler-13A. Lastly, they detected a significant sinusoidal stellar pulsation signal with a period of 7.59 hr.

As part of our systematic phase-curve analysis of northern targets, we revisited this system using the updated SPOC light curves. From a methodological standpoint, one difference between our current treatment and the analysis in Wong et al. (2020d) is the more conservative treatment of red noise in this work. Given the attested presence of an additional source of variability at the first harmonic of the orbital period, as well as the stellar pulsations, we modified the phase-curve modeling described in Section 2.3 to fit the KELT-9 light curve.

For the orbital photometric modulations, we applied two different models. In the first case (fit A), we followed the methods in Wong et al. (2020d) and assigned all variations at

the first harmonic of the orbital phase to the host star:

$$\psi_p^A = \bar{f}_p - A_{\text{atm}} \cos(\phi + \delta_{\text{atm}}), \quad (10)$$

$$\psi_*^A = 1 + A_{\text{Dopp}} \sin(\phi) + A_2 \sin(2\phi) + B_2 \cos(2\phi). \quad (11)$$

Here, instead of a single cosine term for ellipsoidal distortion, we used a generic cosine–sine combination to capture the overall variability at the first harmonic; the planet’s flux is modeled in the same way as before.

In the second case (fit B), we were motivated by the hypothesis described in Wong et al. (2020d), wherein the additional signal in the first-harmonic modulation is due to temperature variations on the dayside hemisphere of KELT-9b stemming from time-variable stellar irradiation. As such, we added an additional irradiation term to the planet’s flux while keeping the star’s flux model identical to the nominal case described in Equation (8):

$$\begin{aligned} \psi_p^B = \bar{f}_p - A_{\text{atm}} \cos(\phi + \delta_{\text{atm}}) \\ + A_{\text{irrad}} \cos(2[\phi + \delta_{\text{irrad}}]), \end{aligned} \quad (12)$$

$$\psi_*^B = 1 + A_{\text{Dopp}} \sin(\phi) - A_{\text{ellip}} \cos(2\phi). \quad (13)$$

The parameters A_{irrad} and δ_{irrad} represent the semiamplitude and phase shift of the additional irradiation signal in the planet’s flux. The shape of this model is almost identical to fit A, except for the mid-eclipse flux; in fit A, the shifted first-harmonic signal on the star is still visible when the planet is occulted, while in fit B, the irradiation signal is not visible during mid-eclipse.

To account for the stellar pulsations, we multiplied the combined systematics and phase-curve model with the expression

$$F_{\text{puls}}(t) = 1 + \alpha \sin(\xi) + \beta \cos(\xi), \quad (14)$$

where $\xi \equiv 2\pi(t - T_0)/\Pi$, Π is the pulsation period, and α and β are the coefficients of the sinusoidal pulsation.

Detailed modeling of the gravity-darkened transits is beyond the scope of this paper, and we trimmed the transits from the TESS light curve prior to fitting. We used the results from Ahlers et al. (2020) as Gaussian priors to constrain the planet-to-star radius ratio, orbital parameters, and transit ephemeris. In order to measure the phase shift in the atmospheric brightness modulation at the fundamental of the orbital phase, we applied a prior to the Doppler-boosting semiamplitude based on the predicted value: 2.1 ± 0.3 ppm. For fit B, we applied an additional prior to the host star’s ellipsoidal distortion (44 ± 6 ppm) to allow for the planet’s irradiation signal at the same harmonic to be recovered.

The results of our two separate MCMC fits are shown in Table 2. The semiamplitude and phase offset of the atmospheric brightness modulation, secondary eclipse depth, and nightside flux from fits A and B are statistically identical, as are the stellar pulsation parameter values. The log-probabilities of the two fits differ by less than 0.5. In the following, we designate fit B as the primary analysis, given the theoretically and observationally motivated explanation that the additional signal at the first harmonic stems from the time-varying irradiation of KELT-9b and should therefore be modeled separately from the stellar flux. We measured a secondary eclipse of 630^{+18}_{-17} ppm and a nightside flux of 87 ± 22 ppm. The atmospheric brightness modulation, with a semiamplitude

Table 2
Results from KELT-9 Phase-curve Fits

Parameter	Fit A ^a		Fit B ^a	
	Value	Error	Value	Error
Orbital and Transit Parameters^b				
R_p/R_*	0.0791	$^{+0.0017}_{-0.0018}$	0.0790	$^{+0.0018}_{-0.0019}$
T_0	710.10518	0.00025	710.10522	0.00027
P (days)	1.4811235	0.0000010	1.4811235	0.0000011
b	0.14	0.04	0.14	0.04
a/R_*	3.18	0.03	3.18	0.03
Phase-curve Parameters				
\bar{f}_p (ppm)	356	$^{+17}_{-18}$	308	15
A_{atm} (ppm)	271.6	$^{+9.0}_{-9.2}$	271.9	$^{+9.0}_{-8.9}$
δ_{atm} (deg)	2.6	1.4	2.6	$^{+1.4}_{-1.3}$
A_{ellip} (ppm)	[44]	[6]
A_{Dopp} (ppm)	[2.1] ^c	[0.3] ^c	[2.1]	[0.3]
A_2 (ppm)	-30.3	$^{+6.0}_{-6.1}$
B_2 (ppm)	7.7	$^{+8.3}_{-8.4}$
A_{irrad} (ppm)	60.1	$^{+9.4}_{-9.1}$
δ_{irrad} (deg)	16.0	$^{+3.7}_{-3.2}$
Stellar Pulsation Parameters				
Π (hr)	7.5851	0.0012	7.5851	0.0011
α (ppm)	95.5	5.8	96.6	$^{+5.9}_{-6.2}$
β (ppm)	87.3	$^{+5.8}_{-5.9}$	86.4	$^{+6.2}_{-6.0}$
Derived Parameters				
D_d (ppm) ^d	627	$^{+17}_{-18}$	630	$^{+18}_{-17}$
D_n (ppm) ^d	84	$^{+21}_{-23}$	87	22

Notes.

^a Fit A: the combined first-harmonic photometric modulation, parameterized by A_2 and B_2 , is attributed to the stellar flux. Fit B: the ellipsoidal distortion of the host star is assumed to occur according to predictions; the additional flux variation at the first harmonic is the planet's response to time-varying stellar irradiation.

^b In these fits, the parameters were constrained by Gaussian priors derived from Ahlers et al. (2020), and T_0 is given in BJD_{TDB}-2,458,000.

^c Square brackets denote applied Gaussian priors.

^d Here D_d and D_n are the dayside and nightside fluxes, respectively. The dayside flux is equivalent to the secondary eclipse depth.

of $271.9^{+9.0}_{-8.9}$ ppm, has a phase offset of $2.6^{+1.3}_{-1.3}$. Similar to the case of KELT-1, the phase shift in the TESS band is significantly smaller than the corresponding infrared measurement at $4.5 \mu\text{m}$ ($18.7^{+2.1}_{-2.3}$; Mansfield et al. 2020). The additional irradiation signal in the planet's flux has a semiamplitude of $A_{\text{irrad}} = 60.1^{+9.4}_{-9.1}$ ppm and comes to maximum roughly 1.6 hr before mid-eclipse. The phase-folded TESS light curve and best-fit phase-curve model are plotted in Figure 9.

Comparing the results of our analysis with those in Wong et al. (2020d), we find that the secondary eclipse, nightside flux, and atmospheric brightness modulation semiamplitude values are mutually consistent at much better than the 1σ level. Meanwhile, the new phase shift δ_{atm} presented here is 1.5σ smaller than the previous measurement. We obtained a stellar pulsation period of 7.5851 ± 0.0011 hr and a peak-to-peak pulsation amplitude of 260 ± 12 ppm, which differ from the corresponding values from Wong et al. (2020d) by 1.3σ and 2.1σ , respectively. We note that TESS observations in sectors 14 and 15 were particularly affected by scattered light on the detectors, and the updated SPOC data contain significantly more flagged points than the initially released photometry (see,

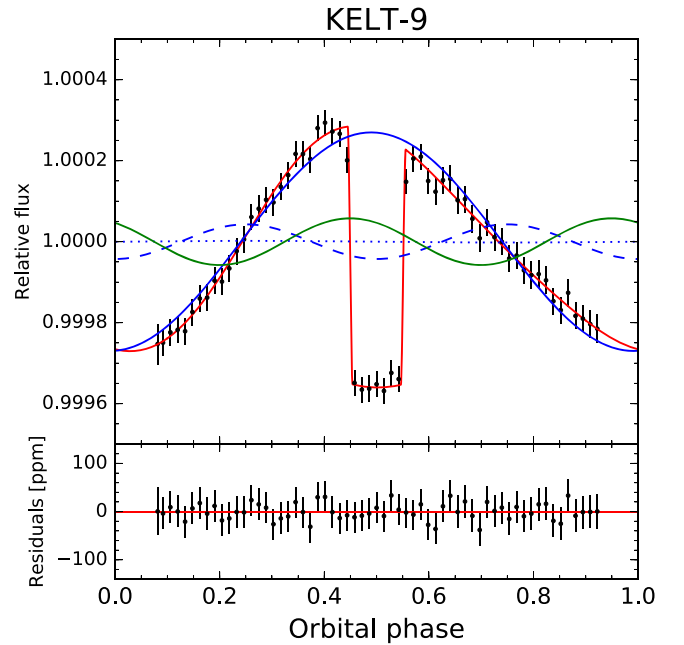


Figure 9. Phase-folded and systematics-corrected TESS light curve of KELT-9, binned in 30 minute intervals. The transits have been removed. The solid, dashed, and dotted blue curves are the best-fit atmospheric brightness modulation, ellipsoidal distortion, and Doppler-boosting signals. The solid green curve is the additional first-harmonic modulation in the planet's flux due to time-variable irradiation from the oblate host star over the course of its near-polar orbit.

for example, the large gaps in the untrimmed SPOC data in Appendix B). The slight discrepancies between the current fit and the previous results in Wong et al. (2020d) may be indicative of some systematic biases in the earlier version of the photometry.

When fitting for an additional phase-curve signal at the second harmonic of the orbital phase, we obtained a semiamplitude of 15 ± 7 ppm, consistent with our previous measurement of 16 ± 4 ppm. However, given the enhanced per-point uncertainty needed to account for red noise at longer timescales, the significance of the present detection is much lower, and including the second harmonic term in the model led to large increases in the AIC and BIC. Therefore, we cannot claim a detection of photometric variability at this harmonic. Future light curves from the TESS extended mission will provide improved sensitivity to low-amplitude phase-curve signals and allow us to definitely determine whether a second-harmonic signal exists in the KELT-9 system.

3.8. Marginal Detections and Nondetections

No statistically significant phase-curve amplitudes or secondary eclipse depths were measured in eight of the 15 systems selected for detailed analysis. Table 3 lists these targets, along with the predicted secondary eclipse depths from Equation (1). Also provided are the marginal detections or upper-limit constraints on the secondary eclipse depths and atmospheric brightness modulation semiamplitudes that were measured from phase-curve fits that included only those components in the astrophysical model. In all cases, the eclipse depth measurements are broadly consistent with the predicted values.

Table 3
Marginal Detections and Nondetections

Target	Sector	T^a	$D_{d,\text{pred}}^b$	$D_{d,\text{meas}}^b$	A_{atm}^c
HAT-P-36	22	11.6	170	150^{+100}_{-90}	<70
KELT-23A	14–17, 21, 23	9.8	70	<50	<10
Qatar-1	17, 21, 24, 25	11.8	80	88^{+66}_{-47}	23^{+25}_{-24}
TrES-3	25, 26	11.6	160	140^{+100}_{-70}	51^{+30}_{-31}
WASP-3	26	10.1	170	150 ± 70	38^{+26}_{-23}
WASP-92	23–25	12.4	120	160^{+120}_{-110}	<70
WASP-93	17	10.6	110	140^{+130}_{-80}	30^{+24}_{-25}
WASP-135	26	12.3	150	120^{+210}_{-150}	<160

Notes.^a Apparent magnitude in the TESS bandpass.^b Predicted and measured secondary eclipse depths in parts per million. Predictions assume $A_g = 0.1$ and no day–night heat recirculation.^c Measured semiamplitudes (or 2σ upper limits) of the atmospheric brightness modulation in parts per million.

Given the absence of any robust phase-curve signals in the TESS photometry, we carried out simplified fits with a flat out-of-transit model flux (i.e., transit-only fits). The results of these fits are presented in Table 4. When comparing the parameter values with those from the respective discovery papers, we generally find good agreement and a moderate increase in the precision of the transit parameters (R_p/R_* , b , and a/R_*) in some cases, yielding improved constraints on the derived parameters, such as orbital semimajor axis a , inclination i , and planetary radius R_p . The systematics-corrected and phase-folded transit light curves are included in the compilation plot in Figure 1.

The handful of instances where the new parameter values differ somewhat significantly ($>2\sigma$) from previous results are described below. KELT-23A was observed during six TESS sectors, and the high data volume produced the most precise transit shape and limb-darkening parameters of any target studied in this paper. We measured $b = 0.523 \pm 0.011$ and

Table 4
Results from Transit-only Light-curve Fits

Parameter	HAT-P-36		KELT-23A		Qatar-1		TrES-3	
	Value	Error	Value	Error	Value	Error	Value	Error
Fitted Parameters								
R_p/R_*	0.1226	$-0.0011^{+0.0012}$	0.13276	$-0.00045^{+0.00050}$	0.1458	$-0.0018^{+0.0019}$	0.1675	$-0.0043^{+0.0030}$
$T_{0,\text{MCMC}}$ (BJD _{TDB} –2,458,000) ^a	911.42294	$-0.00014^{+0.00014}$	769.612269	$-0.00033^{+0.00034}$	959.129856	$-0.00080^{+0.00079}$	1,008.35093	0.00010
$T_{0,\text{PB}}$ (BJD _{TDB} –2,458,000) ^a	911.42299	$-0.00030^{+0.00031}$	769.612278	$-0.00060^{+0.00058}$	959.12981	$-0.00014^{+0.00013}$	1,008.35101	$-0.00022^{+0.00020}$
P (days)	1.327355	$-0.00021^{+0.00022}$	2.25528773	$-0.000077^{+0.000073}$	1.4200228	$-0.000012^{+0.000013}$	1.3061842	$-0.000085^{+0.000087}$
b	0.08	$-0.17^{+0.20}$	0.523	0.011	0.603	$-0.023^{+0.025}$	0.836	$-0.026^{+0.020}$
a/R_*	4.762	$-0.063^{+0.080}$	7.614	$-0.043^{+0.046}$	6.41	$-0.11^{+0.10}$	5.83	0.10
γ_1^b	0.881	$-0.094^{+0.085}$	0.841	0.026	1.15	$-0.09^{+0.11}$	1.07	$-0.39^{+0.35}$
γ_2^b	–0.61	0.56	–0.01	$-0.23^{+0.25}$	–0.45	$-0.66^{+0.75}$	–0.31	$-0.65^{+0.75}$
Derived Parameters								
i (deg)	89.1	$-2.3^{+2.1}$	86.06	0.10	84.60	$-0.30^{+0.28}$	81.77	$-0.30^{+0.40}$
u_1	0.23	0.11	0.335	$-0.053^{+0.056}$	0.37	$-0.15^{+0.17}$	0.34	$-0.28^{+0.22}$
u_2	0.42	0.23	0.170	$-0.097^{+0.091}$	0.41	$-0.29^{+0.25}$	0.33	$-0.29^{+0.23}$
a (au)	0.0243	0.0013	0.03527	0.00057	0.02453	0.00085	0.0217	0.0013
R_p (R_{Jup})	1.308	0.068	1.287	0.020	1.168	0.038	1.307	0.080
Parameter	WASP-3		WASP-92		WASP-93		WASP-135	
	Value	Error	Value	Error	Value	Error	Value	Error
Fitted Parameters								
R_p/R_*	0.1051	$-0.0012^{+0.0016}$	0.1052	$-0.0019^{+0.0034}$	0.1039	$-0.0038^{+0.0032}$	0.1402	$-0.0018^{+0.0033}$
$T_{0,\text{MCMC}}$ (BJD _{TDB} –2,458,000)	1,023.18948	0.00015	971.31989	$-0.00031^{+0.00034}$	779.31211	$-0.00046^{+0.00045}$	1,021.71852	$-0.00028^{+0.00031}$
$T_{0,\text{PB}}$ (BJD _{TDB} –2,458,000)	1,023.18947	$-0.00029^{+0.00025}$	971.32011	$-0.00058^{+0.00054}$	779.31199	0.00062	1,021.71876	$-0.00072^{+0.00048}$
P (days)	1.846866	$-0.000036^{+0.000037}$	2.174663	$-0.000030^{+0.000029}$	2.73253	$-0.00014^{+0.00015}$	1.401403	$-0.000052^{+0.000045}$
b	0.40	$-0.07^{+0.12}$	0.53	$-0.08^{+0.18}$	0.889	$-0.023^{+0.029}$	0.706	$-0.037^{+0.061}$
a/R_*	5.40	$-0.19^{+0.18}$	5.81	$-0.51^{+0.34}$	6.12	$-0.31^{+0.27}$	5.63	$-0.31^{+0.23}$
γ_1	0.73	$-0.09^{+0.10}$	0.84	0.19	0.86	$-0.50^{+0.38}$	0.68	$-0.35^{+0.29}$
γ_2	–0.38	$-0.51^{+0.62}$	–0.53	$-0.64^{+0.68}$	–0.37	$-0.57^{+0.66}$	–0.28	$-0.42^{+0.66}$
Derived Parameters								
i (deg)	85.8	$-1.4^{+1.0}$	84.7	$-2.1^{+1.2}$	81.65	$-0.66^{+0.61}$	82.81	$-0.94^{+0.70}$
u_1	0.21	$-0.10^{+0.12}$	0.22	0.14	0.23	$-0.29^{+0.16}$	0.18	$-0.18^{+0.13}$
u_2	0.29	$-0.25^{+0.20}$	0.37	$-0.30^{+0.25}$	0.32	$-0.28^{+0.23}$	0.23	$-0.32^{+0.16}$
a (au)	0.0329	0.0024	0.0362	0.0031	0.0434	0.0023	0.0251	0.0018
R_p (R_{Jup})	1.340	0.089	1.373	0.069	1.541	0.066	1.310	0.072

Notes.^a Mid-transit times derived from the MCMC and PB analyses.^b Modified limb-darkening parameters $\gamma_1 \equiv 2u_1 + u_2$ and $\gamma_2 \equiv u_1 - 2u_2$.

Table 5
Dayside Blackbody Brightness Temperatures and Geometric Albedos

Planet	$D_{d,TESS}$ (ppm) ^a	$D_{d,3.6}$ (ppm) ^a	$D_{d,4.5}$ (ppm) ^a	T_{day} (K)	A_g ^b	χ_r ^{2c}	Reference ^d
Year 1							
WASP-4b	120^{+80}_{-70}	3190 ± 310	3430 ± 270	1954 ± 67	0.09 ± 0.09	2.39	Beer et al. (2011)
WASP-5b	31^{+73}_{-55}	1970 ± 280	2370 ± 240	2000 ± 90	<0.32	0.17	Baskin et al. (2013)
WASP-18b	339 ± 21	3040 ± 190	3790 ± 150	3046 ± 66	<0.03	1.32	Maxed et al. (2013)
WASP-19b	470^{+130}_{-110}	4850 ± 240	5840 ± 290	2204 ± 49	0.17 ± 0.07	0.49	Wong et al. (2016)
WASP-36b	90^{+100}_{-70}	914 ± 578	1953 ± 544	1440 ± 160	0.16 ± 0.15	0.38	Garhart et al. (2020)
WASP-43b	170 ± 70	3230 ± 60	3830 ± 80	1655 ± 38	0.13 ± 0.06	38.3	Stevenson et al. (2017)
WASP-46b	230^{+140}_{-110}	1360 ± 701	4446 ± 589	1880 ± 120	0.38 ± 0.27	5.87	Garhart et al. (2020)
WASP-64b	230^{+130}_{-110}	2859 ± 270	2071 ± 471	1989 ± 86	0.38 ± 0.26	8.01	Garhart et al. (2020)
WASP-77Ab	53^{+32}_{-22}	2016 ± 94	2487 ± 127	1840 ± 33	0.06 ± 0.05	1.49	Garhart et al. (2020)
WASP-78b	210^{+100}_{-90}	2001 ± 218	2013 ± 351	2550 ± 130	<0.56	0.76	Garhart et al. (2020)
WASP-100b	94 ± 17	1267 ± 98	1720 ± 119	2356 ± 67	0.22 ± 0.08	1.22	Garhart et al. (2020)
WASP-121b	486 ± 59	3685 ± 114	4684 ± 121	2592 ± 44	0.26 ± 0.06	2.89	Garhart et al. (2020)
Year 2							
HAT-P-7b	127^{+33}_{-32}	1560 ± 90	1900 ± 60	2692 ± 62	<0.28	0.24	Wong et al. (2016)
KELT-1b	388^{+67}_{-65}	1877 ± 58	2083 ± 70	2978 ± 56	0.45 ± 0.16	0.62	Beatty et al. (2019)
Kepler-13Ab	301^{+46}_{-42}	1560 ± 310	2220 ± 230	2786 ± 160	0.53 ± 0.15	0.84	Shporer et al. (2014)
Qatar-1b	88^{+66}_{-47}	2100 ± 200	3000 ± 200	1539 ± 41	0.14 ± 0.11	0.07	Keating et al. (2020)
TrES-3b	140^{+130}_{-80}	3450 ± 350	3470 ± 540	1737 ± 70	0.14 ± 0.13	1.84	Fressin et al. (2010)
WASP-3b	150 ± 70	2090^{+400}_{-280}	2820 ± 120	2372 ± 66	<0.55	0.44	Rostron et al. (2014)
WASP-12b	443^{+86}_{-85}	3854 ± 88^e	4160 ± 100^e	2710 ± 55	0.13 ± 0.06	7.11	Bell et al. (2019)
WASP-33b ^f	320 ± 37	3506 ± 173	4250 ± 160	3145 ± 65	<0.08	1.09	Zhang et al. (2018)

Notes.

^a Secondary eclipse depths measured in the TESS bandpass and the 3.6 and 4.5 μm Spitzer/IRAC bandpasses.

^b For marginal cases, 2σ upper limits are provided.

^c Reduced χ^2 value of the best-fit model to the three secondary eclipse measurements.

^d Literature references for the Spitzer secondary eclipse measurements.

^e Weighted averages of eclipse depth measurements from two epochs.

^f TESS secondary eclipse depth taken from von Essen et al. (2020).

$a/R_* = 7.614^{+0.043}_{-0.046}$, which are discrepant from the discovery paper values ($b = 0.576^{+0.024}_{-0.027}$, $a/R_* = 7.13^{+0.16}_{-0.15}$; Johns et al. 2019) at the 1.8σ and 2.9σ levels, respectively. For Qatar-1, our impact parameter $b = 0.603^{+0.023}_{-0.025}$ is 2.8σ larger than the value $b = 0.696^{+0.021}_{-0.024}$ from Alsubai et al. (2011). Meanwhile, the more recent transit light-curve analysis in Maciejewski et al. (2015) presented a more consistent set of parameter values: $b = 0.63 \pm 0.02$ and $a/R_* = 6.319^{+0.070}_{-0.068}$.

4. Discussion

Our systematic light-curve analysis of targets from the second year of the TESS mission yielded seven systems with robust secondary eclipse and phase-curve signals. Some overarching observations include the following: (1) the only orbiting companion to show significant nightside flux in the TESS bandpass is KELT-9b, (2) KELT-9b and WASP-12b are the only systems in the list for which statistically significant phase shifts in the atmospheric brightness modulation were detected, and (3) the strengths of the ellipsoidal distortion modulations measured for KELT-1, Kepler-13A, and WASP-12 are broadly consistent with theoretical predictions. In this section, we use the results of our phase-curve fits to explore the atmospheric properties of these systems and derive updated transit ephemerides.

4.1. Dayside Temperatures and Geometric Albedos

The dayside temperature of an orbiting planet cannot be reliably determined from the system's brightness ratio in a single bandpass without making assumptions about the amount of reflected starlight and/or the level of heat redistribution across the atmosphere. In order to break this degeneracy, additional secondary eclipse measurements at other wavelengths are needed, preferably in the thermal infrared, where the emission from the companion's atmosphere dominates any reflected starlight.

Spitzer secondary eclipse measurements have been published for several of the systems studied in our TESS phase-curve analysis. Just as in our Year 1 analysis, we only considered systems for which secondary eclipse depths were obtained in both the 3.6 and 4.5 μm bandpasses. Seven targets satisfy this criterion—HAT-P-7, KELT-1, Kepler-13A, Qatar-1, TrES-3, WASP-3, and WASP-12. We list the eclipse depths and references in Table 5. Whenever possible, we chose Spitzer eclipse depths that were obtained from combined analyses of the 3.6 and 4.5 μm full-orbit phase-curve fits, given the possibility of a significant bias in the measured values when not properly accounting for the variable out-of-eclipse flux (e.g., Bell et al. 2019). We also included WASP-33, combining the TESS-band secondary eclipse depth measured by von Essen et al. (2020) with the Spitzer results from Zhang et al. (2018).

For each system, we assumed that the thermal emission from the companion's dayside hemisphere in the three bandpasses is

consistent with a single blackbody (i.e., the three wavelength ranges probe similar pressure levels within the atmosphere) and carried out a simple simultaneous fit of the three secondary eclipse depths to Equation (1). Here the measured planetary temperature T_p is designated as the dayside blackbody brightness temperature T_{day} . To account for possible excess flux at short wavelengths due to reflected starlight off clouds and/or hazes, we allowed the geometric albedo A_g to vary freely when modeling the TESS-band secondary eclipse depth; meanwhile, A_g was fixed to zero at the Spitzer wavelengths.

Following the methods in Paper I, we used PHOENIX stellar models (Husser et al. 2013) and derived a best-fit interpolation polynomial as a function of (T_{eff} , $\log g$, $[\text{Fe}/\text{H}]$) for the band-integrated stellar flux in each of the three bandpasses. These polynomials were sampled in a Monte Carlo fashion in order to propagate the stellar parameter uncertainties to our temperature and albedo estimates. In the MCMC fitting procedure, we applied Gaussian priors to R_p/R_* , a/R_* , T_{eff} , $\log g$, and $[\text{Fe}/\text{H}]$ based on literature values and our light-curve fit results (Tables 1 and 4).

There was a minor issue in our implementation of the TESS transmission function in Paper I due to the erroneous inclusion of the photon-to-energy unit conversion factor λ/hc in Equation (1); this factor is needed for computing the CoRoT, Kepler, and Spitzer band-integrated fluxes, as the corresponding transmission functions are provided in photon units. In this paper, we have corrected the calculations and report updated values for all planets in our Year 1 and Year 2 TESS phase-curve sample. The alterations to the best-fit values are negligible (typically $<0.1\text{--}0.2\sigma$).

Table 5 presents the dayside brightness temperature and TESS-band geometric albedo estimates; 2σ upper limits are provided in cases where the albedo value is consistent with zero to within 1σ . We also list the reduced χ^2 values for each fit. Most systems show $\chi_r^2 \lesssim 2$. Meanwhile, four planets—WASP-12b, WASP-43b, WASP-46b, and WASP-64b—have secondary eclipse depths that are not well described by our simple blackbody+reflectivity model. These discrepancies may indicate that the three photometric bandpasses are probing pressure levels within the atmosphere that have significantly different temperatures. For all of these cases except WASP-46b, the brightness temperature derived from the Spitzer $4.5\ \mu\text{m}$ eclipse depth alone is significantly lower than the $3.6\ \mu\text{m}$ brightness temperature.

One plausible explanation for this discrepancy is CO absorption. This scenario is particularly applicable to WASP-12b. Within the framework of the atmospheric mass-loss hypothesis (see Section 3.6 and Bell et al. 2019), the column of escaped gas is oriented along the line of sight at superior conjunction. The CO, which has strong absorption features within the $4.5\ \mu\text{m}$ bandpass, may block a significant portion of the thermal emission from the planet, resulting in a lower apparent brightness temperature. Detailed modeling of the HST/WFC3 and Spitzer secondary eclipse depths of WASP-43b revealed strong absorption from CO within the Spitzer $4.5\ \mu\text{m}$ bandpass, leading to a significant deviation from a blackbody emission spectrum (Stevenson et al. 2017).

While most of the TESS-band geometric albedos we measured lie within 2σ of zero, KELT-1b and Kepler-13Ab show very high reflectivity. Previous atmospheric modeling of the dayside emission of KELT-1b, including the TESS-band secondary eclipse depth, corroborates our conclusion of a significantly nonzero albedo (Beatty et al. 2020). For Kepler-13Ab, a joint fit of the Spitzer and Kepler secondary eclipse

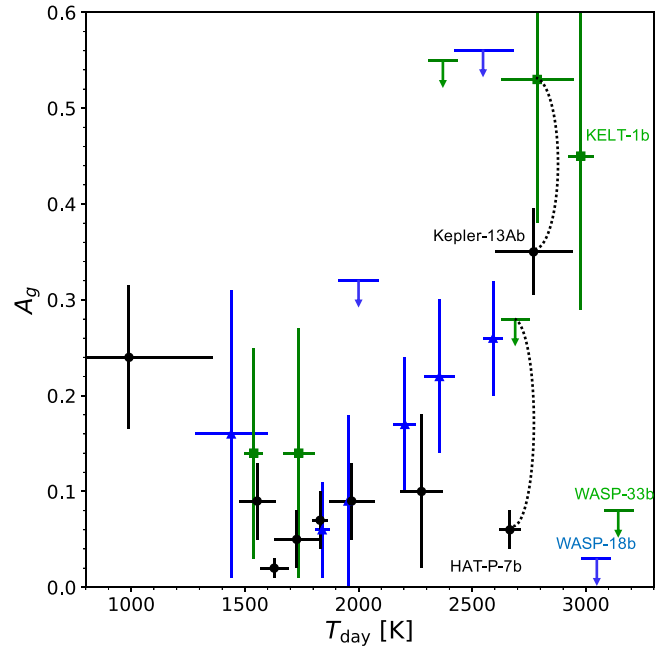


Figure 10. Two-parameter plot showing the relationship between geometric albedo A_g and dayside blackbody brightness temperature T_{day} , as derived from our joint fits of visible-wavelength secondary eclipse depths and Spitzer measurements. The blue triangles and green squares indicate the systems from the first and second year of the TESS primary mission, respectively; the black circles indicate the Kepler-/CoRoT-band geometric albedos for the targets that were observed by those missions. For HAT-P-7b and Kepler-13Ab, which were observed by both Kepler and TESS, dashed curves connect the corresponding Kepler- and TESS-band geometric albedos and T_{day} measurements from the Spitzer+Kepler and Spitzer+TESS fits. For several objects, 2σ upper limits on the geometric albedo are shown by the arrows. Objects with poorly fit emission spectra ($\chi_r^2 > 5$) are not shown. Some notable planets discussed in the text are labeled.

observations yields a Kepler-band geometric albedo of $0.35^{+0.04}_{-0.05}$ and a dayside brightness temperature of $2770 \pm 170\ \text{K}$ (Paper I), which are statistically consistent with our values derived from the Spitzer+TESS fit. Through an analogous calculation for HAT-P-7b using the Kepler-band secondary eclipse depth measurement from Esteves et al. (2015), we obtained $T_{\text{day}} = 2666 \pm 47\ \text{K}$ and a Kepler-band geometric albedo of $A_g = 0.06 \pm 0.02$.

4.2. Revisiting the Albedo–Dayside Temperature Trend

In Paper I, we calculated dayside brightness temperatures and TESS-band geometric albedos following the methodology outlined in the previous subsection. We then searched for trends between albedo and various other system parameters, such as dayside temperature, stellar metallicity, and planetary surface gravity. A marginal 2.2σ positive correlation between the TESS-band geometric albedo and dayside temperature was detected among planets with $1500\ \text{K} < T_{\text{day}} < 3000\ \text{K}$, with the significance increasing to 5.5σ when including additional data points derived from Kepler and CoRoT secondary eclipses. Meanwhile, the very low albedo of WASP-18b ($T_{\text{day}} = 3046 \pm 66\ \text{K}$) indicates a sharp break in the emergent trend for the most extremely irradiated hot Jupiters.

Having expanded the body of self-consistent dayside temperatures and TESS-band geometric albedos with the results of our Year 2 analysis, we revisited the apparent trend between these two parameters. Figure 10 plots the geometric albedo as a

function of dayside blackbody brightness temperature; we have omitted targets whose secondary eclipses are poorly fit by the blackbody+reflectivity model ($\chi_r^2 > 5$). The colored points indicate the measurements we obtained from TESS-band secondary eclipses, while the black points denote the analogously derived values from Kepler or CoRoT eclipse depths (see Table 4 in Paper I). For objects with both TESS and Kepler observations (HAT-P-7b and Kepler-13Ab), we plot both the TESS- and Kepler-band geometric albedos derived from the Spitzer+TESS and Spitzer+Kepler fits, respectively.

The positive correlation between A_g and T_{day} remains apparent in the larger data set. The addition of the KELT-1b data point anchors the high-temperature end of the trend. At even higher temperatures, the low TESS-band geometric albedo of WASP-33b supports the previous suggestion that the dayside atmospheres of the hottest ultrahot Jupiters strongly deviate from the aforementioned correlation and are consistent with zero reflectivity.

Just as in our Year 1 analysis, we carried out an MCMC linear fit to the expanded sample, focusing on systems in the range $1500 \text{ K} < T_{\text{day}} < 3000 \text{ K}$. While this temperature range was primarily selected to allow one-to-one comparison with the results in Paper I, the choice was also motivated by both theoretical and empirical considerations. Previous cloud modeling in the context of optical atmospheric reflectivity has shown that while cooler planets can host a wide array of condensate species, resulting in complicated trends in predicted geometric albedo, silicate clouds are expected to largely disappear across the dayside hemisphere at temperatures above $1500\text{--}1700 \text{ K}$ (e.g., Parmentier et al. 2016). Visual inspection of the A_g versus T_{day} trend in Figure 10 clearly indicates a local minimum in geometric albedo near zero at around $1500\text{--}1600 \text{ K}$, with the small handful of cooler planets having somewhat higher but poorly constrained albedo values and a possible reversal in the trend seen among hotter targets. Meanwhile, the two hottest planets with $T_{\text{day}} > 3000 \text{ K}$ are clear outliers. We experimented with fitting higher-order polynomials to the albedos in both the constrained and full temperature ranges and found that the linear fit to objects in the range $1500 \text{ K} < T_{\text{day}} < 3000 \text{ K}$ yielded the smallest reduced χ^2 and lowest BIC.

When using only the TESS-derived albedos, the addition of the Year 2 targets increases the significance of the positive correlation between TESS-band geometric albedo and dayside temperature from 2.2σ to 3.1σ . Here the inclusion of KELT-1b as an additional high-albedo object is crucial in strengthening the detection of an overall trend. We also considered the Kepler-/CoRoT-band albedos independently and obtained a similar trend between A_g and T_{day} at 4.6σ significance. The TESS, Kepler, and CoRoT bandpasses overlap considerably, with the latter two having almost identical effective wavelengths and comparable bandwidths and the TESS bandpass situated roughly 150 nm redder, on average. Following our previous Year 1 analysis, we carried out a combined MCMC fit to the TESS-, Kepler-, and CoRoT-derived albedos and retrieved a very robust 5.7σ trend. We note that geometric albedo varies with wavelength, and the Kepler and CoRoT bandpasses are more sensitive to bluer wavelengths, where the effect of Rayleigh scattering on the dayside reflectivity is more pronounced. Nevertheless, the presence of a significant trend between A_g and T_{day} in both the TESS-derived and the Kepler-/CoRoT-derived data sets suggests a broader correlation between atmospheric reflectivity and dayside temperature that holds across the visible wavelength range.

In the overall trend of A_g versus T_{day} , HAT-P-7b stands out as an outlier, particularly when considering the Kepler-derived geometric albedo value. A recent reanalysis of the Spitzer $4.5 \mu\text{m}$ phase curve of this planet has revealed some unusual properties (Bell et al. 2021): (1) the day–night temperature contrast is very low ($\sim 400 \text{ K}$), implying much more efficient heat transport between the day- and nightside hemispheres than other hot Jupiters with similar levels of stellar irradiation; (2) the nightside brightness temperature of roughly 2500 K is significantly hotter than all other hot Jupiters with phase-curve measurements, making HAT-P-7b comparable to the extremely irradiated KELT-9b; and (3) the corresponding inferred Bond albedo, derived from simple thermal balance considerations, is negative (see Table 8), suggesting an additional source of heat across the planet’s surface. It is evident that HAT-P-7b presents a challenging case for interpreting the global atmospheric thermal energy budget. We experimented with omitting this object from the TESS-band albedo–dayside temperature trend analysis and obtained a much stronger positive correlation at 3.7σ significance.

The addition of targets from the second year of the TESS mission primarily serves to solidify the detection of a positive correlation between A_g and T_{day} reported in Paper I. Here we briefly reiterate some possible explanations for the trend that were postulated in that work. While most condensate species are expected to be in the vapor phase across the dayside hemisphere for temperatures above $\sim 2000 \text{ K}$, some highly refractory molecules, such as TiO_2 and Al_2O_3 , may survive near the western limb and poles at these higher temperatures (Powell et al. 2019) before finally vaporizing completely for the most extreme cases: WASP-18b and WASP-33b. Such a scenario can be probed with higher-precision visible-light phase curves, which may reveal a westward shift in the location of maximum dayside brightness that is indicative of a cloudy western limb. Alternatively, additional sources of thermal emission due to optical absorbers such as TiO/VO , atomic iron, and dissociated hydrogen may contribute to excess flux at short wavelengths (e.g., Arcangeli et al. 2018; Lothringer et al. 2018). High-resolution dayside emission is needed to address this possibility.

4.3. Secondary Eclipse Spectrum Modeling of Kepler-13Ab

The albedo–temperature trend seen in Figure 10 is strongly driven by the two high-albedo objects with $2700 \text{ K} < T_{\text{day}} < 3000 \text{ K}$: KELT-1b and Kepler-13Ab. These orbiting companions are simultaneously among the most massive objects in the geometric albedo sample ($> 5 M_{\text{Jup}}$). When removing these objects from the sample, the significance of the albedo–temperature trend falls to 3.0σ . Understanding these apparent high-reflectivity outliers is crucial for probing the underlying physical processes that may be responsible for the putative albedo–temperature trend. The simultaneous calculation of the dayside temperatures and geometric albedos in Section 4.1 assumes that the dayside emission spectra closely resemble blackbodies. Any significant wavelength-dependent deviation in the true emission spectra would induce systematic biases in the retrieved albedo values.

Beatty et al. (2017) obtained spectroscopic secondary eclipse observations of Kepler-13Ab using HST/WFC3 and found that the resultant emission spectrum indicates a noninverted vertical temperature profile that decreases monotonically with increasing altitude. With this medium-resolution data set in hand, we

Table 6

Free Parameters and Prior Distributions Used for the Kepler-13Ab Secondary Eclipse Spectrum Retrievals

Parameter	Prior Type	Prior Values
$\log g_p$	Gaussian	3.92 ± 0.03^a
R_p/R_*	Gaussian	0.087373 ± 0.000024^b
a/R_*	Gaussian	4.5007 ± 0.004^b
A_g	Uniform	0–1
T_1	Uniform	1000–5000
b_i	Uniform	0.1–1.5
x_i	Log-uniform	10^{-12} – 10^{-2}

Notes.

^a Here g is given in cgs units. The value is based on the photometric mass estimate from Shporer et al. (2014) derived from measuring the ellipsoidal distortion amplitude.

^b From the Kepler light-curve analysis in Esteves et al. (2015).

can carry out more sophisticated modeling of the secondary eclipse spectrum and probe whether or not the high geometric albedo inferred from our blackbody fits is an artifact of our simplified approach.

To constrain the value of the geometric albedo and the atmospheric properties of Kepler-13Ab, we performed a suite of retrievals using the HELIOS-R2 model (Kitzmann et al. 2020). The model was updated to perform retrievals on emission spectra, including the option to use the corresponding filter response functions for photometric measurements and the additional contribution from reflected starlight. The compiled eclipse depths consist of the TESS and Kepler measurements from this work and Shporer et al. (2014)— 301^{+46}_{-42} and 173.7 ± 1.8 ppm, respectively—the HST/WFC3 data set (Beatty et al. 2017), and the Spitzer 3.6 and $4.5 \mu\text{m}$ secondary eclipse depths (Shporer et al. 2014). Due to its poor precision, we did not include the ground-based K -band secondary eclipse from Shporer et al. (2014).

HELIOS-R2 calculates the eclipse depth at each wavelength according to Equation (1). The thermal emission from the planet’s dayside atmosphere is generated from a free temperature–pressure (TP) profile, with scattering neglected (see Kitzmann et al. 2020 for full details). The stellar spectrum of Kepler-13A is interpolated from the PHOENIX library of theoretical stellar spectra (Husser et al. 2013) and considered fixed in the retrievals.

The free parameters and their corresponding prior distributions are listed in Table 6. The mixing ratios of the chemical species x_i were assumed to be constant throughout the atmosphere. The geometric albedo contribution to the secondary eclipse depth was only considered for the TESS and Kepler photometric points. For the TP profile, the finite element approach in HELIOS-R2 divides the atmosphere into discrete layers in log-pressure space, within which the temperature variation is modeled as a discretized polynomial of a predetermined order; continuity between adjacent layers is enforced. In our implementation, we used three second-order elements to model the planet’s TP profile; the free parameters are the base temperature of the bottom layer T_1 and the relative scaling ratios b_i that yield the temperatures of each successive grid point. The planet’s atmospheric scale height was determined by the surface gravity $\log g_p$. That parameter, along with R_p/R_* and a/R_* , was constrained by Gaussian priors based on literature measurements.

Table 7

Comparison of Kepler-13Ab Secondary Eclipse Spectrum Retrievals

Model	$\ln Z^a$	B_1^a	A_g
H ₂ O, K (+Na opacity)	-123.47 ± 0.05	...	$0.26^{+0.05}_{-0.06}$
H ₂ O, K, TiO	-124.39 ± 0.05	2.51	$0.34^{+0.06}_{-0.08}$
H ₂ O, K, Na	-124.40 ± 0.05	2.53	$0.20^{+0.07}_{-0.08}$
H ₂ O, K	-124.70 ± 0.05	3.42	$0.05^{+0.04}_{-0.03}$
H ₂ O	-132.56 ± 0.06	8870	$0.01^{+0.02}_{-0.01}$

Note.

^a $\ln Z$: logarithm of the Bayesian evidence; B_1 : Bayes factor relative to the best-performing model.

We first ran a free chemistry retrieval that fit for the abundances of a large number of atmospheric species, including H₂O, CO, Fe, FeH, Ti, TiO, VO, Na, K, Ca, and SH. In this and all subsequent retrievals, the remainder of the atmosphere was composed of H₂ and He, assuming the solar ratio for their relative elemental abundances and accounting for collision-induced absorption. From this superset, we identified those species that had significant detections by comparing the Bayesian evidence of the full retrieval and those with one or several species removed. We arrived at a small subset of species—H₂O, K, Na, and TiO—that we considered for subsequent retrievals, with no additional opacity sources.

In addition to retrievals where the abundances of the four aforementioned species were allowed to vary freely, we also ran models in which some species varied jointly with others, with the relative abundances fixed to the solar values (indicated in the table with the “+opacity” designation). This was done, for example, with Na, where the sodium abundance was scaled to the fitted potassium abundance in each iteration of the model. Such retrieval runs reduced the number of free parameters while still accounting for the contributions of both species to the overall atmospheric opacity.

Table 7 presents the Bayesian evidence and inferred geometric albedos for a range of retrievals. Figure 11 shows the median emission spectrum models for three representative retrievals alongside the measured TP profile from the best-performing retrieval, i.e., the run that includes H₂O, K, and opacity from Na assuming a solar Na/K abundance ratio. The two-dimensional posteriors and TP profiles are provided in Appendix C for the same three retrievals. All of the models yield a noninverted TP profile, which is necessary to match the shape of the H₂O absorption feature in the HST/WFC3 emission spectrum (see discussion in Beatty et al. 2017).

However, we find that the model with only H₂O opacity is significantly outperformed by models that include potassium, which has a broad absorption feature between 0.7 and $0.9 \mu\text{m}$, as well as a series of narrow absorptions between 1.1 and $1.3 \mu\text{m}$. The latter features in particular provide a superior fit to the four to five data points at the short-wavelength end of the HST/WFC3 spectrum. Including additional species that absorb strongly in the optical (Na, TiO) led to further slight improvements in the Bayesian evidence. As illustrated in Figure 11, these species alter the detailed shape of the emission spectrum shortward of $\sim 1 \mu\text{m}$, where only broadband photometric measurements are available; therefore, we are unable to discern any spectroscopic features, and the addition of Na or TiO primarily serves to adjust the planetary flux ratio between the Kepler and TESS bandpasses. Formally, the best-performing

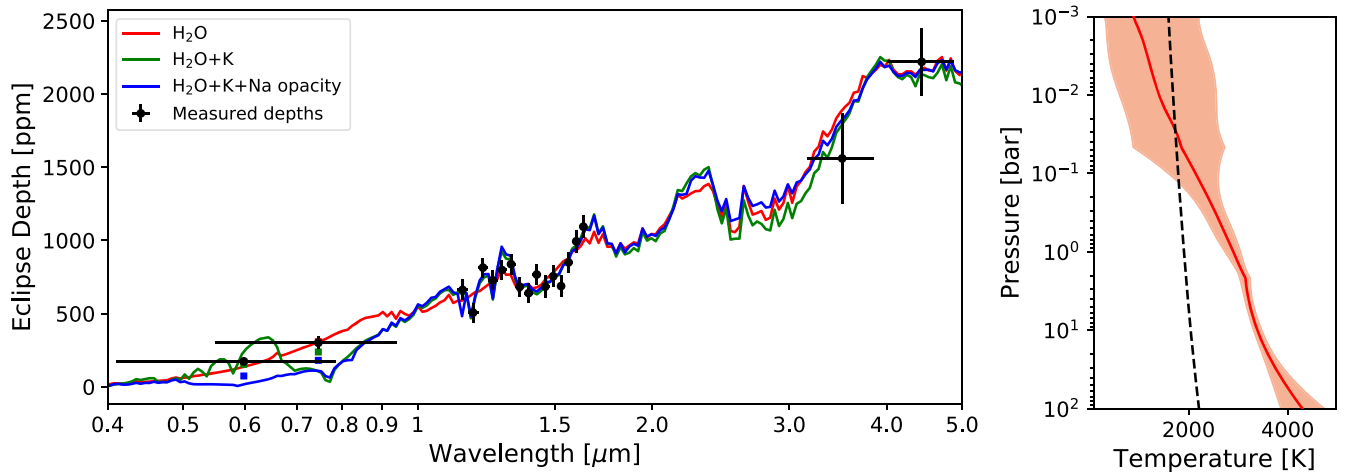


Figure 11. The left panel shows the median retrieved emission spectra of Kepler-13Ab from three atmospheric retrievals: (1) a model with only H₂O opacity, (2) a model containing H₂O and K, and (3) the best-performing model, which includes H₂O, K, and Na, with the abundance of Na scaled to the potassium abundance assuming a solar Na/K ratio. The retrieved reflected-light component is not plotted. The colored squares at optical wavelengths indicate the band-integrated model fluxes for the Kepler and TESS bandpasses. The black data points are the measured eclipse depths. Right panel: the TP profile from the H₂O+K+Na opacity retrieval. The shaded region indicates the 1 σ confidence interval. The black dashed line shows the condensation curve of TiO.

retrieval is the model that includes freely varying H₂O and K abundance, with Na abundance scaled to the corresponding solar Na/K ratio.

Looking at the corresponding geometric albedo posteriors, we find a stark difference between models that include optical absorbers and those that do not. For the retrievals that include only H₂O and K, the modeled emission level at optical wavelengths is significantly higher than the corresponding best-fit blackbody ($T_{\text{day}} = 2786 \pm 160$ K; Table 5), resulting in very low geometric albedos near zero. This is consistent with the findings in Beatty et al. (2017), where the forward models did not include any optical absorbers. Meanwhile, the addition of Na or TiO lowers the planetary emission in the TESS and Kepler bandpasses, thereby necessitating a nonnegligible reflected-light component in the overall dayside flux; the resulting best-fit albedo values range from 0.20 to 0.34. In short, the question of whether Kepler-13Ab has enhanced dayside reflectivity hinges upon the presence of optical absorbers.

The lack of a thermal inversion, combined with the relatively cool upper atmosphere, disfavors the presence of vapor-phase TiO on the dayside. In the right panel of Figure 11, we show the TiO condensation curve. At pressures lower than ~ 10 –100 mbars, the atmosphere may not be hot enough to support vapor-phase TiO. Furthermore, as discussed in depth by Beatty et al. (2017), the high surface gravity of Kepler-13Ab makes gravitational settling of condensed species very efficient, which may facilitate a cold-trap process wherein TiO condenses out on the cooler nightside and becomes locked deep in the atmosphere (Parmentier et al. 2016).

Meanwhile, there is no clear mechanism for cold-trapping sodium. The most prominent condensate species containing sodium is Na₂S, which condenses at 700–1200 K for pressures between 1 μ bar and 100 bars (e.g., Visscher et al. 2006). These temperatures are much lower than those found across both the dayside and nightside ($T_{\text{night}} = 2537 \pm 45$ K; Shporer et al. 2014) of Kepler-13Ab. Therefore, vapor-phase sodium is expected to be present on the dayside of the planet and contribute significantly to the opacity at short wavelengths.

To summarize, we find that the measured secondary eclipse spectrum of Kepler-13Ab shows strong evidence for H₂O and K absorption, with Na opacity at optical wavelengths requiring

significant reflected light across the dayside hemisphere. The retrieved geometric albedo from the H₂O+K+Na opacity model ($0.26^{+0.05}_{-0.06}$) is broadly consistent with the TESS-derived geometric albedo (0.53 ± 0.15). Likewise, the modeled value is in good agreement with the Kepler-band geometric albedo we derived from the joint blackbody+reflectivity fit of the Spitzer 3.6 and 4.5 μ m and Kepler-band secondary eclipse depths ($0.35^{+0.04}_{-0.05}$; Section 4.1). These results show that the high dayside reflectivity derived from our previous simplistic approach is also inferred from more detailed atmospheric modeling of Kepler-13Ab, lending strong support to the temperature–albedo trend in Figure 10. Future spectroscopic observations of KELT-1b, the other high-reflectivity object in our albedo sample, will allow for similar intensive atmospheric characterization and test the accuracy of its high inferred TESS-band geometric albedo (0.45 ± 0.16).

4.4. Interpretation of Geometric Albedos and Phase Integrals

Formally, the geometric albedo is evaluated at zero phase angle (superior conjunction), either at a specific wavelength or, in the case of broadband photometry, integrated over a finite range of wavelengths (e.g., the TESS bandpass). The spherical albedo is the geometric albedo evaluated over all orbital phase angles (Russell 1916; Sobolev 1975; Seager 2010). The Bond albedo A_B (Bond 1861) is the spherical albedo integrated over all wavelengths, weighted by the spectrum of the star (e.g., Marley et al. 1999). The phase integral q is formally defined as the ratio between the spherical and geometric albedos (Russell 1916; Sobolev 1975; Seager 2010), but in practice, it is often defined as (e.g., Pearl et al. 1990; Pearl & Conrath 1991)

$$q = \frac{A_B}{A_g}. \quad (15)$$

There is a rich history of measuring the geometric albedo, Bond albedo, and phase integral for the planets and moons of our solar system (Bond 1861; Russell 1916; Horak 1950; Hapke 1963; de Vaucouleurs 1964; Hanel et al. 1981, 1983; Pearl et al. 1990; Pearl & Conrath 1991). It is worth noting that the A_g , A_B , and q of Jupiter were substantially revised between the Voyager

Table 8
Thermal Energy Budget and Reflectivity Properties

Planet	T_{irrad} (K)	T_{day} (K) ^a	T_{night} (K) ^a	ϵ	A_B	A_g ^b	q
CoRoT-2b	2173 ± 47	1756 ⁺⁴⁴ ₋₄₃	873 ⁺⁵¹ ₋₄₁	0.15 ± 0.03	0.29 ^{+0.08} _{-0.10}	0.07 ± 0.03	4.1 ± 2.2
HAT-P-7b	3058 ± 76	2930 ± 100	2520 ⁺²⁴⁰ ₋₂₉₀	0.75 ^{+0.15} _{-0.19}	-1.41 ^{+0.51} _{-0.57}	<0.28	...
KELT-1b	3439 ± 73	3240 ± 140	1350 ⁺²³⁰ ₋₂₆₀	0.11 ^{+0.08} _{-0.05}	<0.21	0.45 ± 0.16	<0.5
Qatar-1b	1920 ± 52	1535 ± 61	900 ± 180	0.33 ^{+0.21} _{-0.17}	0.20 ^{+0.15} _{-0.20}	0.14 ± 0.11	1.4 ± 1.7
WASP-12b ^c	3600 ± 94	2935 ± 85	1330 ± 180	0.12 ^{+0.07} _{-0.05}	0.26 ^{+0.11} _{-0.12}	0.13 ± 0.06	2.0 ± 1.3
WASP-18b	3423 ± 30	3151 ⁺⁵⁹ ₋₅₈	960 ⁺¹⁴⁰ ₋₁₇₀	0.03 ^{+0.02} _{-0.01}	<0.08	<0.03	...
WASP-19b	2942 ± 48	2291 ⁺⁶⁷ ₋₆₆	1380 ⁺¹²⁰ ₋₁₄₀	0.30 ^{+0.11} _{-0.09}	0.31 ^{+0.09} _{-0.10}	0.17 ± 0.07	1.8 ± 0.9
WASP-33b	3916 ± 53	3232 ± 49	1559 ± 39	0.13 ± 0.02	0.24 ± 0.06	<0.08	>3.0
WASP-43b	2022 ± 93	1476 ⁺⁴⁷ ₋₄₆	640 ⁺¹⁰⁰ ₋₁₁₀	0.11 ^{+0.08} _{-0.05}	0.52 ^{+0.10} _{-0.13}	0.13 ± 0.06	4.0 ± 2.0

Notes.

^a Dayside and nightside brightness temperatures measured from analyses of Spitzer 4.5 μm phase curves (Bell et al. 2021).

^b Geometric albedos derived from the TESS- or CoRoT-band secondary eclipse depths.

^c Weighted averages from the two full-orbit phase-curve observations in 2010 and 2013.

(Hanel et al. 1981) and Cassini (Li et al. 2018) data sets. Meanwhile, Cassini data of Saturn, Neptune, and Uranus have not been analyzed to produce estimates for A_g , A_B , and q (L. Li 2021, private communication).

The Bond albedo of an exoplanet can be straightforwardly estimated from its thermal phase curve. The dayside and nightside brightness temperatures depend on both the Bond albedo A_B and the efficiency of heat transport from the dayside to the nightside ϵ (e.g., Cowan & Agol 2011):

$$T_{B,p,\text{day}} = T_* \sqrt{\frac{R_*}{a}} (1 - A_B)^{1/4} \left(\frac{2}{3} - \frac{5}{12} \epsilon \right)^{1/4}, \quad (16)$$

$$T_{B,p,\text{night}} = T_* \sqrt{\frac{R_*}{a}} (1 - A_B)^{1/4} \left(\frac{\epsilon}{4} \right)^{1/4}. \quad (17)$$

Here ϵ ranges from zero to 1, corresponding to the extremes of no day–night heat recirculation and full recirculation (i.e., uniform temperature across the planet), respectively.

To calculate the Bond albedos, we utilized dayside and nightside blackbody brightness temperatures derived from a recent uniform reanalysis of Spitzer 4.5 μm full-orbit phase curves published in Bell et al. (2021). For targets with both TESS and Spitzer secondary eclipse results, we carried out joint MCMC fits of the measured dayside and nightside temperatures using Equations (16) and (17) while applying Gaussian priors to T_* and a/R_* based on values from the corresponding discovery papers and Table 1. The resulting A_B and ϵ values are listed in Table 8, along with the published dayside and nightside brightness temperatures from the Spitzer 4.5 μm phase-curve analysis and the irradiation temperature, which is defined as $T_{\text{irrad}} \equiv T_* \sqrt{R_*/a}$. In the case of KELT-1b and WASP-18b, 2σ upper limits on A_B are provided. The inferred negative Bond albedo of HAT-P-7b is a notable outlier, along with its very high nightside brightness temperature (see also discussion in Wong et al. 2016). We note that the simple thermal balance arguments underpinning Equations (16) and (17) break down and can lead to biases in the inferred quantities when there are strong discrepancies in the TP profiles and/or compositional gradients between the dayside and nightside hemispheres. Future spectroscopically resolved full-orbit thermal phase curves will help disentangle the various physical and chemical processes that affect the thermal energy budget on exoplanets.

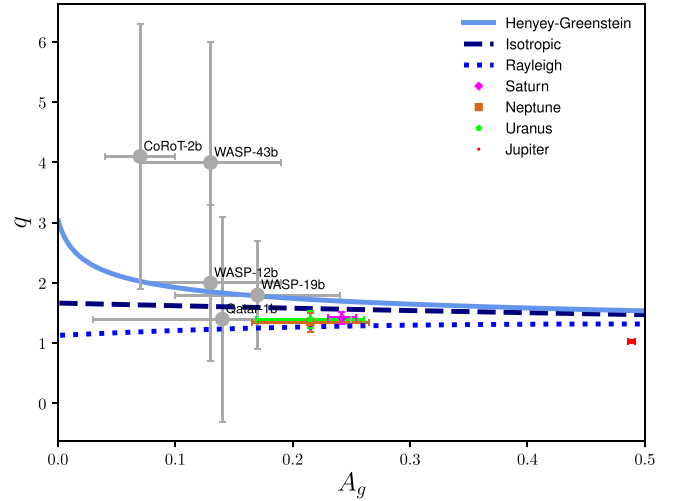


Figure 12. Plot of phase integral versus geometric albedo for five objects in our sample. Also shown are entries for the gas and ice giants of the solar system. The model curves corresponding to the Rayleigh, isotropic, and Henyey–Greenstein reflection laws were calculated using the theory of Heng et al. (2021) for homogeneous atmospheres, which relates A_g and q for any reflection law. For comparison with Jupiter, we show the curve corresponding to the Henyey–Greenstein reflection law with a scattering asymmetry factor of $g_0 = 0.4$. The uncertainties on q for the planets in our TESS sample are too large to robustly exclude any reflection law.

Combining the geometric albedos measured from TESS data in the current study and the derived Bond albedos, we estimated the values of the phase integral (Table 8). Figure 12 plots q versus A_g for the five objects in our sample with measured values of both quantities. Heng et al. (2021) described an ab initio theory for single and multiple scattering of radiation in a semi-infinite, homogeneous atmosphere that relates A_g , A_B , and q in terms of fundamental physical parameters: the single-scattering albedo ω_0 and the scattering asymmetry factor g_0 . The theory was developed for any law of reflection that depends only on the scattering angle. For Rayleigh and isotropic scattering, ω_0 is the only free parameter needed to calculate A_g , A_B , and q . For the commonly used Henyey–Greenstein reflection law (Henyey & Greenstein 1941), which describes anisotropic scattering, $-1 \leq g_0 \leq 1$ quantifies the degree of asymmetry; $g_0 = 0$ corresponds to the limit of isotropic scattering. Isotropic and Rayleigh scattering correspond to the regime of small-particle

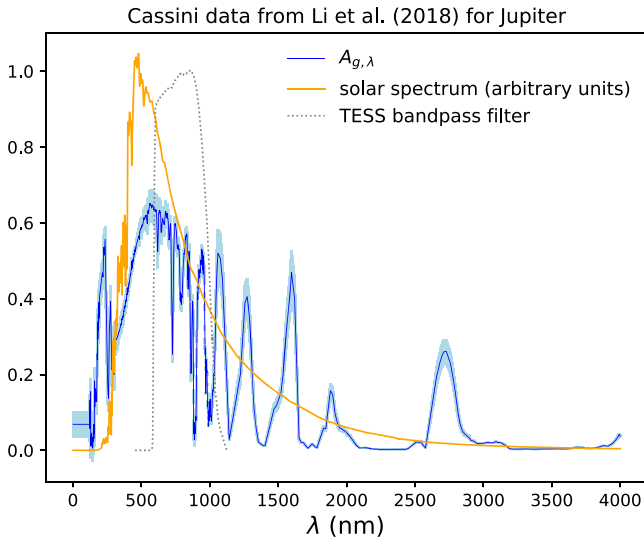


Figure 13. The blue curve and shaded region denote the wavelength-dependent geometric albedo $A_{g,\lambda}$ and corresponding uncertainties derived from the Cassini data analysis of Jupiter, previously published as Figure 3 in Li et al. (2018). The orange curve is the solar spectral irradiance taken from Supplementary Figure 1 of Li et al. (2018). Overlaid in gray is the TESS bandpass filter. These three curves were used to estimate the geometric albedo of Jupiter integrated over the TESS bandpass: $A_g = 0.489 \pm 0.003$.

scattering, where “small” has a well-defined meaning, $2\pi r/\lambda \ll 1$, where r is the radius of the (spherical) particle and λ is the wavelength (Mie 1908; Pierrehumbert 2010; Kitzmann & Heng 2018).

The values for Saturn (Hanel et al. 1983), Neptune (Pearl & Conrath 1991), and Uranus (Pearl et al. 1990) in Figure 12 were taken from Table 7 of Pearl & Conrath (1991), which also lists Jupiter as having $A_g = 0.274 \pm 0.013$, $A_B = 0.343 \pm 0.032$, and $q = 1.25 \pm 0.1$ (Hanel et al. 1981). However, the more recent study of Li et al. (2018) used Cassini data to calculate $A_B = 0.503 \pm 0.012$. Figure 13 shows the geometric albedo $A_{g,\lambda}$ as a function of wavelength (taken from Figure 3 of Li et al. 2018). To estimate A_g in the TESS bandpass, we weighted $A_{g,\lambda}$ with the TESS transmission function and the solar spectral irradiance (i.e., the solar spectrum) from Supplementary Figure 1 of Li et al. (2018) and integrated over the TESS bandpass. This yielded $A_g = 0.489 \pm 0.003$. The uncertainty on A_g was estimated by randomly sampling the Gaussian-distributed $A_{g,\lambda}$, where the uncertainties are provided by Figure 3 of Li et al. (2018). Using $A_B = 0.503 \pm 0.012$, the phase integral is $q = 1.03 \pm 0.03$, where we have assumed that the uncertainties on A_g and A_B are uncorrelated. We checked that weighting $A_{g,\lambda}$ by a 5780 K blackbody spectrum instead of the solar spectral irradiance from Li et al. (2018) produces almost identical values for A_g and q .

Figure 12 illustrates how the current uncertainties on A_g and q are large enough that the atmospheres of Qatar-1b, WASP-12b, and WASP-19b are consistent with the Rayleigh, isotropic, and Henyey–Greenstein ($g_0 = 0.4$) reflection laws. For CoRoT-2b and WASP-43b, the isotropic and Rayleigh reflection laws are weakly disfavored, but nonetheless, the measured phase-integral values lie within 1.5σ of all three theoretical curves. In other words, the current constraints on q for hot Jupiter atmospheres are uninformative. The phase integral of Jupiter is inconsistent with Rayleigh scattering in the TESS bandpass, but robust conclusions cannot be drawn about the size of the scattering particles from analyzing q and A_g

alone. Detailed analysis of the Cassini Jupiter phase curves using a double Henyey–Greenstein reflection law indicates the presence of large ($g_0 \approx 0.4$ for $0.4\text{--}1\ \mu\text{m}$), possibly irregular, polydisperse aerosols in the Jovian atmosphere (Heng & Li 2021). The chemistry of the clouds and hazes in the atmosphere of Jupiter remains an active area of debate and investigation (e.g., Stromovsky & Fry 2002; Baines et al. 2019; Braude et al. 2020; Dahl et al. 2021).

The medians of the phase-integral posteriors for CoRoT-2b and WASP-43b lie around $q = 4$. For homogeneous cloud cover, it is difficult to produce $q \sim 4\text{--}5$, unless $\omega_0 \sim 0$ and $g_0 \sim 1$ (see Figure 14). Using the theory developed by Heng et al. (2021), we experimented with inhomogeneous cloud cover for reflective, semi-infinite atmospheres obeying the Henyey–Greenstein reflection law. This consideration was motivated by the unusual westward phase offset in the Kepler-7b phase curve (Demory et al. 2013; Hu et al. 2015; Shporer & Hu 2015), as well as the general circulation models of Oreshenko et al. (2016) and Roman & Rauscher (2017). We assumed that the atmosphere is dark (with a single-scattering albedo of $\omega_0 = 0.01$) between the local latitudes of x_1 and $x_2 = 90^\circ$, where x_1 was allowed to vary between -80° and 80° . Outside of the region bounded by x_1 and x_2 , the atmosphere is bright and perfectly reflective, with a single-scattering albedo of unity. Figure 14 shows that such inhomogeneous atmospheres readily produce $q \sim 4\text{--}5$ and even $q \sim 10$. The higher values of q are due to a phase shift in the reflected-light phase curve of a planet with inhomogeneous cloud cover, which results in a diminished value of A_g while maintaining a high A_B value. The main prediction from these calculations is that high- q dayside atmospheres are likely to have patchy, inhomogeneous clouds concentrated near the limb, which should produce a significant shift in the reflected-light component of the visible-wavelength phase curve, as in the case of Kepler-7b.

4.5. Updated Transit Ephemerides

The new transit-timing measurements we obtained from the TESS light-curve fits provide additional time baselines to the body of published timings. To fit for updated transit ephemerides and probe for orbital period drift, we gathered the timing measurements available in the peer-reviewed literature, following selection criteria analogous to those outlined in Paper I. We included all timings that (i) have a well-specified time standard, from which we converted to BJD_{TDB} when necessary; (ii) were derived from transit light curves that contain at least half of both ingress and egress; (iii) were fit without any applied priors on the mid-transit time; and (iv) were not affected by starspots, significant time-correlated noise, or other clearly discernible systematic features in the residuals. Many of our targets have benefited from extensive follow-up transit monitoring, and for the sake of maximizing uniformity, we relied on published global reanalyses of previous transit light curves whenever possible. The detailed light-curve vetting carried out in many of these more recent works was also used in our timing measurement selection process. Appendix D provides an exhaustive list of all transit timings included in our analysis.

For each system, we fit the transit timings to both a linear and a quadratic transit ephemeris model,

$$T_{\text{in}}(E) = T_0 + PE, \quad (18)$$

$$T_{\text{quad}}(E) = T_0 + PE + \frac{P}{2} \frac{dP}{dt} E^2, \quad (19)$$

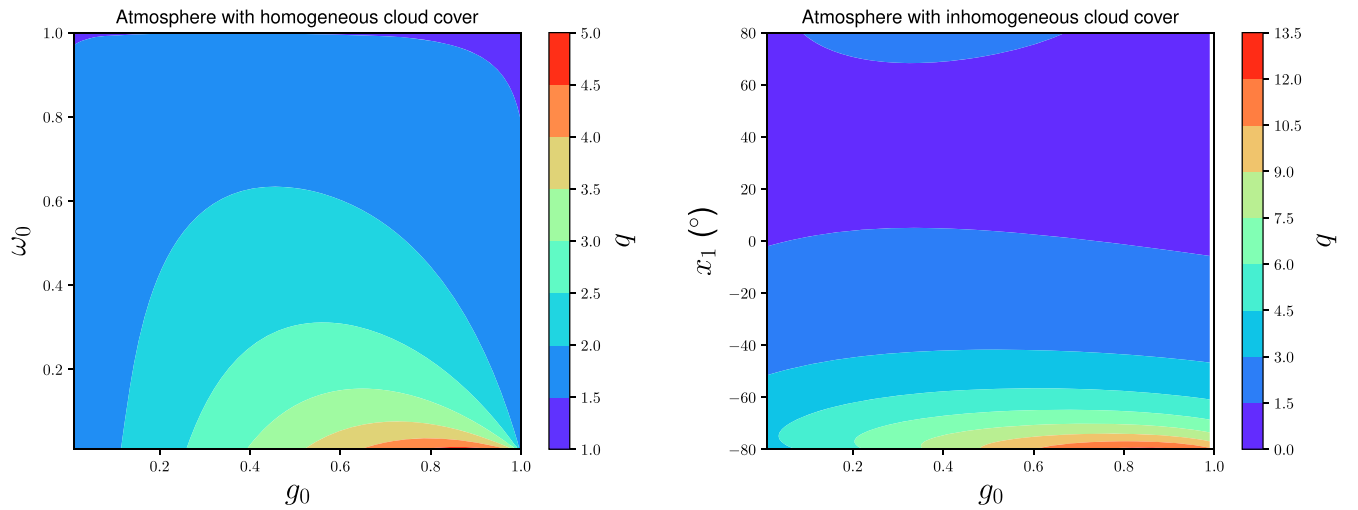


Figure 14. Plots of phase-integral values q computed for purely reflective, semi-infinite atmospheres with homogeneous (left panel) and inhomogeneous (right panel) cloud cover, assuming the Henyey–Greenstein reflection law (Heng et al. 2021). For inhomogeneous cloud cover, the atmosphere is assumed to be dark (with single-scattering albedo $\omega_0 = 0.01$) between the local latitudes of x_1 and $x_2 = 90^\circ$; outside of these local latitudes, the single-scattering albedo is unity. Atmospheres with high phase-integral values ($q > 5$) require inhomogeneous cloud cover concentrated near the limb of the dayside hemisphere.

Table 9
Updated Transit Ephemerides

System	N^a	Δt^a (days)	T_0 (BJD _{TDB} - 2,450,000)	P (days)	dP/dt^b (ms yr ⁻¹)
HAT-P-7	12	4021	5,430.58175 ± 0.00038	2.20473639 ± 0.00000047	<110
HAT-P-36	24	3356	6,766.43049 ± 0.00013	1.32734686 ± 0.00000024	<20
KELT-1	15	2879	7,306.97607 ± 0.00018	1.21749412 ± 0.00000023	<36
KELT-16	52	1885	8,056.357231 ± 0.000078	0.96899322 ± 0.00000021	<40
KELT-20	11	1397	8,312.58576 ± 0.00019	3.4740985 ± 0.0000016	<600
KELT-23A ^c	8,769.612278 ± 0.000060	2.25528773 ± 0.00000077	...
Qatar-1	81	3319	6,458.466991 ± 0.000042	1.420024305 ± 0.000000076	<8.6
TrES-3	99	4822	5,591.367536 ± 0.000057	1.306186358 ± 0.000000060	<5.9
WASP-3	66	4879	5,362.762292 ± 0.000093	1.84683510 ± 0.00000020	<14
WASP-12	132	4338	6,722.378206 ± 0.000038	1.091419740 ± 0.000000029	-29.1 ± 2.0
WASP-92	2	2590	6,381.28419 ± 0.00028	2.17467334 ± 0.00000054	...
WASP-93	2	2700	6,079.56495 ± 0.00046	2.73253748 ± 0.00000078	...
WASP-135	9	3791	8,249.55918 ± 0.00050	1.4013776 ± 0.0000016	<150

Notes.

^a N : number of published transit-timing measurements included in fit; Δt : time baseline spanned by the timing measurements.

^b Period derivative. In the case of nondetections, the 2σ upper limit on the absolute value is given.

^c For KELT-23A, we list the updated ephemeris derived from our analysis of the long-baseline multisector full-orbit TESS light curve (Table 4), which is significantly more precise than the ephemeris derived from an analogous global timing analysis using the measured mid-transit time and previous literature values.

where E , T_0 , P , and dP/dt are the transit epoch, zeroth epoch mid-transit time, orbital period, and period derivative, respectively. The zeroth epoch was set to the published transit epoch closest to the weighted average of all available transit timings.

The literature transit timings were combined with the measurements we obtained from our TESS light-curve fits using the residual permutation analysis, $T_{0,\text{PB}}$. As with our light-curve fitting, we included a uniform per-point scatter scaling to ensure $\chi_r^2 = 1$ for cases in which the noninflated uncertainties produced $\chi_r^2 > 1$. The full list of updated transit ephemerides is given in Table 9. For the systems where no significant period variation was detected, we provide 2σ upper limits on $|dP/dT|$. The observed minus calculated ($O - C$) timing residual plots for all systems with more than two published epochs are shown in Appendix E.

TESS observed KELT-23A for six sectors, and the transit ephemeris we derived from our light-curve fit significantly supersedes the result from the corresponding multiepoch transit-timing fit. As such, we simply list the TESS ephemeris for that system in the table. We also excluded Kepler-13A, which was observed throughout the second year of the TESS mission during sectors 14, 15, and 26 (Section 3.5). The only previous source of transit timings for this system is the 4 yr Kepler light curve. A dedicated analysis of all individual Kepler and TESS transits (up through sector 15) was carried out in Szabó et al. (2020), resulting in an exquisite updated transit ephemeris: $T_0 = 2,455,101.708005 \pm 0.000013$ BJD_{TDB}, $P = 1.76358762 \pm 0.00000003$ days. The best-fit transit ephemeris from our full TESS light-curve analysis (Table 1) agrees with those values.

Mancini et al. (2021) presented an independent transit ephemeris analysis of the KELT-16 system, including the

TESS transits, and obtained $P = 0.96899340 \pm 0.00000018$ day, which agrees with our value at the 0.7σ level. Our set of fitted transit timings is a subset of the timings utilized in their work, due to our more stringent selection criteria.

The only system that displays significant period variation is WASP-12. This period drift has been confirmed by several previous transit-timing analyses (Patra et al. 2017; Yee et al. 2020), with the latter work strongly supporting the scenario of orbital decay over apsidal precession. Recently, Turner et al. (2021) presented a dedicated analysis of transit and secondary eclipse light curves from TESS, reinforcing the conclusion that the orbit of WASP-12b is decaying and not precessing. The decay rate we calculated in this paper— $dP/dt = -29.1 \pm 2.0$ ms yr⁻¹—is statistically identical to the value published in Yee et al. (2020): -29.0 ± 2.0 ms yr⁻¹. Meanwhile, Turner et al. (2021) obtained a slightly higher decay rate of -32.5 ± 1.6 ms yr⁻¹, which is still consistent with our value at the 1.3σ level.

Among the other targets, Qatar-1 and TrES-3 have the most precise updated ephemerides, with 2σ upper limits on period variations of less than 10 ms yr⁻¹. The added time baseline that TESS will provide when it reobserves all of these systems in the extended mission will drastically tighten the current upper limits on orbital decay. Future transit-timing measurements of WASP-12 will yield even more exquisite precision on the decay rate and produce unprecedented constraints on the host star’s tidal quality factor, with important implications for the study of star–planet interactions in this unique system.

5. Conclusions

In this paper, we presented the results from our systematic phase-curve study of previously discovered transiting systems observed during the second year of the TESS primary mission, consisting of TESS sectors 14–26 from 2019 July 18 to 2020 July 4. We carried out a uniform data processing and light-curve fitting analysis on 15 systems that satisfied our target-selection criteria. The primary findings of our study are summarized below.

1. Seven systems show statistically significant secondary eclipses: HAT-P-7b (127^{+33}_{-32} ppm), KELT-1b (388^{+67}_{-65} ppm), KELT-9b (630^{+18}_{-17} ppm), KELT-16b (410^{+130}_{-120} ppm), KELT-20b (111^{+35}_{-36} ppm), Kepler-13Ab (301^{+46}_{-42} ppm), and WASP-12b (443^{+86}_{-85} ppm). The full results from our light-curve fits are provided in Table 1.
2. All seven systems also display atmospheric brightness modulation, with measured semiamplitudes of 56^{+14}_{-13} , 176^{+26}_{-30} , $271.9^{+9.0}_{-8.9}$, 175^{+64}_{-62} , 43^{+13}_{-11} , 151^{+15}_{-16} , and 264^{+33}_{-30} ppm, respectively. For two systems—KELT-9b and WASP-12b—we detected significant eastward offsets in the location of the dayside brightness maximum, with magnitudes of $2^{\circ}6^{+1.3}_{-1.3}$ and $13^{\circ}2 \pm 5^{\circ}7$, respectively.
3. We measured significant ellipsoidal distortion modulation on KELT-1, Kepler-13A, and WASP-12. The amplitudes of these signals are in good agreement with the predicted values from theoretical models. For KELT-9, we repeated the analysis from Wong et al. (2020d) with the updated photometry from the TESS SPOC pipeline and recovered the additional time-varying irradiation signal caused by the planet’s near-polar orbit, which has a semiamplitude of $60.1^{+9.4}_{-9.1}$ ppm (Table 2).

4. For the remaining eight systems—HAT-P-36, KELT-23A, Qatar-1, TrES-3, WASP-3, WASP-92, WASP-93, and WASP-135—no significant phase-curve signals were detected. The results of our transit light-curve fits of these systems are provided in Table 4, with upper limits and marginal secondary eclipse depths listed in Table 3.
5. We self-consistently computed dayside blackbody brightness temperatures and TESS-band geometric albedos for objects in our sample with published Spitzer 3.6 and $4.5 \mu\text{m}$ secondary eclipse depths (Table 5). KELT-1b and Kepler-13Ab show enhanced albedos (0.45 ± 0.16 and 0.53 ± 0.15). These high-reflectivity endmembers strengthen the statistical significance of the previously reported trend between increasing dayside temperature and increasing TESS-band geometric albedo for objects with $1500 \text{ K} < T_{\text{day}} < 3000 \text{ K}$.
6. For Kepler-13Ab, we sought to confirm the high inferred albedo by leveraging the HST/WFC3 spectrophotometric data set obtained by Beatty et al. (2017) and carrying out a detailed atmospheric retrieval analysis of the secondary eclipse spectrum. We found a decreasing TP profile and strong detections of H₂O and K absorption, as well as likely Na opacity at optical wavelengths. The presence of Na requires additional reflected light on the dayside hemisphere to match the measured TESS and Kepler secondary eclipse depths, yielding a high geometric albedo consistent with the value we obtained from the simple blackbody model.
7. Using Spitzer-derived Bond albedos and TESS-/CoRoT-derived geometric albedos, we estimated the phase integral for five objects in our combined primary mission target list and compared them to ab initio calculations of reflective atmospheres with homogeneous cloud cover. The large uncertainties on the phase integrals of CoRoT-2b, Qatar-1b, WASP-12b, WASP-19b, and WASP-43b do not allow us to rule out any reflection law. Phase integrals with values of roughly 4–5 are indicative of atmospheres with inhomogeneous cloud cover—a hypothesis that may be tested with future high-precision visible-wavelength phase curves.
8. Combining transit timings from our TESS light-curve fits and literature values, we calculated updated transit ephemerides. We obtained an orbital period decay rate of 29.1 ± 2.0 ms yr⁻¹ for WASP-12b, consistent with previous measurements.

Over the course of our 2 yr TESS phase-curve study, we measured statistically significant secondary eclipses and/or phase-curve signals for 17 known transiting systems, with a consistent analysis framework that ensures a uniform set of results. This number is comparable to the size of the Kepler phase-curve target list (Esteves et al. 2015) and firmly establishes the contribution of TESS in the realm of time-domain exoplanet science. As TESS continues its full-sky survey throughout the current extended mission and possible additional extended missions, several avenues for further study promise to expand the utility of TESS phase curves and provide additional insight into ensemble-level trends.

Improving the signal-to-noise ratio of the phase-curve measurements will be a priority for follow-up study. With new sectors of data from the current extended mission, as well as possible additional photometry from further extensions of the TESS mission through the middle of the decade, the

uncertainties on the secondary eclipse depths and atmospheric brightness modulation amplitudes will decrease significantly. For the brightest targets, the precision may rival that obtained for the Kepler phase curves, which benefited from 4 yr of near-continuous observation. These high-precision phase-folded light curves will enable exquisite resolution of the longitudinal brightness distribution and, when combined with analogous high-quality phase-curve observations at infrared wavelengths, produce detailed cloud and temperature maps.

Increased precision on the secondary eclipse depths will be especially consequential for our understanding of the trend between dayside temperature and geometric albedo. With the longer baseline from the extended mission, additional targets will populate the sample as currently marginal signals become robust detections and new near-ecliptic systems get observed in future sectors. Of particular interest is extending the TESS-band geometric albedo sample to cooler temperatures ($T_{\text{day}} < 1500$ K). Likewise, reducing the uncertainties on the dayside and nightside brightness temperatures will yield improved Bond albedo measurements and begin to unlock the explanatory potential of exoplanet phase-integral measurements for constraining atmospheric scattering laws.

The addition of more TESS data from extended missions will also enable a detailed study of variability in atmospheric properties. Such variability has been claimed by a few authors (e.g., Armstrong et al. 2016; Jackson et al. 2019; but see also Lally & Vanderburg 2020), and a low level of variability is expected from recent theoretical modeling (Komacek & Showman 2020).

Another fruitful avenue for further study is expanding the wavelength coverage of secondary eclipse spectra using spectroscopic measurements with current and near-future facilities, including HST and the James Webb Space Telescope (JWST). Our retrieval analysis of Kepler-13Ab (Section 4.3) offers a glimpse into the type of intensive atmospheric characterization that can be done when combining higher-resolution near-infrared emission spectra with optical and thermal infrared measurements. The exquisite capabilities of JWST in particular will produce detailed TP profiles and

chemical abundance constraints for a broad range of exoplanet atmospheres, allowing us to explore the interplay between atmospheric composition, heat transport, and cloud cover. By constructing a more complete picture of the dayside atmosphere, we can solidify the inferred optical geometric albedos and definitively assess the albedo–temperature trend that we have uncovered in our multiyear TESS phase-curve study.

Funding for the TESS mission is provided by NASA’s Science Mission directorate. This paper includes data collected by the TESS mission, which are publicly available from the Mikulski Archive for Space Telescopes (MAST). Resources supporting this work were provided by the NASA High-End Computing (HEC) Program through the NASA Advanced Supercomputing (NAS) Division at Ames Research Center for the production of the SPOC data products. I.W. is supported by a Heising-Simons 51 Pegasi b postdoctoral fellowship. K.H. acknowledges an honorary professorship from the University of Warwick. T.D. acknowledges support from MIT’s Kavli Institute as a Kavli postdoctoral fellow. We thank Liming Li for useful correspondence and providing data from Li et al. (2018) in electronic form. We also thank an anonymous referee for helpful comments that improved the manuscript.

Appendix A List of Light-curve Segments

Table A1 lists the light-curve segments for the 15 systems analyzed in this paper. The three-number sequence assigned to each segment in the second column denotes the TESS sector, spacecraft orbit (two per sector), and sequential data-segment number. Data segments lasting less than 1 day were excluded from our analysis and are not listed here. The third and fourth columns show the number of data points before and after removing flagged points, flux ramps, and outliers; the first and last time stamps of each data segment are also tabulated. The seventh column lists the order of the polynomial used in the detrending function (see Section 2.3). The eighth column describes any removed flux ramps, as well as segments that were excluded from the analysis due to severe systematics.

Table A1
Summary of Light-curve Segments

Target	Segment ^a	n_{raw} ^b	n_{trimmed} ^b	T_{start} ^c	T_{end} ^c	Order ^d	Comments
HAT-P-7	14-1-1	3283	3188	683.356	687.899	2	
	14-1-2	3240	3123	687.910	692.399	1	
	14-1-3	2867	2805	692.410	696.391	1	
	14-2-1	3095	2493	698.098	701.628	0	Removed 0.75 day from start
	14-2-2	3060	2992	701.639	705.878	0	
	14-2-3	3109	3044	705.889	710.206	3	
	15-1-1	3095	3004	711.367	715.649	2	
	15-1-2	3060	3001	715.660	719.899	0	
	15-1-3	1351	1155	719.910	721.585	1	
	15-2-1	3100	2978	724.943	729.232	2	
	15-2-2	3060	3004	729.243	733.482	3	
	15-2-3	1602	1428	733.493	735.517	1	
HAT-P-36	22-1-1	4187	3921	900.358	905.964	6	
	22-1-2	4700	4598	905.975	912.507	5	
	22-2-1	3758	2809	916.352	920.359	5	Removed 1.00 day from start
	22-2-2	4410	4354	920.370	926.497	7	
KELT-1	17-1-1	2820	2700	764.689	768.589	6	
	17-1-2	2790	2707	768.600	772.464	5	
	17-2-1	2923	2672	777.986	781.776	7	Removed 0.25 day from start
	17-2-2	2880	2302	782.538	785.776	6	Removed 0.75 day from start
	17-2-3	1548	1022	785.788	787.235	0	Removed 0.50 day from end
KELT-9 ^e	14-1-1	3283	2636	683.562	687.782	1	
	14-1-2	3240	1387	688.005	690.243	3	Removed 0.50 day from end
	14-1-3	2867	945	694.576	696.142	2	Removed 0.50 day from start and 0.25 day from end
	14-2-1	3095	2357	697.597	701.629	3	Removed 0.25 day from start
	14-2-2	3060	2141	701.640	705.138	6	
	14-2-3	3109	1125	708.186	709.999	3	
	15-1-1	3095	2456	711.703	715.650	4	Removed 0.25 day from start
	15-1-2	3060	2509	715.661	719.900	2	
	15-2-1	3100	2412	725.285	729.233	2	Removed 0.25 day from start
	15-2-2	3060	2508	729.246	733.483	4	
	15-2-3	2822		733.494	734.408		Large gap
KELT-16	15-1-1	3095	2837	711.369	715.651	1	Removed 0.25 day from start
	15-1-2	3060	3006	715.662	719.901	3	
	15-2-1	3100	2141	726.197	729.234	1	Removed 1.25 days from start
	15-2-2	3060	2996	729.245	733.484	2	
KELT-20	14-1-1	3283	3209	683.357	687.901	1	
	14-1-2	3240	1960	687.912	690.746	2	
	14-2-1	3095	3019	697.348	701.630	1	
	14-2-2	3060	2260	701.641	704.857	3	
KELT-23A	14-1-1	3283	3196	683.353	687.896	1	
	14-1-2	3240	3121	687.907	692.396	2	
	14-1-3	2867		692.407	696.387		Severe systematics
	14-2-1	3095	3024	697.343	701.625	1	
	14-2-2	3060	2649	702.136	705.875	2	Removed 0.50 day from start
	14-2-3	1494	1141	705.886	707.508	1	Removed 0.25 day from end
	15-1-1	3095	3020	711.364	715.646	2	
	15-1-2	3077	2164	715.657	718.727	1	Removed 1.00 day from end
	15-2-1	3100	2978	724.940	729.229	1	
	15-2-2	3060	2287	729.240	732.480	1	Removed 1.00 day from end
	16-1-1	4238	3446	739.651	744.520	2	Removed 1.00 day from start
	16-1-2	2288		744.532	747.509		Severe systematics
	16-2-1	4235	4144	751.655	757.521	4	
	16-2-2	2468		757.532	760.760		Severe systematics
	17-1-1	2820	2704	764.683	768.583	2	
	17-1-2	2790	2713	768.594	772.458	3	
	17-2-1	2923	2509	778.229	781.771	2	Removed 0.50 day from start
	17-2-2	2880	2826	781.782	785.771	5	
	21-1-1	4530	4027	870.937	876.711	3	Removed 0.50 day from start
	21-1-2	4500	4403	876.722	882.961	1	

Table A1
(Continued)

Target	Segment ^a	n_{raw} ^b	n_{trimmed} ^b	T_{start} ^c	T_{end} ^c	Order ^d	Comments
	21-2-1	4717	4161	885.511	891.461	3	Removed 0.50 day from start
	21-2-2	4543	4078	891.472	897.282	1	Removed 0.50 day from end
	23-1-1	4342	2401	931.830	936.148	4	Removed 1.50 day from start
	23-1-2	3394	3310	936.159	940.872	1	
	23-2-1	3584	2611	946.112	949.877	4	Removed 1.00 day from start
	23-2-2	3592	3535	949.888	954.876	2	
Kepler-13A	14-1-1	3283	3023	683.609	687.899	3	Removed 0.25 day from start
	14-1-2	3240	3129	687.910	692.399	0	
	14-1-3	2867	2801	692.410	696.391	3	
	14-2-1	3095	3003	697.346	701.628	2	
	14-2-2	3060	2983	701.639	705.878	1	
	14-2-3	3109	3045	705.889	710.206	2	
	15-1-1	3095	3006	711.367	715.649	0	
	15-1-2	3060	2987	715.660	719.899	1	
	15-1-3	1345	1139	719.910	721.577	1	
	15-2-1	3100	2966	724.943	729.232	0	
	15-2-2	3060	3004	729.243	733.482	0	
	15-2-3	1587	1414	733.493	735.496	0	
	26-1-1	4350	3162	1010.769	1015.296	0	Removed 0.50 day from start and 1.00 day from end
	26-1-2	4239	3095	1016.305	1020.692	1	Removed 1.50 days from end
	26-2-1	4355	3856	1023.617	1029.149	1	Removed 0.50 day from start
	26-2-2	4304	3838	1029.160	1034.635	0	Removed 0.50 day from end
Qatar-1	17-1-1	2820	2352	765.189	768.586	2	Removed 0.50 day from start
	17-1-2	2790	2708	768.597	772.461	1	
	17-1-3	1730	1196	772.472	774.172	1	Removed 0.50 day from end
	17-2-1	2923	2338	778.483	781.773	1	Removed 0.75 day from start
	17-2-2	2880	2820	781.784	785.773	2	
	17-2-3	1636	1475	785.784	787.855	1	
	21-1-1	4438	3477	871.757	876.709	0	Removed 1.00 day from start
	21-1-2	4500	4413	876.720	882.959	2	
	21-2-1	4430	4161	885.517	891.458	2	Removed 0.25 day from start
	21-2-2	4543	4461	891.470	897.779	4	
	24-1-1	9042	7753	957.294	968.346	0	Removed 1.50 day from start
	24-2-1	5622	4773	970.271	977.062	5	Removed 1.00 day from start
	24-2-2	3749	3675	977.074	982.279	0	
	25-1-1	3997	3871	983.632	989.167	3	
	25-1-2	4649	4472	989.178	995.634	2	
	25-2-1	4542	4200	997.167	1003.209	2	Removed 0.25 day from start
	25-2-2	4382	4278	1003.220	1009.305	0	
TrES-3 ^c	25-1-1	3997	3880	983.635	989.170	5	
	25-1-2	4649	4483	989.181	995.637	4	
	25-2-1	4542	4379	996.920	1003.212	4	
	25-2-2	4382	4275	1003.223	1009.308	6	
	26-1-1	4350	4226	1010.270	1016.295	4	
	26-1-2	4239	4134	1016.307	1022.193	5	
	26-2-1	4355	3160	1024.619	1029.150	2	Removed 1.50 days from start
	26-2-2	4304	4176	1029.161	1035.137	2	
WASP-3	26-1-1	4350	4046	1010.520	1016.295	4	Removed 0.25 day from start
	26-1-2	4239	3057	1017.805	1022.193	4	Removed 1.50 days from start
	26-2-1	4355	4208	1023.118	1029.150	4	
	26-2-2	4304	4179	1029.161	1035.137	4	
WASP-12	20-1-1	3910	3768	842.510	847.922	3	
	20-1-2	3870	3788	847.935	853.298	0	
	20-1-3	1119	1094	853.310	854.862	1	
	20-2-1	3029	2641	858.200	861.944	1	Removed 0.25 day from start
	20-2-2	3959	3874	861.955	867.444	1	
	20-2-3	989	952	867.455	868.827	1	
WASP-92	23-1-1	4959	3709	929.971	936.148	0	Removed 0.50 day from start
	23-1-2	3394	2981	936.160	940.372	1	Removed 0.50 day from end
	23-2-1	4214	3955	944.235	949.878	3	

Table A1
(Continued)

Target	Segment ^a	n_{raw} ^b	n_{trimmed} ^b	T_{start} ^c	T_{end} ^c	Order ^d	Comments
	23-2-2	3592	3535	949.889	954.876	1	
	24-1-1	9042	8803	955.797	968.349	0	
	24-2-1	5622	5496	969.274	977.065	0	
	24-2-2	3749	3655	977.077	982.282	0	
	25-1-1	3997	3698	983.886	989.170	0	Removed 0.25 day from start
	25-1-2	4649	4476	989.181	995.636	0	
	25-2-1	4542	3999	997.421	1003.211	0	Removed 0.50 day from start
	25-2-2	4382	4276	1003.222	1009.307	4	
WASP-93	17-1-1	2820	2518	764.938	768.589	2	Removed 0.25 day from start
	17-1-2	2790	2704	768.600	772.464	0	
	17-2-1	2923	2832	777.734	781.776	1	
	17-2-2	2880	2823	781.787	785.776	2	
	17-2-3	1226		785.787	787.289		Severe systematics
WASP-135	26-1-1	4350	4229	1010.271	1016.296	2	
	26-1-2	4239	3582	1017.056	1022.193	3	Removed 0.75 day from start
	26-2-1	4355	4227	1023.118	1029.150	2	
	26-2-2	4304	3308	1029.911	1034.636	1	Removed 0.75 day from start and 0.50 day from end

Notes.^a The numbers indicate the TESS sector, spacecraft orbit (two per sector), and segment number, respectively.^b Number of data points in each data segment before and after removing flagged points, outliers, and flux ramps.^c Start and end times of each data segment (BJD_{TDB}-2,458,000).^d Order of the polynomial systematics detrending model used in the final joint fits.^e Transits were removed from the KELT-9 light-curve segments prior to fitting. The analysis of TrES-3 used the simple aperture photometry (SAP) light curve.

(This table is available in its entirety in machine-readable form.)

Appendix B
Raw and Corrected Light Curves

Figures B1 and B2 present the light-curve plots for the 15 systems studied in this paper. The raw photometry is shown in

the top panels, with the spacecraft momentum dumps denoted by the vertical blue lines. The bottom panels display the photometry after outlier removal, ramp trimming, and systematics detrending.

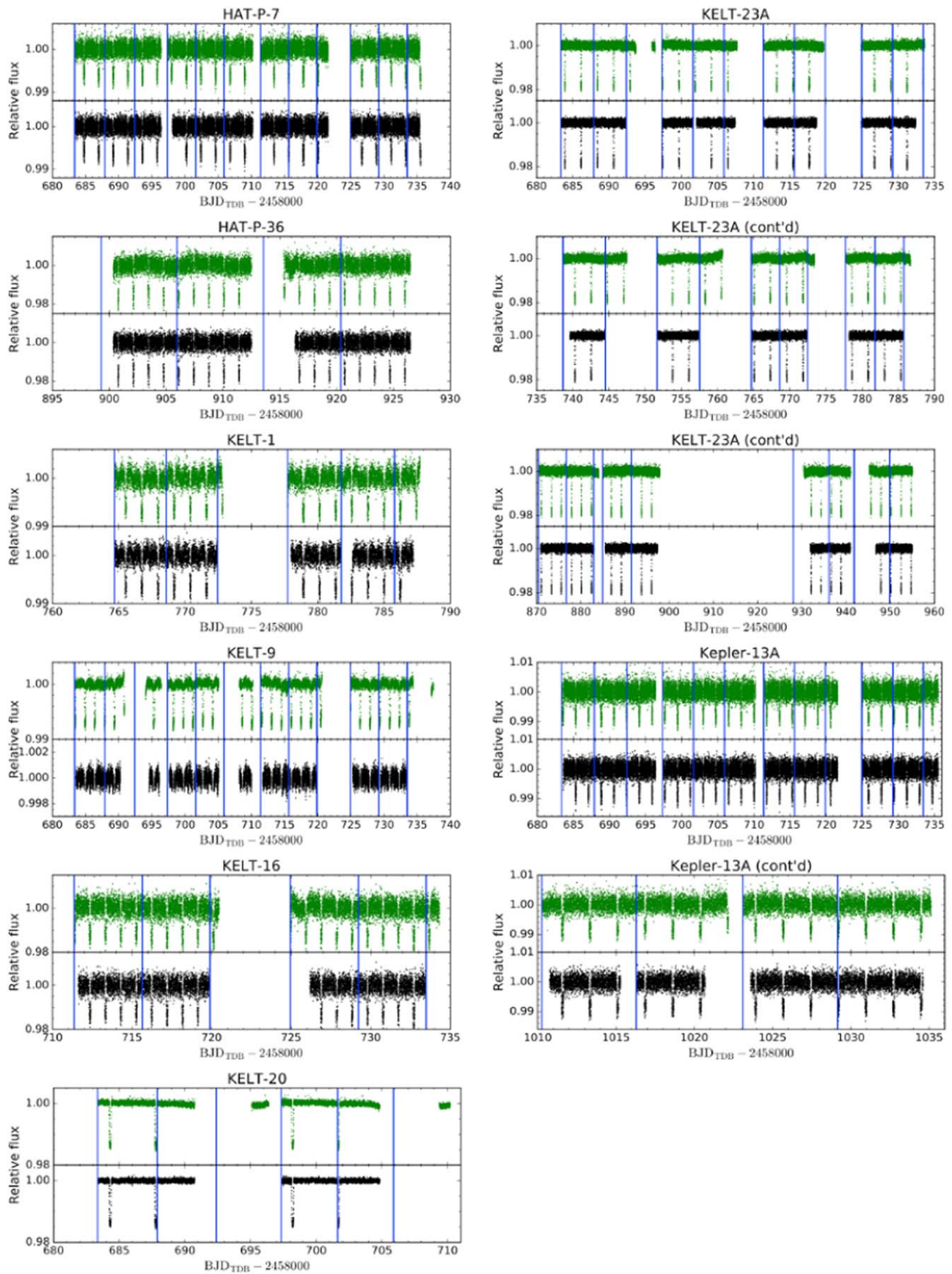


Figure B1. Light curves for eight of the 15 targets analyzed in this paper. The top and bottom panels show the photometry before and after trimming flux ramps and correcting for systematic trends. The vertical blue lines indicate the momentum dumps. For several systems, the full light curves are split across multiple plots for clarity.

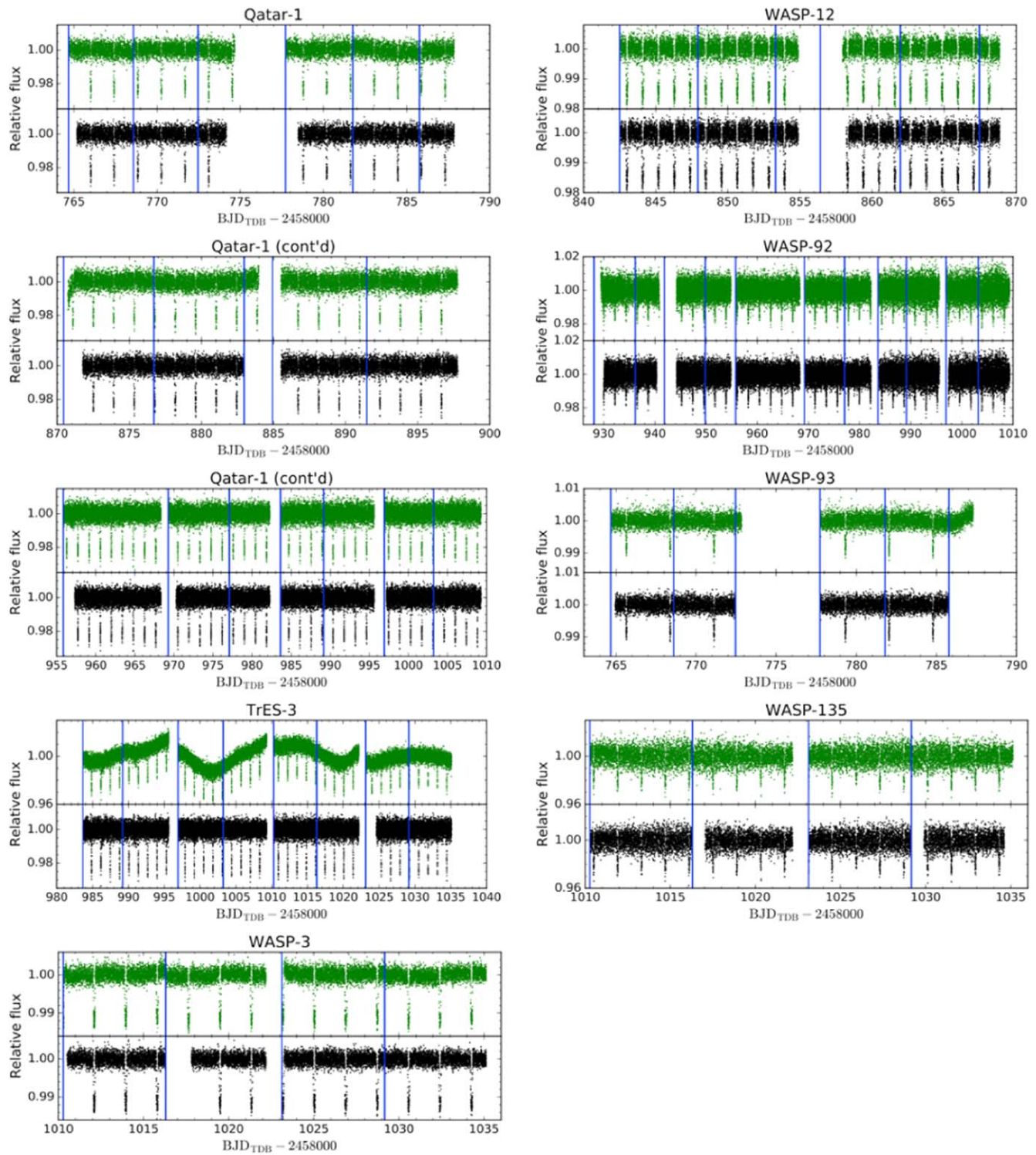


Figure B2. Continuation of Figure B1. Note the stellar variability in the TrES-3 light curve.

Appendix C Retrieval Results for Kepler-13Ab

Figure C1 shows corner plots of the two-dimensional posteriors from three atmospheric retrievals of the Kepler-

13Ab secondary eclipse spectrum: (1) the best-performing model, which includes H_2O , K, and Na, with the abundance of Na scaled to the potassium abundance assuming a solar Na/K ratio; (2) a model containing H_2O and K; and (3) a model with only H_2O opacity. The retrieved TP profiles are also provided.

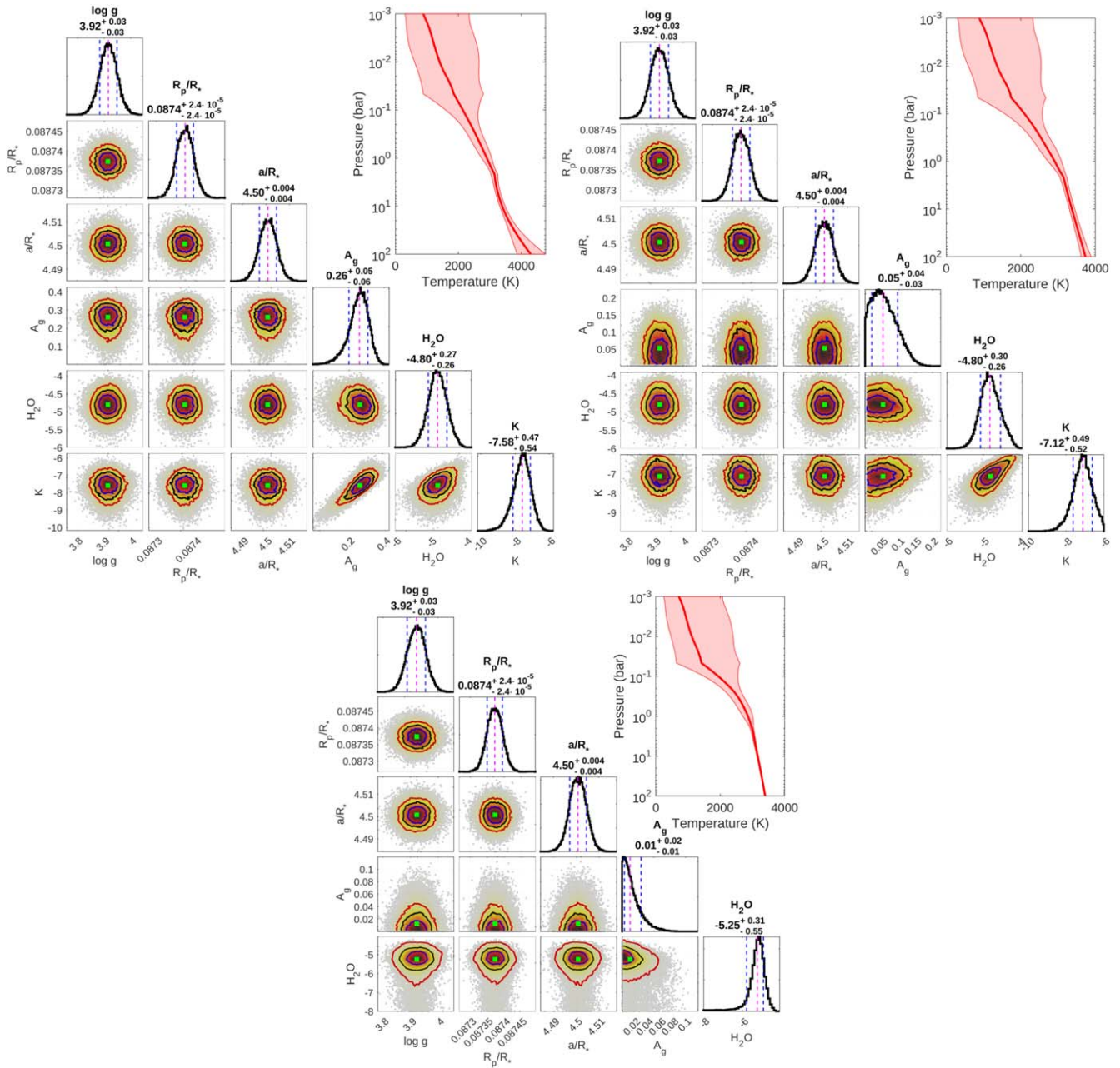


Figure C1. Posterior distributions and TP profiles from three retrieval runs on the Kepler-13Ab secondary eclipse depths using different models. Upper left panel: best-performing model, including free abundances of H₂O and K, with the Na abundance derived from the retrieved K abundance by assuming solar element abundance ratios. Upper right panel: model with free abundances of H₂O and K. Lower panel: model with free abundance of H₂O. The solid blue, red, and yellow lines in the two-parameter correlation plots mark the 1 σ , 2 σ , and 3 σ bounds, respectively. The location of the median model is marked by the green squares. In the TP profiles, the solid red line corresponds to the median profile, while the shaded region represents the 1 σ confidence interval.

Appendix D Compilation of Transit-timing Measurements

The full list of published transit timings used in our updated orbital ephemeris fits is provided in Table D1. These entries were vetted following the criteria outlined in Section 4.5. For each system, the zeroth epoch was assigned to the transit

closest to the weighted average of all timing measurements. We separately list the sources of the original transit light curves and the calculated mid-transit times utilized in our ephemeris fits. The references in these two columns differ whenever earlier transit light curves were systematically reanalyzed in subsequent works.

Table D1
List of Transit Timings

Target	T_0 (BJD _{TDB})	σ (days)	Epoch	Light-curve Source	Timing Source
HAT-P-7	2,454,687.58230	0.00120	-337	Christiansen et al. (2010)	Christiansen et al. (2010)
	2,454,696.40488	0.00075	-333	Christiansen et al. (2010)	Christiansen et al. (2010)
	2,454,698.60720	0.00120	-332	Christiansen et al. (2010)	Christiansen et al. (2010)
	2,454,700.81470	0.00110	-331	Christiansen et al. (2010)	Christiansen et al. (2010)
	2,454,703.01588	0.00099	-330	Christiansen et al. (2010)	Christiansen et al. (2010)
	2,454,705.22294	0.00086	-329	Christiansen et al. (2010)	Christiansen et al. (2010)
	2,454,707.43152	0.00074	-328	Christiansen et al. (2010)	Christiansen et al. (2010)
	2,454,709.63137	0.00092	-327	Christiansen et al. (2010)	Christiansen et al. (2010)
	2,454,731.67993	0.00041	-317	Winn et al. (2009)	Southworth (2011)
	2,455,419.55820	0.00070	-5	Wong et al. (2016)	Wong et al. (2016)
	2,455,430.58280	0.00047	0	Wong et al. (2016)	Wong et al. (2016)
	2,458,709.02466	0.00034	1487	This work	This work
	HAT-P-36	2,455,555.89060	0.00043	-912	Bakos et al. (2012)
2,455,608.98390		0.00030	-872	Bakos et al. (2012)	Mancini et al. (2015)
2,456,007.18909		0.00071	-572	Wang et al. (2019)	Wang et al. (2019)
2,456,015.15110		0.00034	-566	Wang et al. (2019)	Wang et al. (2019)
2,456,356.28178		0.00104	-309	Wang et al. (2019)	Wang et al. (2019)
2,456,372.20849		0.00078	-297	Wang et al. (2019)	Wang et al. (2019)
2,456,397.42894		0.00031	-278	Mancini et al. (2015)	Mancini et al. (2015)
2,456,721.30085		0.00084	-34	Wang et al. (2019)	Wang et al. (2019)
2,456,725.28100		0.00068	-31	Wang et al. (2019)	Wang et al. (2019)
2,456,729.26439		0.00095	-28	Wang et al. (2019)	Wang et al. (2019)
2,456,749.17580		0.00108	-13	Wang et al. (2019)	Wang et al. (2019)
2,456,753.15819		0.00085	-10	Wang et al. (2019)	Wang et al. (2019)
2,456,762.44834		0.00018	-3	Mancini et al. (2015)	Mancini et al. (2015)
2,456,766.43055		0.00028	0	Mancini et al. (2015)	Mancini et al. (2015)
2,457,070.39280		0.00086	229	Wang et al. (2019)	Wang et al. (2019)
2,457,138.08645		0.00073	280	Wang et al. (2019)	Wang et al. (2019)
2,457,398.24830		0.00043	476	Wang et al. (2019)	Wang et al. (2019)
2,457,402.22948		0.00041	479	Wang et al. (2019)	Wang et al. (2019)
2,457,406.21179		0.00092	482	Wang et al. (2019)	Wang et al. (2019)
2,457,447.35849		0.00053	513	Wang et al. (2019)	Wang et al. (2019)
2,457,459.30494		0.00098	522	Wang et al. (2019)	Wang et al. (2019)
2,457,491.16331		0.00072	546	Wang et al. (2019)	Wang et al. (2019)
2,457,864.14544		0.00163	827	Wang et al. (2019)	Wang et al. (2019)
2,458,911.42299	0.00031	1616	This work	This work	
KELT-1	2,455,899.55385	0.00071	-1156	Sivard et al. (2012)	Maciejewski et al. (2018a)
	2,455,905.63900	0.00160	-1151	Sivard et al. (2012)	Maciejewski et al. (2018a)
	2,455,911.72593	0.00075	-1146	Sivard et al. (2012)	Maciejewski et al. (2018a)
	2,455,927.55589	0.00057	-1133	Sivard et al. (2012)	Maciejewski et al. (2018a)
	2,455,933.64303	0.00064	-1128	Sivard et al. (2012)	Maciejewski et al. (2018a)
	2,457,306.97602	0.00030	0	Beatty et al. (2019)	Beatty et al. (2019)
	2,457,959.55263	0.00054	536	Maciejewski et al. (2018a)	Maciejewski et al. (2018a)
	2,457,981.46777	0.00078	554	Maciejewski et al. (2018a)	Maciejewski et al. (2018a)
	2,458,015.55731	0.00046	582	Maciejewski et al. (2018a)	Maciejewski et al. (2018a)
	2,458,020.42711	0.00055	586	Maciejewski et al. (2018a)	Maciejewski et al. (2018a)
	2,458,026.51676	0.00074	591	Maciejewski et al. (2018a)	Maciejewski et al. (2018a)
	2,458,081.30196	0.00085	636	Maciejewski et al. (2018a)	Maciejewski et al. (2018a)
	2,458,126.34908	0.00085	673	Maciejewski et al. (2018a)	Maciejewski et al. (2018a)
	2,458,367.41290	0.00140	871	Maciejewski et al. (2018a)	Maciejewski et al. (2018a)
2,458,778.92707	0.00050	1209	This work	This work	
KELT-16	2,457,165.85142	0.00101	-919	Oberst et al. (2017)	Maciejewski et al. (2018a)
	2,457,166.82179	0.00089	-918	Oberst et al. (2017)	Maciejewski et al. (2018a)
	2,457,168.75660	0.00200	-916	Oberst et al. (2017)	Maciejewski et al. (2018a)
	2,457,198.79802	0.00074	-885	Oberst et al. (2017)	Maciejewski et al. (2018a)
	2,457,228.83690	0.00100	-854	Oberst et al. (2017)	Maciejewski et al. (2018a)
	2,457,238.52790	0.00180	-844	Oberst et al. (2017)	Maciejewski et al. (2018a)
	2,457,328.64440	0.00140	-751	Oberst et al. (2017)	Maciejewski et al. (2018a)
	2,457,329.61146	0.00094	-750	Oberst et al. (2017)	Maciejewski et al. (2018a)
	2,457,330.58151	0.00046	-749	Oberst et al. (2017)	Maciejewski et al. (2018a)
	2,457,363.52676	0.00101	-715	Oberst et al. (2017)	Maciejewski et al. (2018a)
	2,457,714.30206	0.00071	-353	Maciejewski et al. (2018a)	Maciejewski et al. (2018a)

Table D1
(Continued)

Target	T_0 (BJD _{TDB})	σ (days)	Epoch	Light-curve Source	Timing Source
	2,457,914.88456	0.00051	-146	Patra et al. (2020)	Patra et al. (2020)
	2,457,915.85370	0.00062	-145	Patra et al. (2020)	Patra et al. (2020)
	2,457,924.57245	0.00043	-136	Mancini et al. (2021)	Mancini et al. (2021)
	2,457,925.54315	0.00034	-135	Mancini et al. (2021)	Mancini et al. (2021)
	2,457,926.51262	0.00024	-134	Mancini et al. (2021)	Mancini et al. (2021)
	2,457,926.51262	0.00024	-134	Mancini et al. (2021)	Mancini et al. (2021)
	2,457,927.48073	0.00023	-133	Mancini et al. (2021)	Mancini et al. (2021)
	2,457,927.48156	0.00048	-133	Maciejewski et al. (2018a)	Maciejewski et al. (2018a)
	2,457,930.38847	0.00049	-130	Mancini et al. (2021)	Mancini et al. (2021)
	2,457,945.89131	0.00106	-114	Mancini et al. (2021)	Mancini et al. (2021)
	2,457,946.86111	0.00069	-113	Mancini et al. (2021)	Mancini et al. (2021)
	2,457,957.51989	0.00030	-102	Mancini et al. (2021)	Mancini et al. (2021)
	2,457,958.48844	0.00026	-101	Maciejewski et al. (2018a)	Maciejewski et al. (2018a)
	2,457,959.45852	0.00051	-100	Mancini et al. (2021)	Mancini et al. (2021)
	2,457,960.42762	0.00036	-99	Mancini et al. (2021)	Mancini et al. (2021)
	2,457,962.36544	0.00105	-97	Mancini et al. (2021)	Mancini et al. (2021)
	2,457,986.58974	0.00034	-72	Mancini et al. (2021)	Mancini et al. (2021)
	2,457,988.52797	0.00039	-70	Maciejewski et al. (2018a)	Maciejewski et al. (2018a)
	2,457,988.52836	0.00045	-70	Mancini et al. (2021)	Mancini et al. (2021)
	2,457,989.49700	0.00053	-69	Mancini et al. (2021)	Mancini et al. (2021)
	2,458,021.47285	0.00059	-36	Mancini et al. (2021)	Mancini et al. (2021)
	2,458,021.47346	0.00039	-36	Maciejewski et al. (2018a)	Maciejewski et al. (2018a)
	2,458,022.44176	0.00063	-35	Mancini et al. (2021)	Mancini et al. (2021)
	2,458,022.44219	0.00047	-35	Maciejewski et al. (2018a)	Maciejewski et al. (2018a)
	2,458,023.41090	0.00069	-34	Mancini et al. (2021)	Mancini et al. (2021)
	2,458,026.31752	0.00074	-31	Maciejewski et al. (2018a)	Maciejewski et al. (2018a)
	2,458,056.35704	0.00044	0	Mancini et al. (2021)	Mancini et al. (2021)
	2,458,301.51280	0.00030	253	Mancini et al. (2021)	Mancini et al. (2021)
	2,458,302.48200	0.00026	254	Mancini et al. (2021)	Mancini et al. (2021)
	2,458,303.44940	0.00054	255	Mancini et al. (2021)	Mancini et al. (2021)
	2,458,334.45858	0.00063	287	Maciejewski et al. (2018a)	Maciejewski et al. (2018a)
	2,458,365.46578	0.00064	319	Maciejewski et al. (2018a)	Maciejewski et al. (2018a)
	2,458,368.37232	0.00048	322	Maciejewski et al. (2018a)	Maciejewski et al. (2018a)
	2,458,401.31876	0.00028	356	Maciejewski et al. (2018a)	Maciejewski et al. (2018a)
	2,458,677.48078	0.00071	641	Mancini et al. (2021)	Mancini et al. (2021)
	2,458,710.42937	0.00123	675	Mancini et al. (2021)	Mancini et al. (2021)
	2,458,719.14831	0.00045	684	this work	this work
	2,458,743.37244	0.00090	709	Mancini et al. (2021)	Mancini et al. (2021)
	2,458,744.34073	0.00056	710	Mancini et al. (2021)	Mancini et al. (2021)
	2,458,990.46559	0.00084	964	Mancini et al. (2021)	Mancini et al. (2021)
	2,459,050.54472	0.00026	1026	Mancini et al. (2021)	Mancini et al. (2021)
KELT-20	2,457,301.62192	0.00086	-291	Lund et al. (2017)	Lund et al. (2017)
	2,457,544.81092	0.00051	-221	Lund et al. (2017)	Lund et al. (2017)
	2,457,551.75691	0.00064	-219	Lund et al. (2017)	Lund et al. (2017)
	2,457,697.67192	0.00072	-177	Lund et al. (2017)	Lund et al. (2017)
	2,457,881.79960	0.00056	-124	Lund et al. (2017)	Lund et al. (2017)
	2,457,881.79690	0.00064	-124	Lund et al. (2017)	Lund et al. (2017)
	2,457,881.79568	0.00087	-124	Lund et al. (2017)	Lund et al. (2017)
	2,457,888.74555	0.00059	-122	Lund et al. (2017)	Lund et al. (2017)
	2,457,916.53750	0.00058	-114	Lund et al. (2017)	Lund et al. (2017)
	2,458,312.58566	0.00022	0	Casasayas-Barris et al. (2019)	Casasayas-Barris et al. (2019)
	2,458,698.21073	0.00014	111	This work	This work
KELT-23A	2,458,144.89840	0.00046	-277	Johns et al. (2019)	Johns et al. (2019)
	2,458,144.89724	0.00044	-277	Johns et al. (2019)	Johns et al. (2019)
	2,458,153.91793	0.00059	-273	Johns et al. (2019)	Johns et al. (2019)
	2,458,167.44840	0.00110	-267	Johns et al. (2019)	Johns et al. (2019)
	2,458,187.74583	0.00064	-258	Johns et al. (2019)	Johns et al. (2019)
	2,458,196.77035	0.00110	-254	Johns et al. (2019)	Johns et al. (2019)
	2,458,196.77106	0.00063	-254	Johns et al. (2019)	Johns et al. (2019)
	2,458,196.77350	0.00119	-254	Johns et al. (2019)	Johns et al. (2019)
	2,458,273.45249	0.00098	-220	Johns et al. (2019)	Johns et al. (2019)
	2,458,769.61228	0.00006	0	This work	This work

Table D1
(Continued)

Target	T_0 (BJD _{TDB})	σ (days)	Epoch	Light-curve Source	Timing Source
Qatar-1	2,455,640.53380	0.00160	-576	von Essen et al. (2013)	Maciejewski et al. (2015)
	2,455,647.63267	0.00058	-571	von Essen et al. (2013)	Maciejewski et al. (2015)
	2,455,704.43426	0.00059	-531	von Essen et al. (2013)	Maciejewski et al. (2015)
	2,455,711.53450	0.00035	-526	von Essen et al. (2013), Covino et al. (2013)	Maciejewski et al. (2015)
	2,455,742.77475	0.00022	-504	Collins et al. (2017)	Collins et al. (2017)
	2,455,752.71499	0.00024	-497	Collins et al. (2017)	Collins et al. (2017)
	2,455,775.43517	0.00046	-481	von Essen et al. (2013), Maciejewski et al. (2015)	Maciejewski et al. (2015)
	2,455,789.63540	0.00025	-471	Collins et al. (2017)	Collins et al. (2017)
	2,455,796.73583	0.00021	-466	Collins et al. (2017)	Collins et al. (2017)
	2,455,799.57580	0.00020	-464	Mislis et al. (2015)	Mislis et al. (2015)
	2,455,799.57550	0.00010	-464	Mislis et al. (2015)	Mislis et al. (2015)
	2,455,799.57590	0.00020	-464	Mislis et al. (2015)	Mislis et al. (2015)
	2,455,799.57560	0.00010	-464	Mislis et al. (2015)	Mislis et al. (2015)
	2,455,799.57630	0.00032	-464	Covino et al. (2013)	Maciejewski et al. (2015)
	2,455,826.55618	0.00022	-445	Collins et al. (2017)	Collins et al. (2017)
	2,455,836.49672	0.00041	-438	von Essen et al. (2013)	Maciejewski et al. (2015)
	2,455,843.59664	0.00022	-433	Collins et al. (2017)	Collins et al. (2017)
	2,455,850.69628	0.00019	-428	Sada et al. (2012)	Sada et al. (2012)
	2,455,897.55768	0.00024	-395	Collins et al. (2017)	Collins et al. (2017)
	2,455,985.60050	0.00110	-333	von Essen et al. (2013)	Maciejewski et al. (2015)
	2,456,039.56043	0.00075	-295	von Essen et al. (2013)	Maciejewski et al. (2015)
	2,456,049.50010	0.00046	-288	von Essen et al. (2013)	Maciejewski et al. (2015)
	2,456,059.43930	0.00170	-281	von Essen et al. (2013)	Maciejewski et al. (2015)
	2,456,076.47920	0.00100	-269	von Essen et al. (2013)	Maciejewski et al. (2015)
	2,456,097.78070	0.00023	-254	Collins et al. (2017)	Collins et al. (2017)
	2,456,107.72152	0.00021	-247	Collins et al. (2017)	Collins et al. (2017)
	2,456,113.40040	0.00110	-243	von Essen et al. (2013)	Maciejewski et al. (2015)
	2,456,130.44153	0.00035	-231	Covino et al. (2013)	Maciejewski et al. (2015)
	2,456,140.38094	0.00055	-224	von Essen et al. (2013)	Maciejewski et al. (2015)
	2,456,141.80175	0.00029	-223	Collins et al. (2017)	Collins et al. (2017)
	2,456,151.74131	0.00028	-216	Collins et al. (2017)	Collins et al. (2017)
	2,456,157.42152	0.00044	-212	von Essen et al. (2013)	Maciejewski et al. (2015)
	2,456,161.68167	0.00027	-209	Collins et al. (2017)	Collins et al. (2017)
	2,456,164.52187	0.00042	-207	Covino et al. (2013)	Maciejewski et al. (2015)
	2,456,181.56264	0.00023	-195	Covino et al. (2013)	Maciejewski et al. (2015)
	2,456,201.44229	0.00066	-181	von Essen et al. (2013)	Maciejewski et al. (2015)
	2,456,225.58336	0.00027	-164	Collins et al. (2017)	Collins et al. (2017)
	2,456,231.26318	0.00051	-160	von Essen et al. (2013)	Maciejewski et al. (2015)
	2,456,275.28493	0.00043	-129	Maciejewski et al. (2015)	Maciejewski et al. (2015)
	2,456,458.46650	0.00020	0	Mislis et al. (2015)	Mislis et al. (2015)
	2,456,489.70762	0.00020	22	Collins et al. (2017)	Collins et al. (2017)
	2,456,539.40816	0.00065	57	Maciejewski et al. (2015)	Maciejewski et al. (2015)
	2,456,566.38885	0.00057	76	Maciejewski et al. (2015)	Maciejewski et al. (2015)
	2,456,623.18947	0.00060	116	Maciejewski et al. (2015)	Maciejewski et al. (2015)
	2,456,742.47200	0.00110	200	Maciejewski et al. (2015)	Maciejewski et al. (2015)
	2,456,749.57192	0.00038	205	Maciejewski et al. (2015)	Maciejewski et al. (2015)
	2,456,766.61200	0.00040	217	Mislis et al. (2015)	Mislis et al. (2015)
2,456,793.59237	0.00053	236	Maciejewski et al. (2015)	Maciejewski et al. (2015)	
2,456,803.53269	0.00028	243	Maciejewski et al. (2015)	Maciejewski et al. (2015)	
2,456,813.47200	0.00030	250	Mislis et al. (2015)	Mislis et al. (2015)	
2,456,813.47310	0.00020	250	Mislis et al. (2015)	Mislis et al. (2015)	
2,456,823.41500	0.00044	257	Püsküllü et al. (2017)	Püsküllü et al. (2017)	
2,456,830.51327	0.00033	262	Maciejewski et al. (2015)	Maciejewski et al. (2015)	
2,456,840.45424	0.00058	269	Maciejewski et al. (2015)	Maciejewski et al. (2015)	
2,456,840.45327	0.00042	269	Püsküllü et al. (2017)	Püsküllü et al. (2017)	
2,456,854.65325	0.00031	279	Collins et al. (2017)	Collins et al. (2017)	
2,456,861.75417	0.00032	284	Collins et al. (2017)	Collins et al. (2017)	
2,456,867.43480	0.00042	288	Püsküllü et al. (2017)	Püsküllü et al. (2017)	
2,456,888.73423	0.00030	303	Collins et al. (2017)	Collins et al. (2017)	
2,456,894.41548	0.00047	307	Püsküllü et al. (2017)	Püsküllü et al. (2017)	
2,456,908.61490	0.00020	317	Mislis et al. (2015)	Mislis et al. (2015)	
2,456,911.45488	0.00029	319	Maciejewski et al. (2015)	Maciejewski et al. (2015)	
2,456,918.55468	0.00056	324	Maciejewski et al. (2015)	Maciejewski et al. (2015)	
2,456,921.39618	0.00048	326	Püsküllü et al. (2017)	Püsküllü et al. (2017)	

Table D1
(Continued)

Target	T_0 (BJD _{TDB})	σ (days)	Epoch	Light-curve Source	Timing Source
	2,456,925.65523	0.00025	329	Collins et al. (2017)	Collins et al. (2017)
	2,456,928.49510	0.00032	331	Maciejewski et al. (2015)	Maciejewski et al. (2015)
	2,456,931.33528	0.00053	333	Püsküllü et al. (2017)	Püsküllü et al. (2017)
	2,456,958.31430	0.00120	352	Maciejewski et al. (2015)	Maciejewski et al. (2015)
	2,457,124.45935	0.00059	469	Püsküllü et al. (2017)	Püsküllü et al. (2017)
	2,457,168.48014	0.00058	500	Püsküllü et al. (2017)	Püsküllü et al. (2017)
	2,457,330.36216	0.00065	614	Püsküllü et al. (2017)	Püsküllü et al. (2017)
	2,457,340.30315	0.00064	621	Püsküllü et al. (2017)	Püsküllü et al. (2017)
	2,457,347.40134	0.00085	626	Püsküllü et al. (2017)	Püsküllü et al. (2017)
	2,457,570.34628	0.00050	783	Thakur et al. (2018)	Thakur et al. (2018)
	2,457,580.28552	0.00022	790	Thakur et al. (2018)	Thakur et al. (2018)
	2,457,634.24666	0.00035	828	Thakur et al. (2018)	Thakur et al. (2018)
	2,458,959.12981	0.00014	1761	This work	This work
TrES-3	2,454,185.91110	0.00020	-1076	O'Donovan et al. (2007)	Jiang et al. (2013)
	2,454,198.97359	0.00066	-1066	O'Donovan et al. (2007)	Jiang et al. (2013)
	2,454,214.64695	0.00036	-1054	Sozzetti et al. (2009)	Jiang et al. (2013)
	2,454,215.95288	0.00033	-1053	Sozzetti et al. (2009)	Jiang et al. (2013)
	2,454,532.04939	0.00033	-811	Christiansen et al. (2011)	Christiansen et al. (2011)
	2,454,533.35515	0.00035	-810	Christiansen et al. (2011)	Christiansen et al. (2011)
	2,454,534.66317	0.00019	-809	Gibson et al. (2009)	Jiang et al. (2013)
	2,454,535.96903	0.00039	-808	Sozzetti et al. (2009)	Jiang et al. (2013)
	2,454,538.58126	0.00035	-806	Christiansen et al. (2011)	Christiansen et al. (2011)
	2,454,539.88703	0.00040	-805	Christiansen et al. (2011)	Christiansen et al. (2011)
	2,454,541.19261	0.00035	-804	Christiansen et al. (2011)	Christiansen et al. (2011)
	2,454,542.49930	0.00041	-803	Christiansen et al. (2011)	Christiansen et al. (2011)
	2,454,552.94962	0.00022	-795	Sozzetti et al. (2009)	Jiang et al. (2013)
	2,454,569.92982	0.00040	-782	Sozzetti et al. (2009)	Jiang et al. (2013)
	2,454,594.74682	0.00037	-763	Sozzetti et al. (2009)	Jiang et al. (2013)
	2,454,615.64621	0.00021	-747	Gibson et al. (2009)	Jiang et al. (2013)
	2,454,632.62690	0.00020	-734	Gibson et al. (2009)	Jiang et al. (2013)
	2,454,649.60712	0.00019	-721	Gibson et al. (2009)	Jiang et al. (2013)
	2,454,653.52661	0.00092	-718	Gibson et al. (2009)	Jiang et al. (2013)
	2,454,662.66984	0.00060	-711	Gibson et al. (2009)	Jiang et al. (2013)
	2,454,670.50709	0.00034	-705	Gibson et al. (2009)	Jiang et al. (2013)
	2,454,674.42521	0.00028	-702	Gibson et al. (2009)	Jiang et al. (2013)
	2,454,683.56812	0.00042	-695	Gibson et al. (2009)	Jiang et al. (2013)
	2,454,957.86698	0.00048	-485	Sada et al. (2012)	Sada et al. (2012)
	2,454,959.17120	0.00110	-484	Lee et al. (2011)	Mannaday et al. (2020)
	2,454,964.40014	0.00095	-480	Vaňko et al. (2013)	Mannaday et al. (2020)
	2,454,965.70470	0.00023	-479	Kundurthy et al. (2013)	Mannaday et al. (2020)
	2,454,977.46000	0.00150	-470	Vaňko et al. (2013)	Mannaday et al. (2020)
	2,454,995.74737	0.00044	-456	Turner et al. (2013)	Mannaday et al. (2020)
	2,454,995.74657	0.00017	-456	Kundurthy et al. (2013)	Mannaday et al. (2020)
	2,455,004.88970	0.00018	-449	Turner et al. (2013)	Mannaday et al. (2020)
	2,455,017.95161	0.00033	-439	Turner et al. (2013)	Mannaday et al. (2020)
	2,455,045.38085	0.00063	-418	Vaňko et al. (2013)	Mannaday et al. (2020)
	2,455,049.29850	0.00150	-415	Maciejewski et al. (2013c)	Maciejewski et al. (2013c)
	2,455,054.52523	0.00018	-411	Cólon et al. (2010)	Jiang et al. (2013)
	2,455,058.44480	0.00100	-408	Vaňko et al. (2013)	Mannaday et al. (2020)
	2,455,277.88206	0.00038	-240	Kundurthy et al. (2013)	Mannaday et al. (2020)
	2,455,294.86465	0.00039	-227	Lee et al. (2011)	Mannaday et al. (2020)
	2,455,297.47780	0.00080	-225	Maciejewski et al. (2013c)	Maciejewski et al. (2013c)
	2,455,314.45500	0.00072	-212	Vaňko et al. (2013)	Mannaday et al. (2020)
	2,455,327.51720	0.00080	-202	Maciejewski et al. (2013c)	Maciejewski et al. (2013c)
	2,455,332.74259	0.00031	-198	Kundurthy et al. (2013)	Mannaday et al. (2020)
	2,455,341.88380	0.00110	-191	Jiang et al. (2013)	Jiang et al. (2013)
	2,455,358.86606	0.00076	-178	Jiang et al. (2013)	Jiang et al. (2013)
	2,455,358.86723	0.00070	-178	Lee et al. (2011)	Mannaday et al. (2020)
	2,455,362.78568	0.00057	-175	Lee et al. (2011)	Mannaday et al. (2020)
	2,455,362.78470	0.00110	-175	Jiang et al. (2013)	Jiang et al. (2013)
	2,455,365.39650	0.00120	-173	Maciejewski et al. (2013c)	Maciejewski et al. (2013c)
	2,455,366.70215	0.00080	-172	Jiang et al. (2013)	Jiang et al. (2013)
	2,455,375.84617	0.00090	-165	Jiang et al. (2013)	Jiang et al. (2013)

Table D1
(Continued)

Target	T_0 (BJD _{TDB})	σ (days)	Epoch	Light-curve Source	Timing Source
	2,455,378.45955	0.00090	-163	Vaňko et al. (2013)	Mannaday et al. (2020)
	2,455,416.33972	0.00056	-134	Vaňko et al. (2013)	Mannaday et al. (2020)
	2,455,429.39997	0.00046	-124	Vaňko et al. (2013)	Mannaday et al. (2020)
	2,455,446.38075	0.00021	-111	Vaňko et al. (2013)	Mannaday et al. (2020)
	2,455,479.03425	0.00094	-86	Sun et al. (2018)	Sun et al. (2018)
	2,455,481.64795	0.00018	-84	Kundurthy et al. (2013)	Mannaday et al. (2020)
	2,455,591.36690	0.00150	0	Sun et al. (2018)	Sun et al. (2018)
	2,455,643.61454	0.00034	40	Vaňko et al. (2013)	Mannaday et al. (2020)
	2,455,644.92122	0.00019	41	Kundurthy et al. (2013)	Mannaday et al. (2020)
	2,455,678.88252	0.00032	67	Kundurthy et al. (2013)	Mannaday et al. (2020)
	2,455,695.86223	0.00072	80	Kundurthy et al. (2013)	Mannaday et al. (2020)
	2,455,733.74164	0.00035	109	Kundurthy et al. (2013)	Mannaday et al. (2020)
	2,455,797.74568	0.00032	158	Kundurthy et al. (2013)	Mannaday et al. (2020)
	2,455,817.33688	0.00041	173	Vaňko et al. (2013)	Mannaday et al. (2020)
	2,456,011.95934	0.00073	322	Turner et al. (2013)	Mannaday et al. (2020)
	2,456,014.57219	0.00070	324	Turner et al. (2013)	Mannaday et al. (2020)
	2,456,014.57248	0.00065	324	Turner et al. (2013)	Mannaday et al. (2020)
	2,456,028.93996	0.00049	335	Turner et al. (2013)	Mannaday et al. (2020)
	2,456,077.27003	0.00037	372	Mannaday et al. (2020)	Mannaday et al. (2020)
	2,456,082.49260	0.00120	376	Püsküllü et al. (2017)	Mannaday et al. (2020)
	2,456,086.41120	0.00100	379	Püsküllü et al. (2017)	Mannaday et al. (2020)
	2,456,099.47337	0.00160	389	Mannaday et al. (2020)	Mannaday et al. (2020)
	2,456,368.54705	0.00063	595	Maciejewski et al. (2013c)	Maciejewski et al. (2013c)
	2,456,393.36471	0.00050	614	Mannaday et al. (2020)	Mannaday et al. (2020)
	2,456,423.40717	0.00079	637	Mannaday et al. (2020)	Mannaday et al. (2020)
	2,456,431.24526	0.00032	643	Mannaday et al. (2020)	Mannaday et al. (2020)
	2,456,440.38874	0.00063	650	Püsküllü et al. (2017)	Mannaday et al. (2020)
	2,456,487.41277	0.00075	686	Püsküllü et al. (2017)	Mannaday et al. (2020)
	2,456,747.34245	0.00019	885	Mannaday et al. (2020)	Mannaday et al. (2020)
	2,456,841.38981	0.00079	957	Püsküllü et al. (2017)	Mannaday et al. (2020)
	2,457,140.50425	0.00041	1186	Püsküllü et al. (2017)	Mannaday et al. (2020)
	2,457,204.50652	0.00089	1235	Püsküllü et al. (2017)	Mannaday et al. (2020)
	2,457,212.34484	0.00052	1241	Püsküllü et al. (2017)	Mannaday et al. (2020)
	2,457,221.48724	0.00063	1248	Ricci et al. (2017)	Mannaday et al. (2020)
	2,457,225.40653	0.00036	1251	Püsküllü et al. (2017)	Mannaday et al. (2020)
	2,457,238.46724	0.00066	1261	Ricci et al. (2017)	Mannaday et al. (2020)
	2,457,242.38679	0.00025	1264	Püsküllü et al. (2017)	Mannaday et al. (2020)
	2,457,256.75464	0.00074	1275	Ricci et al. (2017)	Mannaday et al. (2020)
	2,457,259.36698	0.00058	1277	Püsküllü et al. (2017)	Mannaday et al. (2020)
	2,457,491.86832	0.00041	1455	Ricci et al. (2017)	Mannaday et al. (2020)
	2,457,542.80916	0.00026	1494	Ricci et al. (2017)	Mannaday et al. (2020)
	2,458,185.45419	0.00064	1986	Mannaday et al. (2020)	Mannaday et al. (2020)
	2,458,189.37246	0.00068	1989	Mannaday et al. (2020)	Mannaday et al. (2020)
	2,458,202.43178	0.00150	1999	Mannaday et al. (2020)	Mannaday et al. (2020)
	2,458,206.35282	0.00076	2002	Mannaday et al. (2020)	Mannaday et al. (2020)
	2,458,219.41292	0.00058	2012	Mannaday et al. (2020)	Mannaday et al. (2020)
	2,458,223.33346	0.00053	2015	Mannaday et al. (2020)	Mannaday et al. (2020)
	2,458,347.42160	0.00020	2110	von Essen et al. (2019)	von Essen et al. (2019)
	2,459,008.35101	0.00022	2616	This work	This work
WASP-3	2,454,143.85104	0.00040	-660	Pollacco et al. (2008)	Pollacco et al. (2008)
	2,454,601.86671	0.00026	-412	Tripathi et al. (2010)	Nascimbeni et al. (2013)
	2,454,605.56042	0.00030	-410	Gibson et al. (2008)	Nascimbeni et al. (2013)
	2,454,638.80399	0.00034	-392	Tripathi et al. (2010)	Nascimbeni et al. (2013)
	2,454,660.96479	0.00015	-380	Tripathi et al. (2010)	Nascimbeni et al. (2013)
	2,454,679.43318	0.00042	-370	Christiansen et al. (2011)	Nascimbeni et al. (2013)
	2,454,681.27967	0.00034	-369	Christiansen et al. (2011)	Nascimbeni et al. (2013)
	2,454,683.12798	0.00049	-368	Christiansen et al. (2011)	Nascimbeni et al. (2013)
	2,454,684.97524	0.00040	-367	Christiansen et al. (2011)	Nascimbeni et al. (2013)
	2,454,692.36168	0.00056	-363	Christiansen et al. (2011)	Nascimbeni et al. (2013)
	2,454,694.20776	0.00083	-362	Christiansen et al. (2011)	Nascimbeni et al. (2013)
	2,454,712.67641	0.00064	-352	Nascimbeni et al. (2013)	Nascimbeni et al. (2013)
	2,454,714.52368	0.00041	-351	Gibson et al. (2008)	Nascimbeni et al. (2013)
	2,454,963.84450	0.00081	-216	Tripathi et al. (2010)	Nascimbeni et al. (2013)

Table D1
(Continued)

Target	T_0 (BJD _{TDB})	σ (days)	Epoch	Light-curve Source	Timing Source
	2,454,963.84527	0.00118	-216	Sada et al. (2012)	Nascimbeni et al. (2013)
	2,454,967.53651	0.00085	-214	Mantalto et al. (2012)	Mantalto et al. (2012)
	2,454,976.77284	0.00030	-209	Tripathi et al. (2010)	Nascimbeni et al. (2013)
	2,454,987.85256	0.00093	-203	Nascimbeni et al. (2013)	Nascimbeni et al. (2013)
	2,455,037.71878	0.00086	-176	Nascimbeni et al. (2013)	Nascimbeni et al. (2013)
	2,455,041.41172	0.00035	-174	Damasso et al. (2010)	Nascimbeni et al. (2013)
	2,455,041.41255	0.00058	-174	Maciejewski et al. (2010)	Nascimbeni et al. (2013)
	2,455,065.42023	0.00036	-161	Maciejewski et al. (2010)	Nascimbeni et al. (2013)
	2,455,078.34809	0.00114	-154	Maciejewski et al. (2010)	Nascimbeni et al. (2013)
	2,455,098.66406	0.00044	-143	Maciejewski et al. (2013b)	Maciejewski et al. (2013b)
	2,455,102.36030	0.00084	-141	Maciejewski et al. (2010)	Nascimbeni et al. (2013)
	2,455,139.29753	0.00073	-121	Maciejewski et al. (2010)	Nascimbeni et al. (2013)
	2,455,305.51117	0.00056	-31	Maciejewski et al. (2010)	Nascimbeni et al. (2013)
	2,455,342.44700	0.00120	-11	Maciejewski et al. (2013b)	Maciejewski et al. (2013b)
	2,455,349.83390	0.00069	-7	Sada et al. (2012)	Nascimbeni et al. (2013)
	2,455,349.83306	0.00090	-7	Sada et al. (2012)	Nascimbeni et al. (2013)
	2,455,355.37419	0.00053	-4	Maciejewski et al. (2013b)	Maciejewski et al. (2013b)
	2,455,362.76233	0.00040	0	Maciejewski et al. (2013b)	Maciejewski et al. (2013b)
	2,455,366.45610	0.00100	2	Maciejewski et al. (2013b)	Maciejewski et al. (2013b)
	2,455,401.54564	0.00036	21	Maciejewski et al. (2013b)	Maciejewski et al. (2013b)
	2,455,423.70889	0.00048	33	Nascimbeni et al. (2013)	Nascimbeni et al. (2013)
	2,455,436.63530	0.00100	40	Maciejewski et al. (2013b)	Maciejewski et al. (2013b)
	2,455,438.48270	0.00060	41	Maciejewski et al. (2013b)	Maciejewski et al. (2013b)
	2,455,451.41010	0.00040	48	Maciejewski et al. (2013b)	Maciejewski et al. (2013b)
	2,455,654.56180	0.00140	158	Maciejewski et al. (2013b)	Maciejewski et al. (2013b)
	2,455,665.64627	0.00069	164	Mantalto et al. (2012)	Mantalto et al. (2012)
	2,455,678.57065	0.00106	171	Mantalto et al. (2012)	Mantalto et al. (2012)
	2,455,689.65263	0.00015	177	Nascimbeni et al. (2013)	Nascimbeni et al. (2013)
	2,455,691.49938	0.00086	178	Maciejewski et al. (2013b)	Maciejewski et al. (2013b)
	2,455,698.88641	0.00027	182	Maciejewski et al. (2013b)	Maciejewski et al. (2013b)
	2,455,698.88476	0.00160	182	Sada et al. (2012)	Nascimbeni et al. (2013)
	2,455,702.58052	0.00028	184	Nascimbeni et al. (2013)	Nascimbeni et al. (2013)
	2,455,715.50824	0.00072	191	Maciejewski et al. (2013b)	Maciejewski et al. (2013b)
	2,455,715.50608	0.00074	191	Mantalto et al. (2012)	Mantalto et al. (2012)
	2,455,728.43608	0.00052	198	Maciejewski et al. (2013b)	Maciejewski et al. (2013b)
	2,455,739.51620	0.00017	204	Nascimbeni et al. (2013)	Nascimbeni et al. (2013)
	2,455,739.51735	0.00064	204	Maciejewski et al. (2013b)	Maciejewski et al. (2013b)
	2,455,748.75070	0.00110	209	Maciejewski et al. (2013b)	Maciejewski et al. (2013b)
	2,455,763.52552	0.00070	217	Mantalto et al. (2012)	Mantalto et al. (2012)
	2,455,763.52511	0.00031	217	Nascimbeni et al. (2013)	Nascimbeni et al. (2013)
	2,455,765.37180	0.00140	218	Maciejewski et al. (2013b)	Maciejewski et al. (2013b)
	2,455,776.45452	0.00092	224	Maciejewski et al. (2013b)	Maciejewski et al. (2013b)
	2,455,787.53583	0.00053	230	Maciejewski et al. (2013b)	Maciejewski et al. (2013b)
	2,455,787.53379	0.00080	230	Mantalto et al. (2012)	Mantalto et al. (2012)
	2,455,800.46112	0.00170	237	Mantalto et al. (2012)	Mantalto et al. (2012)
	2,455,800.46137	0.00055	237	Maciejewski et al. (2013b)	Maciejewski et al. (2013b)
	2,455,813.38910	0.00150	244	Maciejewski et al. (2013b)	Maciejewski et al. (2013b)
	2,455,813.38792	0.00098	244	Mantalto et al. (2012)	Mantalto et al. (2012)
	2,455,837.39876	0.00044	257	Maciejewski et al. (2013b)	Maciejewski et al. (2013b)
	2,455,850.32740	0.00100	264	Maciejewski et al. (2013b)	Maciejewski et al. (2013b)
	2,458,223.50975	0.00078	1549	Maciejewski et al. (2018b)	Maciejewski et al. (2018b)
	2,459,023.18947	0.00029	1982	This work	This work
WASP-12	2,454,515.52496	0.00043	-2022	Hebb et al. (2009)	Maciejewski et al. (2013a)
	2,454,836.40340	0.00028	-1728	Copperwheat et al. (2013)	Maciejewski et al. (2016)
	2,454,840.76893	0.00062	-1724	Chan et al. (2011)	Maciejewski et al. (2016)
	2,455,140.90981	0.00042	-1449	Collins et al. (2017)	Collins et al. (2017)
	2,455,147.45861	0.00043	-1443	Maciejewski et al. (2013a)	Maciejewski et al. (2016)
	2,455,163.83061	0.00032	-1428	Collins et al. (2017)	Collins et al. (2017)
	2,455,172.56138	0.00036	-1420	Chan et al. (2011)	Maciejewski et al. (2016)
	2,455,209.66895	0.00046	-1386	Collins et al. (2017)	Collins et al. (2017)
	2,455,210.76151	0.00041	-1385	Collins et al. (2017)	Collins et al. (2017)
	2,455,230.40653	0.00024	-1367	Maciejewski et al. (2011)	Maciejewski et al. (2016)
	2,455,254.41761	0.00043	-1345	Maciejewski et al. (2011)	Maciejewski et al. (2016)

Table D1
(Continued)

Target	T_0 (BJD _{TDB})	σ (days)	Epoch	Light-curve Source	Timing Source
	2,455,494.52999	0.00074	-1125	Maciejewski et al. (2013a)	Maciejewski et al. (2016)
	2,455,498.89590	0.00079	-1121	Sada et al. (2012)	Sada et al. (2012)
	2,455,509.80971	0.00037	-1111	Collins et al. (2017)	Collins et al. (2017)
	2,455,510.90218	0.00031	-1110	Collins et al. (2017)	Collins et al. (2017)
	2,455,518.54147	0.00040	-1103	Cowan et al. (2012)	Maciejewski et al. (2016)
	2,455,542.55210	0.00040	-1081	Cowan et al. (2012)	Cowan et al. (2012)
	2,455,542.55273	0.00029	-1081	Maciejewski et al. (2013a)	Maciejewski et al. (2016)
	2,455,590.57561	0.00071	-1037	Maciejewski et al. (2013a)	Maciejewski et al. (2016)
	2,455,598.21552	0.00035	-1030	Maciejewski et al. (2013a)	Maciejewski et al. (2016)
	2,455,600.39800	0.00030	-1028	Maciejewski et al. (2013a)	Maciejewski et al. (2016)
	2,455,601.49010	0.00024	-1027	Maciejewski et al. (2013a)	Maciejewski et al. (2016)
	2,455,603.67261	0.00029	-1025	Collins et al. (2017)	Collins et al. (2017)
	2,455,623.31829	0.00039	-1007	Maciejewski et al. (2013a)	Maciejewski et al. (2016)
	2,455,876.52786	0.00027	-775	Maciejewski et al. (2013a)	Maciejewski et al. (2016)
	2,455,887.44198	0.00021	-765	Maciejewski et al. (2013a)	Maciejewski et al. (2016)
	2,455,888.53340	0.00027	-764	Maciejewski et al. (2013a)	Maciejewski et al. (2016)
	2,455,890.71635	0.00024	-762	Maciejewski et al. (2013a)	Maciejewski et al. (2016)
	2,455,903.81357	0.00032	-750	Collins et al. (2017)	Collins et al. (2017)
	2,455,920.18422	0.00031	-735	Maciejewski et al. (2013a)	Maciejewski et al. (2016)
	2,455,923.45850	0.00022	-732	Maciejewski et al. (2013a)	Maciejewski et al. (2016)
	2,455,946.37823	0.00018	-711	Maciejewski et al. (2013a)	Maciejewski et al. (2016)
	2,455,947.47015	0.00017	-710	Maciejewski et al. (2013a)	Maciejewski et al. (2016)
	2,455,948.56112	0.00034	-709	Maciejewski et al. (2013a)	Maciejewski et al. (2016)
	2,455,951.83536	0.00011	-706	Stevenson et al. (2014b)	Maciejewski et al. (2016)
	2,455,952.92708	0.00013	-705	Stevenson et al. (2014b)	Maciejewski et al. (2016)
	2,455,959.47543	0.00017	-699	Maciejewski et al. (2013a)	Maciejewski et al. (2016)
	2,455,970.38941	0.00040	-689	Maciejewski et al. (2013a)	Maciejewski et al. (2016)
	2,455,971.48111	0.00035	-688	Maciejewski et al. (2013a)	Maciejewski et al. (2016)
	2,455,982.39509	0.00034	-678	Maciejewski et al. (2013a)	Maciejewski et al. (2016)
	2,455,983.48695	0.00035	-677	Maciejewski et al. (2013a)	Maciejewski et al. (2016)
	2,455,984.57797	0.00032	-676	Collins et al. (2017)	Collins et al. (2017)
	2,455,985.66975	0.00042	-675	Collins et al. (2017)	Collins et al. (2017)
	2,455,996.58378	0.00037	-665	Collins et al. (2017)	Collins et al. (2017)
	2,456,005.31533	0.00037	-657	Maciejewski et al. (2013a)	Maciejewski et al. (2016)
	2,456,006.40637	0.00033	-656	Maciejewski et al. (2013a)	Maciejewski et al. (2016)
	2,456,245.42729	0.00033	-437	Maciejewski et al. (2016)	Maciejewski et al. (2016)
	2,456,249.79404	0.00039	-433	Collins et al. (2017)	Collins et al. (2017)
	2,456,273.80514	0.00030	-411	Collins et al. (2017)	Collins et al. (2017)
	2,456,282.53584	0.00030	-403	Maciejewski et al. (2016)	Maciejewski et al. (2016)
	2,456,284.71857	0.00030	-401	Collins et al. (2017)	Collins et al. (2017)
	2,456,297.81605	0.00030	-389	Collins et al. (2017)	Collins et al. (2017)
	2,456,302.18179	0.00046	-385	Maciejewski et al. (2016)	Maciejewski et al. (2016)
	2,456,305.45536	0.00026	-382	Maciejewski et al. (2016)	Maciejewski et al. (2016)
	2,456,319.64424	0.00038	-369	Collins et al. (2017)	Collins et al. (2017)
	2,456,328.37556	0.00027	-361	Maciejewski et al. (2016)	Maciejewski et al. (2016)
	2,456,329.46733	0.00029	-360	Maciejewski et al. (2016)	Maciejewski et al. (2016)
	2,456,604.50489	0.00021	-108	Maciejewski et al. (2016)	Maciejewski et al. (2016)
	2,456,605.59624	0.00030	-107	Maciejewski et al. (2016)	Maciejewski et al. (2016)
	2,456,606.68760	0.00034	-106	Maciejewski et al. (2016)	Maciejewski et al. (2016)
	2,456,607.77938	0.00071	-105	Collins et al. (2017)	Collins et al. (2017)
	2,456,629.60726	0.00019	-85	Maciejewski et al. (2016)	Maciejewski et al. (2016)
	2,456,630.69917	0.00043	-84	Maciejewski et al. (2016)	Maciejewski et al. (2016)
	2,456,654.71047	0.00034	-62	Collins et al. (2017)	Collins et al. (2017)
	2,456,662.35014	0.00019	-55	Maciejewski et al. (2016)	Maciejewski et al. (2016)
	2,456,663.44136	0.00019	-54	Maciejewski et al. (2016)	Maciejewski et al. (2016)
	2,456,664.53256	0.00032	-53	Maciejewski et al. (2016)	Maciejewski et al. (2016)
	2,456,677.63039	0.00032	-41	Collins et al. (2017)	Collins et al. (2017)
	2,456,688.54384	0.00041	-31	Maciejewski et al. (2016)	Maciejewski et al. (2016)
	2,456,711.46415	0.00026	-10	Maciejewski et al. (2016)	Maciejewski et al. (2016)
	2,456,722.37807	0.00047	0	Maciejewski et al. (2016)	Maciejewski et al. (2016)
	2,456,986.50195	0.00043	242	Maciejewski et al. (2016)	Maciejewski et al. (2016)
	2,457,010.51298	0.00039	264	Maciejewski et al. (2016)	Maciejewski et al. (2016)
	2,457,012.69617	0.00049	266	Collins et al. (2017)	Collins et al. (2017)

Table D1
(Continued)

Target	T_0 (BJD _{TDB})	σ (days)	Epoch	Light-curve Source	Timing Source
	2,457,045.43831	0.00049	296	Maciejewski et al. (2016)	Maciejewski et al. (2016)
	2,457,046.53019	0.00049	297	Maciejewski et al. (2016)	Maciejewski et al. (2016)
	2,457,059.62713	0.00035	309	Collins et al. (2017)	Collins et al. (2017)
	2,457,060.71839	0.00036	310	Collins et al. (2017)	Collins et al. (2017)
	2,457,067.26715	0.00023	316	Maciejewski et al. (2016)	Maciejewski et al. (2016)
	2,457,068.35834	0.00021	317	Maciejewski et al. (2016)	Maciejewski et al. (2016)
	2,457,103.28423	0.00031	349	Maciejewski et al. (2016)	Maciejewski et al. (2016)
	2,457,345.57867	0.00042	571	Maciejewski et al. (2016)	Maciejewski et al. (2016)
	2,457,390.32708	0.00034	612	Maciejewski et al. (2016)	Maciejewski et al. (2016)
	2,457,391.41818	0.00033	613	Maciejewski et al. (2016)	Maciejewski et al. (2016)
	2,457,426.34324	0.00055	645	Maciejewski et al. (2016)	Maciejewski et al. (2016)
	2,457,427.43496	0.00023	646	Maciejewski et al. (2016)	Maciejewski et al. (2016)
	2,457,451.44617	0.00021	668	Maciejewski et al. (2018a)	Maciejewski et al. (2018a)
	2,457,671.91324	0.00035	870	Patra et al. (2017)	Patra et al. (2017)
	2,457,691.55888	0.00025	888	Maciejewski et al. (2018a)	Maciejewski et al. (2018a)
	2,457,703.56388	0.00034	899	Maciejewski et al. (2018a)	Maciejewski et al. (2018a)
	2,457,706.83791	0.00037	902	Patra et al. (2017)	Patra et al. (2017)
	2,457,726.48400	0.00028	920	Maciejewski et al. (2018a)	Maciejewski et al. (2018a)
	2,457,727.57547	0.00023	921	Maciejewski et al. (2018a)	Maciejewski et al. (2018a)
	2,457,765.77515	0.00028	956	Patra et al. (2017)	Patra et al. (2017)
	2,457,766.86633	0.00039	957	Patra et al. (2017)	Patra et al. (2017)
	2,457,772.32407	0.00024	962	Maciejewski et al. (2018a)	Maciejewski et al. (2018a)
	2,457,773.41517	0.00022	963	Maciejewski et al. (2018a)	Maciejewski et al. (2018a)
	2,457,776.68869	0.00029	966	Patra et al. (2017)	Patra et al. (2017)
	2,457,781.05566	0.00036	970	Patra et al. (2020)	Patra et al. (2020)
	2,457,781.05418	0.00043	970	Patra et al. (2020)	Patra et al. (2020)
	2,457,786.51210	0.00026	975	Maciejewski et al. (2018a)	Maciejewski et al. (2018a)
	2,457,788.69464	0.00048	977	Patra et al. (2017)	Patra et al. (2017)
	2,457,800.69978	0.00032	988	Patra et al. (2017)	Patra et al. (2017)
	2,457,808.34020	0.00040	995	Öztürk & Erdem (2019)	Öztürk & Erdem (2019)
	2,457,809.43190	0.00018	996	Maciejewski et al. (2018a)	Maciejewski et al. (2018a)
	2,457,810.52327	0.00021	997	Maciejewski et al. (2018a)	Maciejewski et al. (2018a)
	2,458,026.62368	0.00056	1195	Maciejewski et al. (2018a)	Maciejewski et al. (2018a)
	2,458,050.63519	0.00023	1217	Maciejewski et al. (2018a)	Maciejewski et al. (2018a)
	2,458,060.45870	0.00030	1226	Öztürk & Erdem (2019)	Öztürk & Erdem (2019)
	2,458,073.55509	0.00022	1238	Maciejewski et al. (2018a)	Maciejewski et al. (2018a)
	2,458,074.64651	0.00034	1239	Maciejewski et al. (2018a)	Maciejewski et al. (2018a)
	2,458,077.92107	0.00028	1242	Yee et al. (2020)	Yee et al. (2020)
	2,458,123.76011	0.00027	1284	Yee et al. (2020)	Yee et al. (2020)
	2,458,124.85183	0.00035	1285	Yee et al. (2020)	Yee et al. (2020)
	2,458,132.49121	0.00031	1292	Maciejewski et al. (2018a)	Maciejewski et al. (2018a)
	2,458,134.67471	0.00032	1294	Yee et al. (2020)	Yee et al. (2020)
	2,458,136.85760	0.00033	1296	Yee et al. (2020)	Yee et al. (2020)
	2,458,155.41040	0.00050	1313	Öztürk & Erdem (2019)	Öztürk & Erdem (2019)
	2,458,155.41152	0.00031	1313	Maciejewski et al. (2018a)	Maciejewski et al. (2018a)
	2,458,156.50267	0.00032	1314	Maciejewski et al. (2018a)	Maciejewski et al. (2018a)
	2,458,159.77773	0.00091	1317	Yee et al. (2020)	Yee et al. (2020)
	2,458,161.95991	0.00035	1319	Patra et al. (2020)	Patra et al. (2020)
	2,458,161.95964	0.00026	1319	Patra et al. (2020)	Patra et al. (2020)
	2,458,163.05125	0.00021	1320	Patra et al. (2020)	Patra et al. (2020)
	2,458,163.05089	0.00034	1320	Patra et al. (2020)	Patra et al. (2020)
	2,458,166.32575	0.00034	1323	Maciejewski et al. (2018a)	Maciejewski et al. (2018a)
	2,458,178.33104	0.00038	1334	Maciejewski et al. (2018a)	Maciejewski et al. (2018a)
	2,458,411.89495	0.00040	1548	Yee et al. (2020)	Yee et al. (2020)
	2,458,471.92257	0.00026	1603	Yee et al. (2020)	Yee et al. (2020)
	2,458,494.84270	0.00030	1624	Yee et al. (2020)	Yee et al. (2020)
	2,458,506.84758	0.00044	1635	Yee et al. (2020)	Yee et al. (2020)
	2,458,853.91918	0.00021	1953	This work	This work
WASP-92	2,456,381.28418	0.00028	0	Hay et al. (2016)	Hay et al. (2016)
	2,458,971.32011	0.00058	1191	This work	This work
WASP-93	2,456,079.56495	0.00046	0	Hay et al. (2016)	Hay et al. (2016)
	2,458,779.31199	0.00062	988	This work	This work

Table D1
(Continued)

Target	T_0 (BJD _{TDB})	σ (days)	Epoch	Light-curve Source	Timing Source
WASP-135	2,455,230.99020	0.00090	−2154	Spake et al. (2016)	Spake et al. (2016)
	2,457,924.43994	0.00022	−232	Öztürk & Erdem (2021)	Öztürk & Erdem (2021)
	2,458,249.56016	0.00018	0	Öztürk & Erdem (2021)	Öztürk & Erdem (2021)
	2,458,280.38743	0.00064	22	Öztürk & Erdem (2021)	Öztürk & Erdem (2021)
	2,458,301.41018	0.00028	37	Öztürk & Erdem (2021)	Öztürk & Erdem (2021)
	2,458,336.44162	0.00044	62	Öztürk & Erdem (2021)	Öztürk & Erdem (2021)
	2,458,381.28867	0.00043	94	Öztürk & Erdem (2021)	Öztürk & Erdem (2021)
	2,458,388.29083	0.00052	99	Öztürk & Erdem (2021)	Öztürk & Erdem (2021)
	2,459,021.71876	0.00072	551	This work	This work

(This table is available in its entirety in machine-readable form.)

Appendix E Updated Transit Ephemeris Fits

Figure E1 shows the results from our updated transit ephemeris fits for the 11 systems with at least three published transit-timing measurements. The black and red data points correspond to the previously published transit timings and the

new TESS-epoch mid-transit times, respectively. The shaded blue region indicates the 1σ confidence region relative to the best-fit linear transit ephemeris (see Table 9). The orbit of WASP-12 is decaying, and we have included an additional panel showing the residuals from the best-fit quadratic transit model.

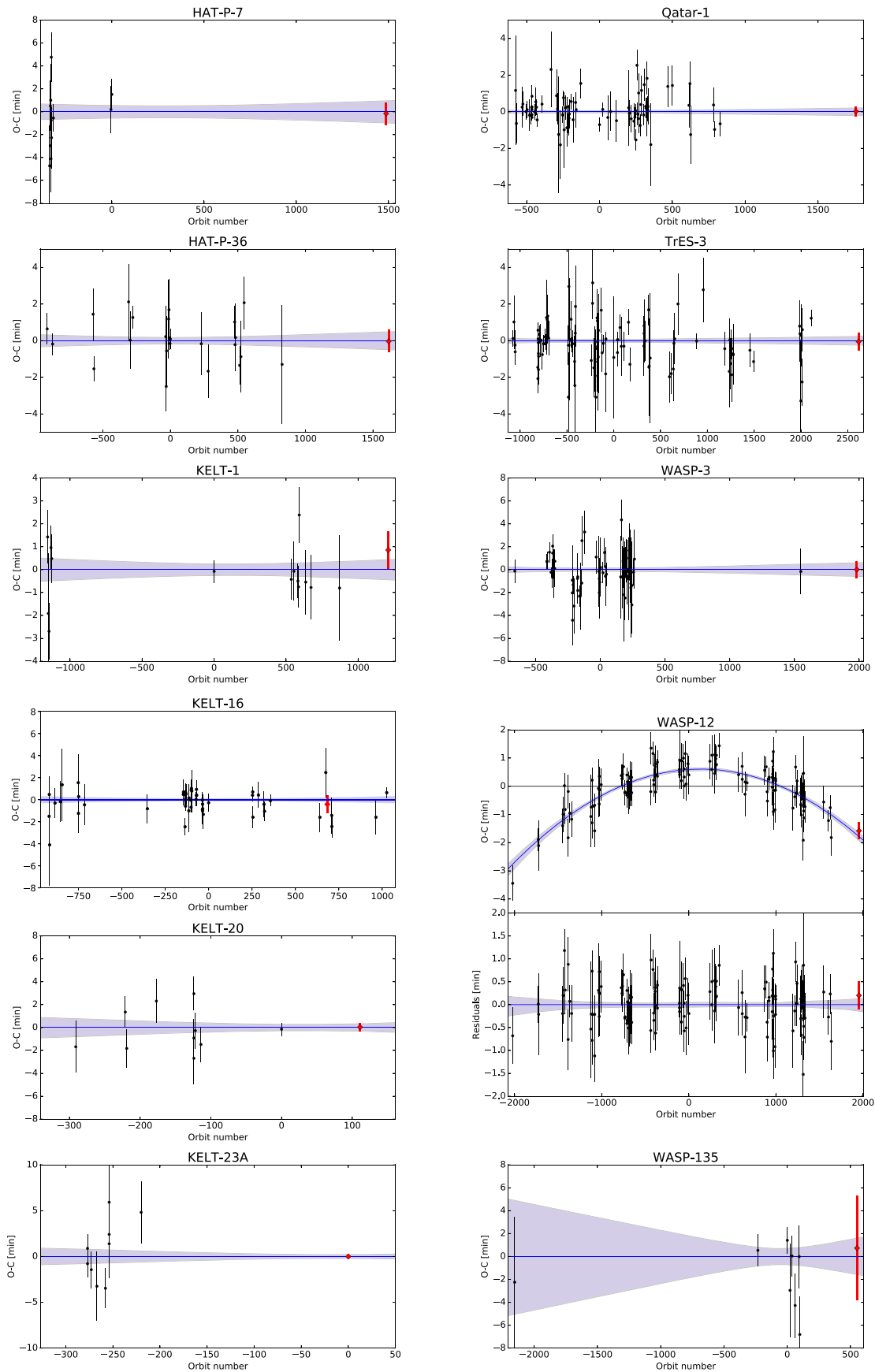





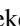

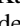


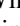



Figure E1. Observed minus calculated ($O - C$) plots for the 11 systems with more than two published transit timings. The TESS measurements are shown in red.

ORCID iDs

Ian Wong  <https://orcid.org/0000-0001-9665-8429>
 Daniel Kitzmann  <https://orcid.org/0000-0003-4269-3311>
 Avi Shporer  <https://orcid.org/0000-0002-1836-3120>
 Kevin Heng  <https://orcid.org/0000-0003-1907-5910>
 Tara Fetherolf  <https://orcid.org/0000-0002-3551-279X>
 Björn Benneke  <https://orcid.org/0000-0001-5578-1498>
 Tansu Daylan  <https://orcid.org/0000-0002-6939-9211>
 Stephen R. Kane  <https://orcid.org/0000-0002-7084-0529>
 Roland Vanderspek  <https://orcid.org/0000-0001-6763-6562>
 Sara Seager  <https://orcid.org/0000-0002-6892-6948>
 Joshua N. Winn  <https://orcid.org/0000-0002-4265-047X>
 Jon M. Jenkins  <https://orcid.org/0000-0002-4715-9460>
 Eric B. Ting  <https://orcid.org/0000-0002-8219-9505>

References

- Ahlers, J. P., Johnson, M. C., Stassun, K. G., et al. 2020, *AJ*, 160, 4
 Alsubai, K. A., Parley, N. R., Bramich, D. M., et al. 2011, *MNRAS*, 417, 709
 Angerhausen, D., DeLarme, E., & Morse, J. A. 2015, *PASP*, 127, 1113
 Arcangeli, J., Désert, J.-M., Line, M. R., et al. 2018, *ApJL*, 855, L30
 Armstrong, D. J., de Mooij, E., Barstow, J., et al. 2016, *NatAs*, 1, 4
 Baines, K. H., Sromovsky, L. A., Carlson, R. W., Momary, T. W., & Fry, P. M. 2019, *Icar*, 330, 217
 Bakos, G. Á., Hartman, J. D., Torres, G., et al. 2012, *AJ*, 144, 19
 Baskin, N. J., Knutson, H. A., Burrows, A., et al. 2013, *ApJ*, 773, 124
 Beatty, T. G., Collins, K. A., Fortney, J., et al. 2014, *ApJ*, 783, 112
 Beatty, T. G., Madhusudhan, N., Tsirias, A., et al. 2017, *AJ*, 154, 158
 Beatty, T. G., Marley, M. S., Gaudi, B. S., et al. 2019, *AJ*, 158, 166
 Beatty, T. G., Wong, I., Fetherolf, T., et al. 2020, *AJ*, 160, 211
 Beerer, I. M., Knutson, H. A., Burrows, A., et al. 2011, *ApJ*, 727, 23
 Bell, T. J., Dang, L., Cowan, N. B., et al. 2021, *MNRAS*, 504, 3316
 Bell, T. J., Zhang, M., Cubillos, P. E., et al. 2019, *MNRAS*, 489, 1995
 Benneke, B., Knutson, H. A., Lothringer, J., et al. 2019, *NatAs*, 3, 813
 Bond, G. P. 1861, *MNRAS*, 21, 197
 Borucki, W. J., Koch, D., Jenkins, J., et al. 2009, *Sci*, 325, 709
 Bouma, L. G., Winn, J. N., Baxter, C., et al. 2019, *AJ*, 157, 217
 Bourrier, V., Kitzmann, D., Kuntzer, T., et al. 2020, *A&A*, 637, A36
 Braude, A. S., Irwin, P. G. J., Orton, G. S., & Fletcher, L. N. 2020, *Icar*, 338, 113589
 Campo, C. J., Harrington, J., Hardy, R. A., et al. 2011, *ApJ*, 727, 125
 Casasayas-Barris, N., Pallé, E., Yan, F., et al. 2019, *A&A*, 628, A9
 Chan, T., Ingemyr, M., Winn, J. N., et al. 2011, *AJ*, 141, 179
 Christiansen, J. L., Ballard, S., Charbonneau, D., et al. 2010, *ApJ*, 710, 97
 Christiansen, J. L., Ballard, S., Charbonneau, D., et al. 2011, *ApJ*, 726, 94
 Claret, A. 2017, *A&A*, 600, A30
 Collins, K. A., Kielkopf, J. F., & Stassun, K. G. 2017, *AJ*, 153, 78
 Cólón, K. D., Ford, E. B., Lee, B., Mahadevan, S., & Blake, C. H. 2010, *MNRAS*, 408, 1494
 Copperwheat, C. M., Wheatley, P. J., Southworth, J., et al. 2013, *MNRAS*, 434, 661
 Cortés-Zuleta, P., Rojo, P., Wang, S., et al. 2020, *A&A*, 636, A98
 Covino, E., Esposito, M., Barbieri, M., et al. 2013, *A&A*, 554, A28
 Cowan, N. B., & Agol, E. 2011, *ApJ*, 729, 54
 Cowan, N. B., Machalek, P., Croll, B., et al. 2012, *ApJ*, 747, 82
 Dahl, E. K., Chanover, N. J., Orton, G. S., et al. 2021, *PSJ*, 2, 16
 Damasso, M., Giacobbe, P., Calciolone, P., et al. 2010, *PASP*, 122, 1077
 Daylan, T., Günther, M. N., Mikal-Evans, T., et al. 2021, *AJ*, 161, 131
 de Vaucouleurs, G. 1964, *Icar*, 3, 187
 Demory, B.-O., de Wit, J., Lewis, N., et al. 2013, *ApJL*, 776, L25
 Esteves, L. J., De Mooij, E. J. W., & Jayawardhana, R. 2013, *ApJ*, 772, 51
 Esteves, L. J., De Mooij, E. J. W., & Jayawardhana, R. 2015, *ApJ*, 804, 150
 Foreman-Mackey, D., Hogg, D. W., Lang, D., & Goodman, J. 2013, *PASP*, 125, 306
 Fressin, F., Knutson, H. A., Charbonneau, D., et al. 2010, *ApJ*, 711, 374
 Garhart, E., Deming, D., Mandell, A., et al. 2020, *AJ*, 159, 137
 Gaudi, B. S., Stassun, K. G., Collins, K. A., et al. 2017, *Natur*, 546, 514
 Gibson, N. P., Pollacco, D., Simpson, E. K., et al. 2008, *A&A*, 492, 603
 Gibson, N. P., Pollacco, D., Simpson, E. K., et al. 2009, *ApJ*, 700, 1078
 Gillon, M., Smalley, B., Hebb, L., et al. 2009, *A&A*, 267, 259
 Hanel, R., Conrath, B., Herath, L., Kunde, V., & Pirraglia, J. 1981, *JGR*, 86, 8705
 Hanel, R. A., Conrath, B. J., Kunde, V. G., Pearl, J. C., & Pirraglia, J. A. 1983, *Icar*, 53, 262
 Hapke, B. 1963, *JGR*, 68, 4571
 Hay, K. L., Collier-Cameron, A., Doyle, A. P., et al. 2016, *MNRAS*, 463, 3276
 Hebb, L., Collier-Cameron, A., Loeillet, B., et al. 2009, *ApJ*, 693, 1920
 Heng, K., & Demory, B.-O. 2013, *ApJ*, 777, 100
 Heng, K., & Li, L. 2021, *ApJL*, 909, L20
 Heng, K., Morris, B. M., & Kitzmann, D. 2021, *NatAs*, in press
 Heng, K., & Showman, A. P. 2015, *AREP*, 43, 509
 Henyey, L. G., & Greenstein, J. L. 1941, *ApJ*, 93, 70
 Holman, M. J., Winn, J. N., Latham, D. W., et al. 2006, *ApJ*, 652, 1715
 Hooton, M. J., de Mooij, E. J. W., Watson, C. A., et al. 2019, *MNRAS*, 486, 2397
 Horak, H. G. 1950, *ApJ*, 112, 445
 Hu, R., Demory, B.-O., Seager, S., Lewis, N., & Showman, A. P. 2015, *ApJ*, 802, 51
 Huang, C. X., Burt, J., Vanderburg, A., et al. 2018, *ApJL*, 868, L39
 Husser, T.-O., Wende-von Berg, S., Dreizler, S., et al. 2013, *A&A*, 553, A6
 Ikwut-Ukwa, M., Rodriguez, J. E., Bieryla, A., et al. 2020, *AJ*, 160, 209
 Jackson, B., Adams, E., Sandidge, W., et al. 2019, *AJ*, 157, 239
 Jansen, T., & Kipping, D. 2020, *MNRAS*, 494, 4077
 Jenkins, J. M., Twicken, J. D., McCauliff, S., et al. 2016, *Proc. SPIE*, 9913, 99133E
 Jiang, I.-G., Yeh, L.-C., Thakur, P., et al. 2013, *AJ*, 145, 68
 Johns, D., Reed, P. A., Rodriguez, J. E., et al. 2019, *AJ*, 158, 78
 Johnson, M. C., Cochran, W. D., Albrecht, S., et al. 2014, *ApJ*, 790, 30
 Kane, S. R., Bean, J. L., Campante, T. L., et al. 2021, *PASP*, 133, 014402
 Keating, D., Stevenson, K. B., Cowan, N. B., et al. 2020, *AJ*, 159, 225
 Kitzmann, D., & Heng, K. 2018, *MNRAS*, 475, 94
 Kitzmann, D., Heng, K., Oreshenko, M., et al. 2020, *ApJ*, 890, 174
 Komacek, T. D., & Showman, A. P. 2016, *ApJ*, 821, 16
 Komacek, T. D., & Showman, A. P. 2020, *ApJ*, 888, 2
 Kreidberg, L. 2015, *PASP*, 127, 1161
 Kundurthy, P., Becker, A. C., Agol, E., Barnes, R., & Williams, B. 2013, *ApJ*, 764, 8
 Lally, M., & Vanderburg, A. 2020, *BAAS*, 52, 1
 Lee, J. W., Youn, J.-H., Kim, S.-L., Lee, C.-U., & Koo, J.-R. 2011, *PASJ*, 63, 301
 Li, L., Jiang, X., West, R. A., et al. 2018, *NatCo*, 9, 3709
 Loeb, A., & Gaudi, B. S. 2003, *ApJL*, 588, L117
 Lothringer, J., Barman, T., & Koskinen, T. 2018, *ApJ*, 866, 27
 Lund, M. B., Rodriguez, J. E., Zhou, G., et al. 2017, *AJ*, 154, 194
 Maciejewski, G., Dimitrov, D., Fernández, M., et al. 2016, *A&A*, 588, L6
 Maciejewski, G., Dimitrov, D., Neuhäuser, R., et al. 2010, *MNRAS*, 407, 2625
 Maciejewski, G., Dimitrov, D., Seeliger, M., et al. 2013a, *A&A*, 551, A108
 Maciejewski, G., Errmann, R., Raetz, St., et al. 2011, *A&A*, 528, A65
 Maciejewski, G., Fernández, M., Aceituno, F., et al. 2015, *A&A*, 577, A109
 Maciejewski, G., Fernández, M., Aceituno, F., et al. 2018a, *A&A*, 68, 371
 Maciejewski, G., Niedzielski, A., Wolszczan, A., et al. 2013b, *AJ*, 146, 147
 Maciejewski, G., Puchalski, D., Saral, G., et al. 2013c, *IBVS*, 2013, 6082
 Maciejewski, G., Stangret, M., Ohlert, J., et al. 2018b, *IBVS*, 63, 6243
 Madhusudhan, N., Harrington, J., Stevenson, K. B., et al. 2011, *Natur*, 469, 64
 Mancini, L., Esposito, M., Covino, E., et al. 2015, *A&A*, 579, A136
 Mancini, L., Southworth, J., Naponiello, L., et al. 2021, *MNRAS*, submitted
 Mannaday, V. K., Thakur, P., Jiang, I.-G., et al. 2020, *AJ*, 160, 47
 Mansfield, M., Bean, J. L., Stevenson, K. B., et al. 2020, *ApJL*, 888, L15
 Mantalto, M., Gregorio, J., Boué, G., et al. 2012, *MNRAS*, 427, 2757
 Marley, M. S., Gelino, C., Stephens, D., Lunine, J. I., & Freedman, R. 1999, *ApJ*, 513, 879
 Masuda, K. 2015, *ApJ*, 805, 28
 Maxted, P. F. L., Anderson, D. R., Doyle, A. P., et al. 2013, *MNRAS*, 428, 2645
 Mazej, T., Nachmani, G., Sokol, G., et al. 2012, *A&A*, 541, A56
 Mie, G. 1908, *AnPhy*, 330, 377
 Mislis, D., Mancini, L., Tregloan-Reed, J., et al. 2015, *MNRAS*, 448, 2617
 Morris, S. L. 1985, *ApJ*, 295, 143
 Morris, S. L., & Naftilan, S. A. 1993, *ApJ*, 419, 344
 Narita, N., Sato, B., Hirano, T., & Tamura, M. 2009, *PASJ*, 61, L35
 Nascimbeni, V., Cunial, A., Murabito, S., et al. 2013, *A&A*, 549, A30
 O'Donovan, F. T., Charbonneau, D., Bakos, G. Á., et al. 2007, *ApJL*, 663, L37
 Oberst, T. E., Rodriguez, J. E., Cólón, K. D., et al. 2017, *AJ*, 153, 97
 Oreshenko, M., Heng, K., & Demory, B.-O. 2016, *MNRAS*, 457, 3420
 Owens, N., de Mooij, E. J. W., Watson, C. A., & Hooton, M. J. 2021, *MNRAS*, 503, L38
 Öztürk, O., & Erdem, A. 2019, *MNRAS*, 486, 2290
 Öztürk, O., & Erdem, A. 2021, *NewA*, 82, 101454

- Pál, A., Bakos, G. Á., Torres, G., et al. 2008, *ApJ*, **680**, 1450
- Parmentier, V., & Crossfield, I. J. M. 2018, in *Handbook of Exoplanets*, ed. H. J. Deeg & J. A. Belmonte (Cham: Springer), 116
- Parmentier, V., Fortney, J. J., Showman, A. P., Morley, C., & Marley, M. S. 2016, *ApJ*, **828**, 22
- Patra, K. C., Winn, J. N., Holman, M. J., et al. 2017, *AJ*, **154**, 4
- Patra, K. C., Winn, J. N., Holman, M. J., et al. 2020, *AJ*, **159**, 150
- Pearl, J. C., & Conrath, B. J. 1991, *JGR*, **96**, 18921
- Pearl, J. C., Conrath, B. J., Hanel, R. A., Pirraglia, J. A., & Coustenis, A. 1990, *Icar*, **84**, 12
- Pierrehumbert, R. T. 2010, *Principles of Planetary Climate* (Cambridge: Cambridge Univ. Press)
- Pollacco, D., Skillen, I., Collier Cameron, A., et al. 2008, *MNRAS*, **385**, 1576
- Pont, F., Zucker, S., & Queloz, D. 2006, *MNRAS*, **373**, 231
- Powell, D., Loudon, T., Kreidberg, L., et al. 2019, *ApJ*, **887**, 170
- Püsküllü, Ç., Soyduğan, F., Erdem, A., & Budding, E. 2017, *NewA*, **55**, 39
- Ricci, D., Sada, P. V., Navarro-Meza, S., et al. 2017, *PASP*, **129**, 064401
- Roman, M., & Rauscher, E. 2017, *ApJ*, **850**, 17
- Rostron, J. W., Wheatley, P. J., Anderson, D. R., et al. 2014, *MNRAS*, **441**, 3666
- Russell, H. N. 1916, *ApJ*, **43**, 173
- Sada, P. V., Deming, D., Jennings, D. E., et al. 2012, *PASP*, **124**, 212
- Santerne, A., Moutou, C., Barros, S. C. C., et al. 2012, *A&A*, **544**, L12
- Seager, S. 2010, *Exoplanet Atmospheres* (Princeton, NJ: Princeton Univ. Press)
- Shakura, N. I., & Postnov, K. A. 1987, *A&A*, **183**, L21
- Showman, A. P., & Guillot, T. 2002, *A&A*, **385**, 166
- Shporer, A. 2017, *PASP*, **129**, 072001
- Shporer, A., & Hu, R. 2015, *AJ*, **150**, 112
- Shporer, A., Jenkins, J. M., Rowe, J. F., et al. 2011, *AJ*, **142**, 195
- Shporer, A., Kaplan, D. L., Steinfeldt, J. D. R., et al. 2010, *ApJL*, **725**, L200
- Shporer, A., O'Rourke, J. G., Knutson, H. A., et al. 2014, *ApJ*, **788**, 92
- Shporer, A., Wong, I., Huang, C. X., et al. 2019, *AJ*, **157**, 178
- Siverd, R. J., Beatty, T. G., Pepper, J., et al. 2012, *ApJ*, **761**, 123
- Smith, J. C., Stumpe, M. C., Van Cleve, J. E., et al. 2012, *PASP*, **124**, 1000
- Sobolev, V. V. 1975, *Light Scattering in Planetary Atmospheres* (Oxford: Pergamon)
- Southworth, J. 2011, *MNRAS*, **417**, 2166
- Sozzetti, A., Torres, G., Charbonneau, D., et al. 2009, *ApJ*, **691**, 1145
- Spake, J. J., Brown, D. J. A., Doyle, A. P., et al. 2016, *PASP*, **128**, 024401
- Sromovsky, L. A., & Fry, P. M. 2002, *Icar*, **157**, 373
- Stevenson, K. B., Bean, J. L., Madhusudhan, N., & Harrington, J. 2014a, *ApJ*, **791**, 36
- Stevenson, K. B., Bean, J. L., Seifahrt, A., et al. 2014b, *AJ*, **147**, 161
- Stevenson, K. B., Line, M. R., Bean, J. L., et al. 2017, *AJ*, **153**, 68
- Stumpe, M. C., Smith, J. C., Catanzarite, J. H., et al. 2014, *PASP*, **126**, 100
- Stumpe, M. C., Smith, J. C., Van Cleve, J. E., et al. 2012, *PASP*, **124**, 985
- Sun, Z., Ji, J., & Dong, Y. 2018, *ChA&A*, **42**, 101
- Szabó, G. M., Szabó, R., Benkő, J. M., et al. 2011, *ApJL*, **736**, L4
- Szabó, Gy. M., Pribulla, T., Pál, A., et al. 2020, *MNRAS*, **492**, L17
- Talens, G. J. J., Justesen, A. B., Albrecht, S., et al. 2018, *A&A*, **612**, A57
- Teske, J., Díaz, M. R., Luque, R., et al. 2020, *AJ*, **160**, 96
- Thakur, P., Mannaday, V. K., Jiang, I.-G., Sahu, D. K., & Chand, S. 2018, *BSRSL*, **87**, 132
- Tripathi, A., Winn, J. N., Johnson, J. A., et al. 2010, *ApJ*, **715**, 421
- Turner, J. D., Ridden-Harper, A., & Jayawardhana, R. 2021, *AJ*, **161**, 72
- Turner, J. D., Smart, B. M., Hardegree-Ullman, K. K., et al. 2013, *MNRAS*, **428**, 678
- Vaňko, M., Maciejewski, G., Jakubík, M., et al. 2013, *MNRAS*, **432**, 944
- Visscher, C., Lodders, K., & Fegley, B. 2006, *ApJ*, **648**, 1181
- von Essen, C., Mallonn, M., Borre, C. C., et al. 2020, *A&A*, **639**, A34
- von Essen, C., Mallonn, M., Cowan, N. B., et al. 2020, *A&A*, **648**, A71
- von Essen, C., Schröter, S., Agol, E., & Schmitt, J. H. M. M. 2013, *A&A*, **555**, A92
- von Essen, C., Stefansson, G., Mallonn, M., et al. 2019, *A&A*, **628**, A115
- Wang, Y.-H., Wang, S., Hinse, T. C., et al. 2019, *AJ*, **157**, 82
- Winn, J. N., Johnson, J. A., Albrecht, S., et al. 2009, *ApJL*, **703**, L99
- Wong, I., Benneke, B., Gao, P., et al. 2020a, *ApJ*, **159**, 234
- Wong, I., Benneke, B., Shporer, A., et al. 2020b, *AJ*, **159**, 104
- Wong, I., Knutson, H. A., Kataria, T., et al. 2016, *ApJ*, **823**, 122
- Wong, I., Shporer, A., Daylan, T., et al. 2020c, *AJ*, **160**, 155
- Wong, I., Shporer, A., Kitzmann, D., et al. 2020d, *AJ*, **160**, 88
- Yee, S. W., Winn, J. N., Knutson, H. A., et al. 2020, *ApJL*, **888**, L5
- Zhang, M., Knutson, H. A., Kataria, T., et al. 2018, *AJ*, **155**, 83
- Zucker, S., Mazeh, T., & Alexander, T. 2007, *ApJ*, **670**, 1326